MOLECULAR MODIFICATION OF GRAPHENE

WONG SWEE LIANG

(B. Sc.(Hons), NATIONAL UNIV. of SINGAPORE)

A THESIS SUBMITTED

FOR THE DEGREE OF DOCTOR OF PHILOSOPHY

NUS GRADUATE SCHOOL FOR INTEGRATIVE

SCIENCES AND ENGINEERING

NATIONAL UNIVERSITY OF SINGAPORE

2013

Declaration

I hereby declare that the thesis is my original work and it has been written by me in its entirety. I have duly acknowledged all the sources of information which have been used in the thesis.

This thesis has also not been submitted for any degree in any university previously.

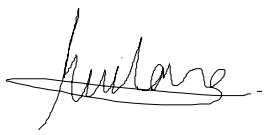

Wong Swee Liang

15 July 2013

Dedicated to my beloved wife, family and friends.

Acknowledgement

First and foremost, I would like to take this opportunity to express my gratitude towards my supervisors, Prof. Wee and Asst. Prof. Chen Wei. The insightful guidance and advice provided by them over these four years have proven to be invaluable. Even though when occupied with work, their meticulous and tireless review of my manuscripts as well as the care and concern that they show for students have never failed to impress me. Without them, the work presented herein would not have been possible.

I would also like to thank my fellow students and friends both in and outside of the Surface Science Laboratory: Yong Siah, Sharon, Tianchao, Wang Rui, Yuli, Huang Han, Jian Qiang, Guanggeng, Wentao, Dongchen, Yuzhan, Cao Liang, Pan Feng, Jia Lin, Iman Santoso and so many others whose paths have crossed with mine along this journey. Their companionship and aid provided throughout the course of my PhD study is priceless and will be sorely missed. I would like to thank the seniors in my laboratory who have selflessly imparted many experimental techniques and even take the extra effort to analyse the data with me.

In particular, I would like to mention my deepest thanks for Huang Han, who spent a lot of time and effort answering both scientific and personal questions of mine. He never rejected any request for help nor took any credit for the great assistance he has rendered in my projects. His integrity and dedication to proper science is worthy of mention and would always be a model for me.

I am also appreciative of the support and encouragement that my friends and family have shown me through this period of time which constantly renews my strength

in my endeavours. Last but not least, my beloved wife, Mrs Lin Yinghan, who has always been a pillar of support and a source of joy not only during my pursuit of the doctorate but also my entire life.

List of Publications

Swee Liang Wong*, H. Huang, W. Chen, and A.T.S. Wee, STM studies of epitaxial graphene, *MRS Bull.* **37**, 12, 1195-1202 (2012).

Swee Liang Wong*, H. Huang, Y.Z. Wang, L. Cao, D.C. Qi, I. Santoso, W. Chen and A.T.S. Wee, Quasi-Free-Standing Epitaxial Graphene on SiC(0001) by Fluorine intercalation from a molecular source, *ACS Nano* **5**, 7662-7668 (2011).

Swee Liang Wong*, H. Huang, Y.L. Huang, Y.Z. Wang , X.Y. Gao , T. Suzuki , W. Chen and A.T.S. Wee, Effect of fluorination on the molecular packing of perfluoropentacene and pentacene ultrathin films on Ag (111), *J. Phys. Chem. C* **114**, 9356-9361 (2010).

K.J. Rietwyk, Swee Liang Wong*, L. Cao, K. M. O'Donnell, L. Ley, A. T. S. Wee, and C. I. Pakes, Work function and electron affinity of the fluorine-terminated (100) diamond surface, *Appl. Phys. Lett.* **102**, 091604 (2013).

M. Yokoyama, Swee Liang Wong*, W. Chen, A.T.S. Wee, T. Matsui and J. Yuhara, Symmetrical transition of an atomic arrangement for two-dimensional Bi films on Rh(111) in the submonolayer regime, *Surf. Sci.* **605**, 844-847 (2011).

H. Huang, Swee Liang Wong*, W. Chen and A.T.S. Wee, LT-STM studies on substrate-dependent self-assembly of small organic molecules, *J. Phy. D: Applied Physics* **44**, 464005 (2011).

H. Huang, Swee Liang Wong*, C.C. Tin and A.T.S. Wee, Epitaxial growth and characterization of graphene on free-standing polycrystalline 3C-SiC, *J. Appl. Phys.* **110**, 014308-1 (2011).

J.T Sun, H. Huang, Swee Liang Wong*, Y.P. Feng and A.T.S. Wee, Energy-gap opening in a Bi (110) nanoribbon induced by edge reconstruction, *Phys. Rev. Lett.* **109**, 246804 (2012).

H. Huang, D.C. Wei, J.T. Sun, Swee Liang Wong*,Y.P. Feng, A.H. Castro Neto and A.T.S. Wee, Spatially resolved electronic structures of atomically precise armchair graphene nanoribbons, *Sci. Rep.* **2**, 983 (2012).

H. Glowatzki, G. Heimel, A. Vollmer, Swee Liang Wong*, H. Huang, W. Chen, A.T.S. Wee, J.P. Rabe and N. Koch, Impact of fluorination on initial growth and stability of pentacene on Cu(111), *J. Phys. Chem. C* **116**, 7726–7734 (2012).

Table of Contents

Summary

In this thesis, we investigate the modification of epitaxial graphene on SiC (0001) through the application of organic molecules in three different systems. Scanning tunnelling microscopy and spectroscopy measurements are used to visualise their effects on the local atomic scale while photoemission spectroscopy (PES) is employed to measure general chemical and electronic changes in the graphene layer. Throughout the thesis, we will correlate the observations on the atomic scale with the macroscopic effects observed by PES measurements.

For the first system, we have demonstrated successful fluorine intercalation between the buffer layer and the substrate using fluorinated fullerene as a molecular source of fluorine. Two states are formed during the process at different annealing temperatures, namely semi-intercalated graphene and quasi-freestanding graphene. Scanning tunnelling microscopy (STM) and spectroscopy (STS) measurements reveal that the semi-intercalated graphene is periodically bonded to the substrate and exhibits topographical properties of a narrow graphene ribbon array which displays an electronic band gap of 280meV. After intercalation is completed, quasi-freestanding graphene is formed and is found to be charge neutral with a fluorine passivated silicon layer beneath it. Highly localized perturbation caused by the presence of adsorbed fluorine was also observed on the quasi-freestanding graphene. Photoemission spectroscopy (PES) confirms the associated electronic and structural changes.

A method of selective fluorination using deposited $C_{60}F_{36}$ molecules is also presented. Synchrotron radiation is used to induce fluorine dissociation from the

molecules and subsequent C-F bond formation at specific regions on graphene. The efficacy and localisation of this method is determined using PES measurements. Selectivity of the fluorination process was demonstrated with the desired region showing enhanced signals of C-F bonds and fluorine content. Lastly, we carried out successful formation and LT-STM characterization of a bimolecular network consisting of 6T and F_4-TCNQ molecules to generate a periodic potential on epitaxial graphene. Bimolecular networks corresponding to 1:2 F_4-TCNQ to 6T molecular coverage ratio was formed with a doping range of the molecules limited to a radius of 4 nm. PES is performed to calibrate the growth of the molecular network while preliminary angular resolved PES studies observe a reduction in the graphene band velocity of up to 14% after deposition of the bimolecular network.

List of Figures

List of Abbreviations

0D	Zero-Dimensional
1D	One-Dimensional
2D	Two-Dimensional
3D	Three-Dimensional
vdW	Van Der Waals
Ru	Ruthenium
LT-STM	Low Temperature Scanning Tunnelling Microscopy
STM	Scanning Tunnelling Microscopy
STS	Scanning Tunnelling Spectroscopy
WSxM	Windows Scanning X Microscope
LEED	Low Energy Electron Diffraction
LEEM	Low Energy Electron Microscopy
PEEM	Photoemission Electron Microscopy
TCNQ	Teracyanoquinonedimethane
PTCDA	3,4,9,10-perylenetetracarboxylic dianhydride
F_4-TCNQ	Tetrafluoro-tetracyanoquinodimethane
6T	α-sexithiophene
PES	Photoemission Spectroscopy
ARPES	Angular Resolved Photoemission Spectroscopy
MDC	Momentum Distribution Curve
NEXAFS	Near Edge X-Ray Absorption Fine Structure
XAS	X-Ray Absorption Spectroscopy

SINS	Surface, Interface and Nanostructure Science
SSLS	Singapore Synchrotron Light Source
B.E.	Binding Energy
K.E.	Kinetic Energy
UHV	Ultra-High Vacuum
E_F	Fermi Level
SiC	Silicon Carbide
XPS	X-ray Photoelectron Spectroscopy
UPS	Ultra-violet Photoelectron Spectroscopy
SECO	Secondary Electron Cut-off
AEY	Auger Electron Yield
QCM	Quartz Crystal Microbalance
DOS	Density of States
LDOS	Local Density of States
HOPG	Highly Oriented Pyrolytic Graphite
XeF_2	Xenon Difluoride
RMS	Root Mean Square
FT	Fourier Transformation
V_{tip}	Tip Bias
Ir	Iridium
YAG	Yttrium Aluminium Garnet
Au	Gold
ML	Monolayer

Chapter 1: Introduction

In this chapter, the fundamental properties of graphene will be briefly discussed first. Following which, the functionalization of graphene and their applications will be touched on to provide a background for the work in this dissertation. Lastly, we will give an overview of the current research progress on molecule – graphene systems which are the main focus of the experiments.

1.1 Basic Properties of Graphene

Graphene, comprising atomically thin layers of carbon atoms, has been an intensively researched topic since the discovery of its extraordinary electronic properties in 2004[1-4] which led to the Nobel Prize award for Geim and Novoselov in 2010. It is a two dimensional allotrope of the carbon family, with the 0D, 1D and 3D counterparts being fullerene, carbon nanotubes and graphite respectively, as illustrated in Figure 1.1.[5] The graphene layer is not completely flat and there exists out of plane undulations of the layer due to flexural phonons.[6-9] In addition, the graphene surface roughness is directly proportional to the underlying substrate roughness as demonstrated when graphene is placed on substrates of varying roughness such as silicon dioxide, mica and boron nitride.[10-12]

Graphene is made up of carbon atoms residing in the same plane bonded to each nearest neighbour by three sp^2 σ bonds and a delocalized π bond. The electrons of these carbon π-orbitals are delocalized over the entire graphene system, giving rise to its conductive nature. As the valence electronic shells of the graphene atoms are filled,

graphene is inert and highly stable, even in ambient atmospheres. The chemical structure of graphene is presented in Figure 1.1b.

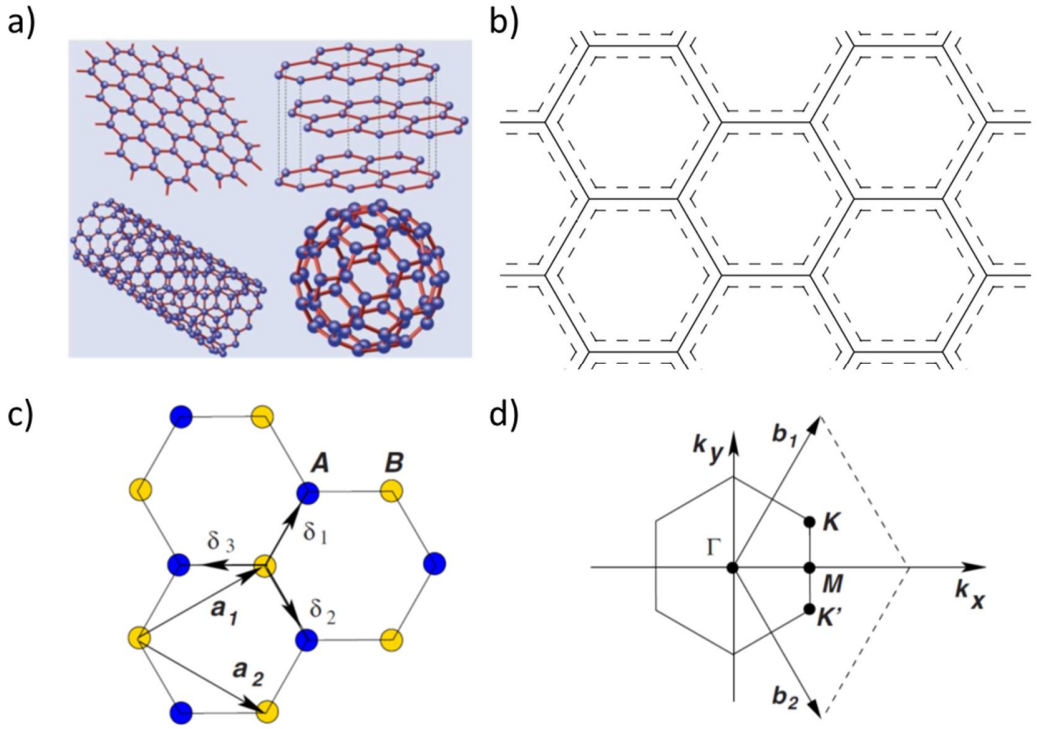

Figure 1.1 a) Carbon allotropes, from clockwise: graphene, graphite, carbon nanotubes and fullerene. b) Chemical structure of graphene. c) Unit cell of graphene with the lattice vectors a_1 and a_2 indicated. $\delta_{1,2,3}$ are the distance between nearest neighbouring carbon atoms. Carbon atoms belonging to different sublattices are highlighted in different colours. d) Corresponding Brilluoin zone of graphene with b_1 and b_2 being reciprocal lattice vectors. Figures a), b) and c) are reproduced with permission from Reference 5. ©2009, American Physical Society.

Figure 1.1c describes the unit cell of graphene. It is made up of 2 inter-penetrating triangular sub lattices with each containing one of the two carbon atoms in the unit cell.[5] The lattice parameters of graphene are $a_1 = a_2 = 0.246$nm, with an included angle of 60° consistent with the three-fold symmetry of the system. By plotting the reciprocal lattice vectors, b_1 and b_2 of the system in Figure 1.1d, the Brilluoin Zone is defined. Notably, it

also follows a three-fold symmetry with the conduction band minima and valence bands maxima located at the K and K' positions.

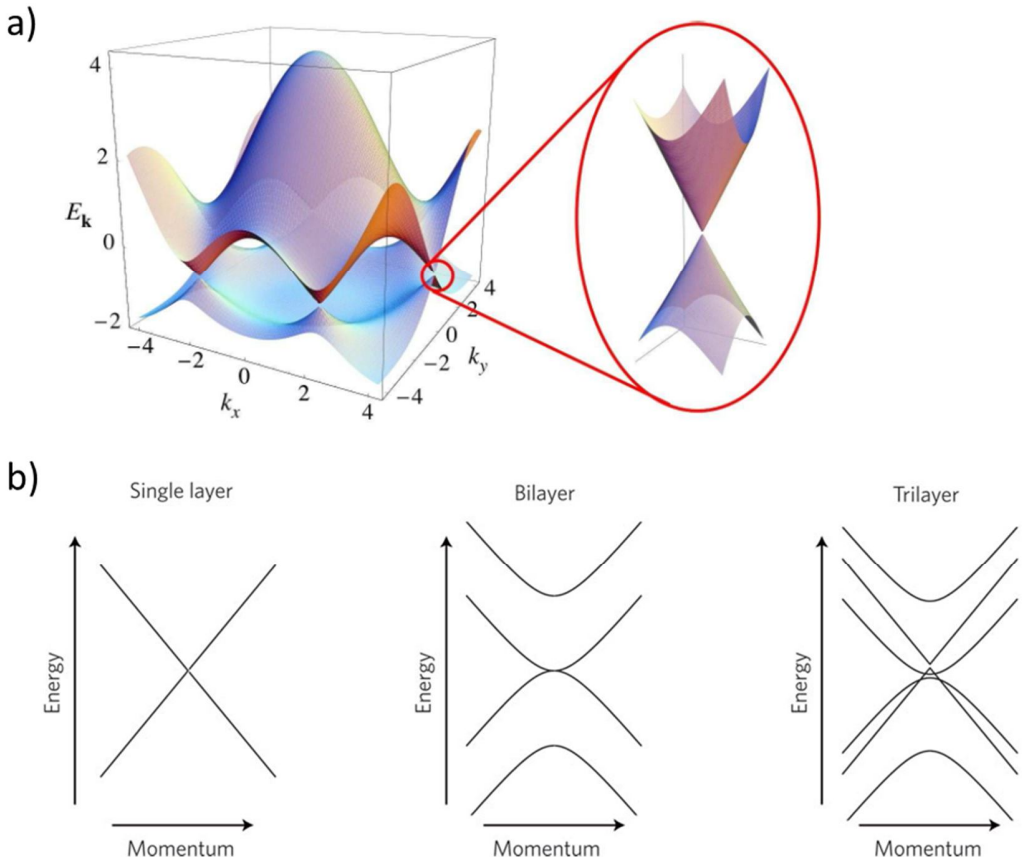

Figure 1.2 a) (Left) Band dispersion of graphene with energy units of *t*. (Right) Conical dispersion at K and K' points. b) Electronic dispersion of (left) monolayer graphene, (centre) bilayer graphene and (right) ABA stacked trilayer graphene. Figure a) is reproduced with permission from Reference 5. ©2009, American Physical Society. Figure b) is reproduced with permission from Reference 19. ©2011, Macmillian Publishers Limited.

Due to its 2-dimensional honeycomb nature, the electronic energy band dispersion, *E*, of monolayer graphene at low energy regimes (within 1eV) about the charge neutrality point at the K/K' points of the Brilluoin Zone is found to be linear[5,13] (Figure 1.2a) with

no electronic band gap between the conduction and valence bands as described by the equation below:

$$E = \hbar v_F k \tag{1.1}$$

where $\hbar$ is the Planck constant divided by 2π, k is the magnitude of the electron crystal momentum with respect to the reciprocal lattice location of the Dirac point and v_F is the Fermi velocity, given by $3ta/(2\hbar) \approx 10^6$ ms^{-1}. $t \approx 2.8$ eV is the hopping parameter used and a is the lattice parameter of graphene.[5] Due to the linearity of the dispersion, dispersion cones are present at the K/K' points for monolayer graphene at low energies. This electronic band structure of graphene has been measured by Angular Resolved Photoemission Spectroscopy (ARPES), Scanning Tunneling Microscopy (STM) and also electronic transport measurements.[14-18]

In addition, the effective mass of electrons in the monolayer graphene system is zero and the charge carriers in graphene behave as relativistic particles described by Dirac equations.[5,18] As the electronic dispersion of single layer graphene is only linearly dependent on k, the density of states is also linearly dependent on k.[5] Therefore, the density of states for monolayer graphene vanishes at the Dirac point, defined at the crossing between the conduction and valence band. Figure 1.2b shows the electronic dispersion for different number of graphene layers.[19] For the case of bilayer graphene, an additional band occurs but the dispersion is now hyperbolic while for trilayer ABA stacked graphene, it is a combination of both linear and hyperbolic bands. The offset of the linear and hyperbolic bands at charge neutrality are to account for the experimental observations of overlapping Landau levels from the hyperbolic and linear bands.[20]

Eventually, as the number of graphene layers increases, the electronic structure of graphite is obtained.

Due to the unique electronic band structure of graphene, it possesses a range of remarkable properties. Single layer has an extremely high electron mobility [5,10,18,21,22,23,24], with reported values of up to 500,000 $cm^2V^{-1}s^{-1}$ in graphene samples sandwiched between hexagonal boron nitride substrates.[24] Other electronic properties also include the observation of a half-integer quantum Hall effect[1,4,25-27]. The lack of a band gap allows an easily tuned charge carrier system from holes to electrons and vice versa just by shifting the Fermi level across the Dirac point, allowing ambipolar charge transport.[1,2,4,18] Furthermore, as graphene is a 2D material, the Fermi level can be easily tuned by applying a voltage through a metal back gate with an intermediate dielectric material such as silicon dioxide.[1,2,4,18] However, the lack of a band gap results in the unsuitability of graphene in digital electronic systems due to the very low on-off ratios of ~10 to 100 in pristine graphene.[18]

Due to graphene being atomically thick, only 2.3% of light that passes through it is absorbed[28], making it a suitable candidate for application as a transparent conductor for use in touch screen panels[29] and photovoltaic cells.[30-33] Furthermore, the strong in plane covalent bonds between carbon atoms gives the graphene a large mechanical strengthwith a Young's modulus of ~ 1 TPa.[34] The out of plane flexibility of the carbon sp^2 bond structure also translates to the observed flexibility of the carbon layer. Due to its large surface to volume ratio and sensitivity to dopants on its charge carrier concentration, highly sensitive gas sensors have been fashioned from graphene with detection limits of down to single molecules.[35-37] The small spin-coupling effect of the low mass carbon

atoms and high electron mobility in graphene also makes it suitable for spintronic applications with fairly long spin diffusion length of up to 100 μm at low temperatures.[38-41]

Graphene can be produced from a variety of methods. It can be isolated by mechanically exfoliating highly oriented pyrolytic graphite (HOPG) which can provide high quality samples of up to 1 mm.[3,18] It can also be epitaxially grown from both Si and C faces of the SiC substrate via segregation of carbon atoms when annealed at high temperatures.[42-44] Metal substrates can also been used as catalysts for the thermal decomposition of hydrocarbons to produce graphene in chemical vapor deposition processes which can be subsequently transferred onto other substrates.[45-48] Another method of production involves the chemical reduction of exfoliated graphene oxide which results in reduced graphene oxide or chemically functionalized graphene.[49-51] Recent techniques also include arc discharge between graphite electrodes[52], electrochemical exfoliation of graphite[53] and solvothermal synthesis of graphene.[54]

1.2 Modification of Graphene

Graphene, being two dimensional and having a large surface to volume ratio, makes the material very accessible to functionalization and modification by atomic or molecular adsorption. Modification of graphene can take place through various methods. Covalent functionalization involves the forming of covalent bonds between the graphene C atoms and other species.[55-59] Other types of modification include the removal of C atoms from graphene to form vacancies[60] or lithographical patterning of the graphene layer to create nanomesh and nanoribbons.[61-64] Non-covalent functionalization consists of

molecules or atoms being adsorbed[65-68] onto or introduced beneath the graphene layer[69-72] without perturbing the sp^2 structure of graphene.

The most basic forms of covalent functionalization involve usage of reactive atomic elements such as metals, hydrogen, fluorine and oxygen. During the formation of a covalent bond, the planar sp^2 configuration of the C=C bonds is broken when the free π orbital forms an out of plane sp^3 bond with the adatom, resulting in an out-of plane buckling of graphene. The resultant absence of the π band at the low energy regime results in a band gap. Such functionalization can be reversible, depending on the strength of the bond formed. Hydrogenation is easily reversible at low temperatures of 200°C[58] while fluorination, having a stronger C-F bond, requires a higher temperature of 400°C[73] to be removed. Fluorination of graphene has been shown to create an electronic band gap of up to 3eV.[73] Depending on the element that was involved, various electronic and magnetic properties can be induced in the functionalized graphene.[55,74-76] It has been shown that hydrogenation results in a room temperature ferromagnetic signal.[75] Substitutional doping of nitrogen atoms has also been reported to induce asymmetry in the local density of states about the Fermi level of the surrounding graphene.[74]

Lithographical patterning is a commonly used technique to create a band gap in graphene. Such a process is normally irreversible and aims to fashion quantum structures such as nanomeshes[64,77] and nanoribbons[61,62]. Decreasing the dimensions of graphene would then result in a quantum confinement of the electrons and therefore produce an electronic band gap of up to a few hundred meV. Graphene nanoribbons can also be produced by chemically unzipping carbon nanotubes.[78-80] However, electron mobility through these nanoribbons is lowered due to the presence of defective edges.[81,82] To

circumvent this issue, patterned hydrogenation has been performed by Balog et. al. on graphene, in which hydrogen atoms selectively bond to the moiré pattern of graphene on Ir (111), to create a moderate band gap in graphene of up to 0.7 eV.[57] Bottom up approaches to produce pristine graphene nanoribbons from molecular precursors have also been demonstrated but it requires a metallic surface for the required cyclo-dehydrogenation reaction for the formation of the nanoribbons.[83-85] Thus, it will be of interest to generate electronic band gaps in graphene without requiring destructive methods or additional bonding of foreign atoms to the graphene surface. In Chapter 3, this issue is addressed by partially intercalating epitaxial graphene on SiC (0001) with fluorine to generate a graphene array with a band gap of 280meV.

Reversible non-covalent and non-destructive methods of functionalization involve introduction of adsorbates such as molecules or atoms onto or below the graphene surface. The most common interactions of these adsorbates involve charge transfer with graphene,[67,68,86] van der Waals (vdW)[66,87] as well as electrostatic[88,89] interactions. These processes are usually reversible and involve only simple removal of the adsorbates through thermal or solvent application. Charge transfer results in a doping of the graphene which is useful for tuning the Fermi level relative to the Dirac point and has been demonstrated using metallic atoms such as potassium as well as organic molecules.[67,68,86] Such non-covalent functionalization graphene is often performed to increase the charge carrier density in graphene and thus lower its sheet resistivity for use as electrodes. In addition, the potential asymmetry between graphene layers induced by the presence of these dopants such as potassium can also result in an electronic band gap.[68]

Instead of adsorbing onto the graphene surface, foreign elements can also be introduced beneath the graphene layer instead, whereby elements such as hydrogen[72,90], fluorine[69] and gold[91,92] can be intercalated between the graphene and metallic or silicon carbide substrate. These intercalants may react with the atoms at the interface, such as in the formation of Si-H bonds when hydrogen is intercalated beneath epitaxial graphene on SiC (0001)[72,90], thereby forming a new interface between the graphene layer and the substrate. They can also remain as interstitials without chemically reacting with either substrate or graphene. These methods often alter the charge carrier concentration of the graphene layer as well as minimize the interactions it has with the underlying substrate due to the presence of a passivated interface. Quasi-freestanding graphene has been produced via hydrogen intercalation of epitaxial graphene on SiC (0001) substrates.[72,90] However such intercalations have not been well studied at the atomic scale and hence will be the subject of our STM/STS measurements in Chapter 3.

1.3 Organic Molecule – Graphene System

Organic molecules have been studied extensively in the past decade, with recent advances in devices such as organic light emitting diodes, solar cells and field-effect transistors providing continuous impetus for their research.[93-95] Organic molecules consist of an aromatic hydrocarbon base structure, with their properties varying with the functional groups attached to it. They exhibit a variety of properties such as magnetism in magnetic (cobalt, iron, etc.) atom containing phthalocyanines[96,97], electron acceptor[67,98] or donor[86,99] molecules, catalytic behavior,[100,101] and as reactive radicals that covalently functionalize graphene.[102,103]

Due to their carbon makeup, organic molecules are compatible with graphene and have been shown to non-destructively modify the electrical and physical properties of graphene[104], forming the basis for the following experimental work. Both adsorbates and substrate share similar traits of flexibility, lightweight and an aromatic ring based structure. As noted by the compatibility of their physical structures, graphene has been used as an electrode in organic molecular based field effect transistors[105,106], photovoltaic cells[32,107,108] and even as a template to promote charge transfer induced magnetic moments in Teracyanoquinonedimethane (TCNQ) molecules.[109] Organic electron acceptors and donors are commonly used to dope graphene via non-covalent charge transfer. Tetrafluoro-tetracyanoquinodimethane (F4-TCNQ) has a known p-type doping effect on graphene of up to 0.7eV.[67] It has been shown to generate a charge neutral bilayer graphene while at the same time creating a band gap due to a potential difference across layers.[98] Thus, it is of importance to understand the packing structure of such doping molecules to improve their incorporation into graphene devices. One particular electron acceptor molecule, $C_{60}F_{48}$, is investigated using STM in Chapter 3.

Reactive molecules can also covalently functionalize graphene to alter its electronic and magnetic properties.[102,103,110] Recent studies have shown that reduced 4-nitrophenyl diazonium tetrafluoroborate covalently bonds to epitaxial graphene on SiC (0001) to generate an electronic band gap.[102] Similarly, solution based spontaneous grafting of nitro phenyl groups on graphene also converts epitaxial graphene from a semi-metal to a semiconductor due to the formation of covalent bonds between graphene and the molecules. Even though graphene is inert, when the molecules are reactive enough to break the C=C bonds to form sp^3 covalent bonds as in the case of diazonium radicals[102],

the π bonds which contribute to the electronic states at the Fermi level and hence conducting charge carriers are disrupted. Such a disruption opens an electronic band gap in graphene. In certain cases, they act as a carrier for the desired element to be bonded.[111,112] Larger chains of molecules, polymers containing fluorine have been used to fluorinate the graphene surface by irradiating them with a laser to generate the required fluorine radicals.[111] In particular, we demonstrate the usage of fluorinated fullerenes to both intercalate as well as functionalize the graphene layer with fluorine in Chapters 3 and 4 respectively.

Numerous studies have been performed to investigate the molecular self-assembly and molecule-substrate interactions on graphene.[66,87,96,105,113-117] Due to the inertness of the graphene surface, the diffusion barrier to organic molecules is very low and many as-deposited organic molecules are able to form well defined layers over moderate length scales (μm). Molecules like PTCDA has shown to be able to form continuous molecular layers over graphene, even over step edges.[66] These molecular layers show no chemical interaction with the underlying graphene layer and can serve as a protective overlayer to graphene.[118] Due to the vdW interactions between the out of plane π orbitals of the molecular layers and that of graphene, many organic molecules such as PTCDA[66] and pentacene[105] adsorb with their basal plane lying flat on graphene.

Non-covalent interactions, such as vdW, hydrogen bonding, electrostatic and dipole-dipole interactions between molecules play a part in the self-assembly of these molecules in the layer.[119-122] In particular, hydrogen bonding between electropositive hydrogen atoms and electronegative atoms such as fluorine, nitrogen and oxygen present in molecules is highly directional.[121,123] Such interactions have been shown to create self-

assembled molecular networks on graphite with lattice parameters determined by the positions of the relevant peripheral atoms on the molecules.[124-126] This property will be exploited in Chapter 5 to form a self-assembled bimolecular network consisting of electron accepting F_4-TCNQ with α-sexithiophene (6T) molecules acting as spacers between the dopants to generate a periodic potential on graphene.

Spatially modulated graphene can also act as a template to direct the growth of organic molecular layers.[96,113,127] For the case of graphene grown on metallic substrates such as Ru (111), lattice mismatch between the substrate surface and the graphene generate moiré patterns in the carbon layer. In turn, these patterns act as sites on which the incoming F4-TCNQ molecules selectively adsorb upon, isolating the normally diffusive molecules.[113] Likewise, supramolecular Kagome lattices of magnetic phthalocyanine molecules have been formed on these graphene based moiré pattern.[96] Even though organic molecules are larger than single atoms, they can be buried beneath the graphene layer and decouple it from the substrate. This has been demonstrated by rapidly annealing multilayer fullerenes deposited on graphene grown on an Ir (111) surface which results in their diffusion into the interface between the graphene and metal.[128]

1.4 Thesis Objectives

In the light of the various properties that organic molecules possess and their interactions with graphene, it is therefore of interest to perform studies on molecule-graphene hybrid systems. Such studies would enable us to better understand their interactions with graphene and allow us to improve our control over their electronic and chemical effects on graphene. In particular, it would be beneficial to look into how we

can exploit the unique properties of organic molecules to modify the electronic and physical structure of graphene. This would allow us to achieve a bottom-up approach of modifying graphene using molecules at low dimensions.

Hence, the graphene-molecule systems described in this thesis will be studied using two main approaches, namely STM and PES measurements. STM will be used to study the self-assembly of these molecules on graphene. At the same time, the influence that these molecules have on the physical and electronic structure of graphene would also be measured using STM and STS. PES measurements would be utilized to determine the influences on the electronic structures of both the molecules and graphene. These measurements also include ARPES as well as near edge X-ray absorption fine structure measurements (NEXAFS) that allow probing of the orientation of the electronic orbitals. Such a combination of STM and PES studies allows us to correlate any phenomena observed on the atomic scale with the macroscopic effect that they may have on the electronic structure of graphene.

Three separate organic molecule–graphene systems will be investigated in this thesis. The first will be $C_{60}F_{48}$, in which the morphology of the deposited fluorinated fullerene layer is studied before they are used as a source of fluorine to intercalate the epitaxial graphene on SiC (0001). The various stages of the intercalation process and their associated electronic and structural changes of graphene will be measured using STM/STS and PES is carried out to confirm the associated electronic and structural changes that are observed on the atomic scale. The subsequent chapter will demonstrate the usage of $C_{60}F_{36}$ and synchrotron radiation to selectively fluorinate the graphene surface. Lastly, a bimolecular network made up of F_4-TCNQ and 6T molecules on

epitaxial graphene will be studied first using STM for possible generation of a periodic potential on graphene and then ARPES to determine the influence of this network on the electronic band structure of graphene. The graphene that is used for all three systems is grown on the Si-face of SiC substrates due to its single crystalline orientation and large domain size. The physical properties of this particular graphene system will be elaborated in the following chapter.

In this thesis, we would first discuss the working principles of the relevant techniques used for the measurements followed by a description of the growth and basic properties of the epitaxial graphene on silicon carbide. In the ensuing chapters describing each of the organic molecule-graphene system worked on, we would touch briefly on the motivation behind the choice of molecules in each system studied before having an in-depth presentation and discussion of the results. Relevant results from work done by others would also be brought forth for comparison and analysis. Each chapter will then conclude with a section that summarizes the results and discussion as well as its significance for future work and applications.

References

1. K.S. Novoselov; A.K. Geim; S.V. Morozov; D. Jiang; M.I. Katsnelson; I.V. Grigorieva; S.V. Dubonos and A.A. Firsov, *Nature* **438**, 197-200 (2005).

2. K.S. Novoselov; D. Jiang; F. Schedin; T.J. Booth; V.V. Khotkevich; S.V. Morozov and A.K. Geim, *Proc. Natl. Acad. Sci. USA* **102**, 10451-10453 (2005).

3. K.S. Novoselov; A.K. Geim; S.V. Morozov; D. Jiang; Y. Zhang; S.V. Dubonos; I.V. Grigorieva and A.A. Firsov, *Science (New York, N.Y.)* **306**, 666-669 (2004).

4. Y. Zhang; Y.W. Tan; H.L. Stormer and P. Kim, *Nature* **438**, 201 (2005).

5. A. Castro Neto; N. Peres; K. Novoselov and A. Geim, *Rev. Mod. Phys.* **81**, 109-162 (2009).

6. U. Bangert; M.H. Gass; A.L. Bleloch; R.R. Nair and A.K. Geim, *Phys. Status Solidi A* **206**, 1117-1122 (2009).

7. J.C. Meyer; A.K. Geim; M.I. Katsnelson; K.S. Novoselov; T.J. Booth and S. Roth, *Nature* **446**, 60 (2007).

8. A. Fasolino; J.H. Los and M.I. Katsnelson, *Nature Mater.* **6**, 858 (2007).

9. E. Stolyarova; K.T. Rim; S. Ryu; J. Maultzsch; P. Kim; L.E. Brus; T.F. Heinz; M.S. Hybertsen and G.W. Flynn, *Proc. Natl. Acad. Sci.* **104**, 9209-9212 (2007).

10. C.R. Dean; A.F. Young; I. Meric; C. Lee; L. Wang; S. Sorgenfrei; K. Watanabe; T. Taniguchi; P. Kim; K.L. Shepard and J. Hone, *Nature Nanotech.* **5**, 722 (2010).

11. C.H. Lui; L. Liu; K.F. Mak; G.W. Flynn and T.F. Heinz, *Nature* **462**, 339 (2009).

12. J. Xue; J. Sanchez-Yamagishi; D. Bulmash; P. Jacquod; A. Deshpande; K. Watanabe; T. Taniguchi; P. Jarillo-Herrero and B.J. LeRoy, *Nature Mater.* **10**, 282 (2011).

13. P. Wallace, *Phys. Rev.* **71**, 622-634 (1947).

14. D.L. Miller; K.D. Kubista; G.M. Rutter; M. Ruan; W.A. de Heer; P.N. First and J.A. Stroscio, *Science* **324**, 924 (2009).

15. S.Y. Zhou; G.H. Gweon; A.V. Fedorov; P.N. First; W.A. de Heer; D.H. Lee; F. Guinea; A.H. Castro Neto and A. Lanzara, *Nature Mater.* **6**, 770 (2007).

16. M. Sprinkle; D. Siegel; Y. Hu; J. Hicks; A. Tejeda; A. Taleb-Ibrahimi; P. Le Fèvre; F. Bertran; S. Vizzini; H. Enriquez; S. Chiang; P. Soukiassian; C. Berger; W.A. de Heer; A. Lanzara and E.H. Conrad, *Phys. Rev. Lett.* **103**, 226803 (2009).

17. J. Chae; S. Jung; A.F. Young; C.R. Dean; L. Wang; Y. Gao; K. Watanabe; T. Taniguchi; J. Hone; K.L. Shepard; P. Kim; N.B. Zhitenev and J.A. Stroscio, *Phys. Rev. Lett.* **109**, 116802 (2012).

18. A. Geim, *Science* **324**, 1530-1534 (2009).

19. M. Freitag, *Nature Phys.* **7**, 596-597 (2011).

20. T. Taychatanapat; K. Watanabe; T. Taniguchi and P. Jarillo-Herrero, *Nature Phys.* **7**, 621-625 (2011).

21. T. Ando and T. Nakanishi, *J. Phys. Soc. Jpn.* **67**, 1704-1713 (1998).

22. T. Ando; T. Nakanishi and R. Saito, *J. Phys. Soc. Jpn.* **67**, 2857-2862 (1998).

23. K. Bolotin; K. Sikes; Z. Jiang; M. Klima; G. Fudenberg; J. Hone; P. Kim and H. Stormer, *Solid State Commun.* **146**, 351-355 (2008).

24. A.S. Mayorov; R.V. Gorbachev; S.V. Morozov; L. Britnell; R. Jalil; L.A. Ponomarenko; P. Blake; K.S. Novoselov; K. Watanabe; T. Taniguchi and A.K. Geim, *Nano Lett.* **11**, 2396-2399 (2011).

25. A.F. Young and P. Kim, *Nature Phys.* **5**, 222-226 (2009).

26. N. Stander; B. Huard and D. Goldhaber-Gordon, *Phys. Rev. Lett.* **102**, 026807 (2009).

27. M.I. Katsnelson; K.S. Novoselov and A.K. Geim, *Nature Phys.* **2**, 620-625 (2006).

28. R.R. Nair; P. Blake; A.N. Grigorenko; K.S. Novoselov; T.J. Booth; T. Stauber; N.M.R. Peres and A.K. Geim, *Science* **320**, 1308-1308 (2008).

29. S. Bae; H. Kim; Y. Lee; X. Xu; J.S. Park; Y. Zheng; J. Balakrishnan; T. Lei; H. Ri Kim; Y.I. Song; Y.J. Kim; K.S. Kim; B. Özyilmaz; J.H. Ahn; B.H. Hong and S. Iijima, *Nature Nanotech.* **5**, 574-578 (2010).

30. X. Wang; L. Zhi and K. Müllen, *Nano Lett.* **8**, 323-327 (2008).

31. J. Wu; H.A. Becerril; Z. Bao; Z. Liu; Y. Chen and P. Peumans, *Appl. Phys. Lett.* **92**, 263302 (2008).

32. Z. Liu; Q. Liu; Y. Huang; Y. Ma; S. Yin; X. Zhang; W. Sun and Y. Chen, *Adv. Mater.* **20**, 3924-3930 (2008).

33. H. Zhu; J. Wei; K. Wang and D. Wu, *Sol. Energ. Mat. Sol. Cells* **93**, 1461-1470 (2009).

34. C. Lee; X. Wei; J.W. Kysar and J. Hone, *Science* **321**, 385-388 (2008).

35. F. Schedin; A.K. Geim; S.V. Morozov; E.W. Hill; P. Blake; M.I. Katsnelson and K.S. Novoselov, *Nature Mater.* **6**, 652-655 (2007).

36. B. Huang; Z. Li; Z. Liu; G. Zhou; S. Hao; J. Wu; B.L. Gu and W. Duan, *J. Phys. Chem. C* **112**, 13442-13446 (2008).

37. J.D. Fowler; M.J. Allen; V.C. Tung; Y. Yang; R.B. Kaner and B.H. Weiller, *ACS Nano* **3**, 301-306 (2009).

38. P. Seneor; B. Dlubak; M.B. Martin; A. Anane; H. Jaffres and A. Fert, *MRS Bull.* **37**, 1245 (2012).

39. B. Dlubak; M.B. Martin; C. Deranlot; B. Servet; S. Xavier; R. Mattana; M. Sprinkle; C. Berger; W.A. De Heer; F. Petroff; A. Anane; P. Seneor and A. Fert, *Nature Phys.* **8**, 557-561 (2012).

40. M.H.D. Guimarães; A. Veligura; P.J. Zomer; T. Maassen; I.J. Vera-Marun; N. Tombros and B.J. van Wees, *Nano Lett.* **12**, 3512 (2012).

41. W. Han and R.K. Kawakami, *Phys. Rev. Lett.* **107**, 047207 (2011).

42. H. Huang; W. Chen; S. Chen and A.T.S. Wee, *ACS Nano* **2**, 2513-2518 (2008).

43. P. First; W. De Heer; T. Seyller; C. Berger; J. Stroscio and J. Moon, *MRS Bull.* **35**, 296-305 (2010).

44. C. Berger; X. Wu; P. First; E. Conrad; X. Li; M. Sprinkle; J. Hass; F. Varchon; L. Magaud; M. Sadowski; M. Potemski; Martinez G. and de Heer W.A., *Adv. Solid State Phys.* **47**, 145-157 (2008).

45. X. Li; W. Cai; J. An; S. Kim; J. Nah; D. Yang; R. Piner; A. Velamakanni; I. Jung; E. Tutuc; S.K. Banerjee; L. Colombo and R.S. Ruoff, *Science* **324**, 1312-1314 (2009).

46. K.S. Kim; Y. Zhao; H. Jang; S.Y. Lee; J.M. Kim; K.S. Kim; J.H. Ahn; P. Kim; J.Y. Choi and B.H. Hong, *Nature* **457**, 706-710 (2009).

47. Y. Lee; S. Bae; H. Jang; S. Jang; S.E. Zhu; S.H. Sim; Y.I. Song; B.H. Hong and J.H. Ahn, *Nano Lett.* **10**, 490-493 (2010).

48. X. Li; Y. Zhu; W. Cai; M. Borysiak; B. Han; D. Chen; R.D. Piner; L. Colombo and R.S. Ruoff, *Nano Lett.* **9**, 4359-4363 (2009).

49. S. Park and R.S. Ruoff, *Nature Nanotech.* **4**, 217-224 (2009).

50. S. Stankovich; D.A. Dikin; G.H.B. Dommett; K.M. Kohlhaas; E.J. Zimney; E.A. Stach; R.D. Piner; S.T. Nguyen and R.S. Ruoff, *Nature* **442**, 282-286 (2006).

51. S. Stankovich; D.A. Dikin; R.D. Piner; K.A. Kohlhaas; A. Kleinhammes; Y. Jia; Y. Wu; S.T. Nguyen and R.S. Ruoff, *Carbon* **45**, 1558-1565 (2007).

52. K.S. Subrahmanyam; L.S. Panchakarla; A. Govindaraj and C.N.R. Rao, *J. Phys. Chem. C* **113**, 4257-4259 (2009).

53. N. Liu; F. Luo; H. Wu; Y. Liu; C. Zhang and J. Chen, *Adv. Func. Mater.* **18**, 1518-1525 (2008).

54. M. Choucair; P. Thordarson and J.A. Stride, *Nature Nanotech.* **4**, 30-33 (2009).

55. J.T. Robinson; J.S. Burgess; C.E. Junkermeier; S.C. Badescu; T.L. Reinecke; F.K. Perkins; M.K. Zalalutdniov; J.W. Baldwin; J.C. Culbertson; P.E. Sheehan and E.S. Snow, *Nano Lett.* **10**, 3001-3005 (2010).

56. N.P. Guisinger; G.M. Rutter; J.N. Crain; P.N. First and J.A. Stroscio, *Nano Lett.* **9**, 1462-1466 (2009).

57. R. Balog; B. Jørgensen; L. Nilsson; M. Andersen; E. Rienks; M. Bianchi; M. Fanetti; E. Lægsgaard; A. Baraldi; S. Lizzit; Z. Sljivancanin; F. Besenbacher; B. Hammer; T.G. Pedersen; P. Hofmann and L. Hornekær, *Nature Mater.* **9**, 315-319 (2010).

58. D. Elias; R. Nair; T. Mohiuddin; S. Morozov; P. Blake; M. Halsall; A. Ferrari; D. Boukhvalov; M. Katsnelson; A. Geim and others, *Science* **323**, 610 (2009).

59. R. Balog; B. Jrgensen; J. Wells; E. Lgsgaard; P. Hofmann; F. Besenbacher and L. Hornekr, *J. Am. Chem. Soc.* **131**, 8744-8745 (2009).

60. M.M. Ugeda; Brihuega I; F. Guinea and J.M. Gómez-Rodríguez, *Phys. Rev. Lett.* **104**, 096804 (2010).

61. M. Han; B. Özyilmaz; Y. Zhang and P. Kim, *Phys. Rev. Lett.* **98**, 206805 (2007).

62. L. Tapaszto; G. Dobrik; P. Lambin and L. Biro, *Nature Nanotech.* **3**, 397-401 (2008).

63. M. Wang; L. Fu; L. Gan; C. Zhang; M. Rümmeli; A. Bachmatiuk; K. Huang; Y. Fang and Z. Liu, *Sci. Rep.* **3**, 1238 (2013).

64. J. Bai; X. Zhong; S. Jiang; Y. Huang and X. Duan, *Nature Nanotech.* **5**, 190-194 (2010).

65. O. Aktrk and M. Tomak, *Appl. Phys. Lett.* **96**, 081914 (2010).

66. H. Huang; S. Chen; X. Gao; W. Chen and A.T.S. Wee, *ACS Nano* **3**, 3431-3436 (2009).

67. W. Chen; S. Chen; D.C. Qi; X.Y. Gao and A.T.S. Wee, *J. Am. Chem. Soc.* **129**, 10418-10422 (2007).

68. T. Ohta; A. Bostwick; T. Seyller; K. Horn and E. Rotenberg, *Science* **313**, 951-954 (2006).

69. A.L. Walter; K.J. Jeon; A. Bostwick; F. Speck; M. Ostler; T. Seyller; L. Moreschini; Y.S. Kim; Y.J. Chang; K. Horn and E. Rotenberg, *Appl. Phys. Lett.* **98**, 184102 (2011).

70. I. Gierz; T. Suzuki; R.T. Weitz; D.S. Lee; B. Krauss; C. Riedl; U. Starke; H. Höchst; J.H. Smet; C.R. Ast and K. Kern, *Phys. Rev. B* **81**, 235408 (2010).

71. C. Virojanadara; S. Watcharinyanon; A. Zakharov and L. Johansson, *Phys. Rev. B* **82**, 205402 (2010).

72. C. Riedl; C. Coletti; T. Iwasaki; A.A. Zakharov and U. Starke, *Phys. Rev. Lett.* **103**, 246804 (2009).

73. R.R. Nair; W. Ren; R. Jalil; I. Riaz; V.G. Kravets; L. Britnell; P. Blake; F. Schedin; A.S. Mayorov; S. Yuan; M.I. Katsnelson; H.M. Cheng; W. Strupinski; L.G. Bulusheva; A.V. Okotrub; I.V. Grigorieva; A.N. Grigorenko; K.S. Novoselov and A.K. Geim, *Small* **6**, 2877-2884 (2010).

74. L. Zhao; R. He; K.T. Rim; T. Schiros; K.S. Kim; H. Zhou; C. Gutierrez; S.P. Chockalingam; C.J. Arguello; L. Palova; D. Nordlund; M.S. Hybertsen; D.R. Reichman; T.F. Heinz; P. Kim; A. Pinczuk; G.W. Flynn and A.N. Pasupathy, *Science* **333**, 999-1003 (2011).

75. X. Lanfei; Xiao Wang; L. Jiong; N. Zhenhua; L. Zhiqiang; M. Hongying; W. Rui; W. Yingying; H. Han; Q. Dongchen; L. Rong; Y. Ting; S. Zexiang; W. Tom; P. Haiyang; Ö. Barbaros; L. Kianping; W. Andrew T. S.; Ariando and C. Wei, *Appl. Phys. Lett.* **98**, 193113 (2011).

76. J. Balakrishnan; K. G.W.K; M. Jaiswal; A.H. Castro Neto and B. Özyilmaz, *Nature Phys.* **9**, 284-287 (2013).

77. L. Xie; X. Wang; J. Lu; Z. Ni; Z. Luo; H. Mao; R. Wang; Y. Wang; H. Huang; D. Qi and others, *Appl. Phys. Lett.* **98**, 193113 (2011).

78. N.S. Safron; A.S. Brewer and M.S. Arnold, *Small* **7**, 492-498 (2011).

79. Y. Gong; M. Long; G. Liu; S. Gao; C. Zhu; X. Wei; X. Geng; M. Sun; C. Yang; L. Lu and L. Liu, *Phys. Rev. B* **87**, 165404 (2013).

80. Y.R. Kang; Y.L. Li and M.Y. Deng, *J. Mater. Chem.* **22**, 16283-16287 (2012).

81. D. Wei; L. Xie; K.K. Lee; Z. Hu; S. Tan; W. Chen; C.H. Sow; K. Chen; Y. Liu and A.T.S. Wee, *Nat. Commun.* **4**, 1374 (2013).

82. M.Y. Han; J.C. Brant and P. Kim, *Phys. Rev. Lett.* **104**, 056801 (2010).

83. P. Gallagher; K. Todd and D. Goldhaber-Gordon, *Phys. Rev. B* **81**, 115409 (2010).

84. H. Huang; D. Wei; J. Sun; S.L. Wong; Y.P. Feng; A.H.C. Neto and A.T.S. Wee, *Sci. Rep.* **2**, 983 (2012).

85. Y.C. Chen; D.G. de Oteyza; Z. Pedramrazi; C. Chen; F.R. Fischer and M.F. Crommie, *ACS Nano* ASAP Article (2013).

86. J. Cai; P. Ruffieux; R. Jaafar; M. Bieri; T. Braun; S. Blankenburg; M. Muoth; A.P. Seitsonen; M. Saleh; X. Feng; K. Müllen and R. Fasel, *Nature* **466**, 470 (2010).

87. P. Wei; N. Liu; H.R. Lee; E. Adijanto; L. Ci; B.D. Naab; J.Q. Zhong; J. Park; W. Chen; Y. Cui and Z. Bao, *Nano Lett.* **13**, 1890-1897 (2013).

88. H.G. Jee; J.H. Han; H.N. Hwang; B. Kim; H.S. Kim; Y.D. Kim and C.C. Hwang, *Appl. Phys. Lett.* **95**, 093107 (2009).

89. V.W. Brar; R. Decker; H.M. Solowan; Y. Wang; L. Maserati; K.T. Chan; H. Lee; Ç.O. Girit; A. Zettl; S.G. Louie; M.L. Cohen and M.F. Crommie, *Nature Phys.* **7**, 43-47 (2010).

90. Y. Wang; V.W. Brar; A.V. Shytov; Q. Wu; W. Regan; H.Z. Tsai; A. Zettl; L.S. Levitov and M.F. Crommie, *Nature Phys.* **8**, 653-657 (2012).

91. C. Riedl; C. Coletti and U. Starke, *J. Phys. D: Appl. Phys.* **43**, 374009 (2010).

92. M. Cranney; F. Vonau; P.B. Pillai; E. Denys; D. Aubel; M.M. De Souza; C. Bena and L. Simon, *EPL* **91**, 66004 (2010).

93. B. Premlal; M. Cranney; F. Vonau; D. Aubel; D. Casterman; M.M. De Souza and L. Simon, *Appl. Phys. Lett.* **94**, 263115-263115 (2009).

94. N. Koch, *ChemPhysChem* **8**, 1438-1455 (2007).

95. L.L. Chua; J. Zaumseil; J...F. Chang; E.C.W. Ou; P.K.H. Ho; H. Sirringhaus and R.H. Friend, *Nature* **434**, 194-199 (2005).

96. S.R. Forrest, *MRS Bull.* **30**, 28-32 (2005).

97. J. Mao; H. Zhang; Y. Jiang; Y. Pan; M. Gao; W. Xiao and H.J. Gao, *J. Am. Chem. Soc.* **131**, 14136 (2009).

98. G.I. Cárdenas-Jirón; P. Leon-Plata; D. Cortes-Arriagada and J.M. Seminario, *J. Phys. Chem. C* **115**, 16052-16062 (2011).

99. C. Coletti; C. Riedl; D.S. Lee; B. Krauss; L. Patthey; K. von Klitzing; J.H. Smet and U. Starke, *Phys. Rev. B* **81**, 235401 (2010).

100. J.T. Sun; Y.H. Lu; W. Chen; Y.P. Feng and A.T.S. Wee, *Phys. Rev. B* **81**, 155403 (2010).

101. N. Karousis; J. Ortiz; K. Ohkubo; T. Hasobe; S. Fukuzumi; Á. Sastre-Santos and N. Tagmatarchis, *J. Phys. Chem. C* **116**, 20564-20573 (2012).

102. Y. Jiang; Y. Lu; X. Lv; D. Han; Q. Zhang; L. Niu and W. Chen, *ACS Catal.* **3**, 1263-1271 (2013).

103. M.Z. Hossain; M.A. Walsh and M.C. Hersam, *J. Am. Chem. Soc.* **132**, 15399 (2010).

104. C.K. Chan; T.E. Beechem; T. Ohta; M.T. Brumbach; D.R. Wheeler and K.J. Stevenson, *J. Phys. Chem. C* **117**, 12038-12044 (2013).

105. H.Y. Mao; Y.H. Lu; J.D. Lin; S. Zhong; A.T.S. Wee and W. Chen, *Prog. Surf. Sci.* **88**, 132-159 (2013).

106. W.H. Lee; J. Park; S.H. Sim; S. Lim; K.S. Kim; B.H. Hong and K. Cho, *J. Am. Chem. Soc.* **133**, 4447-4454 (2011).

107. S. Lee; S.J. Kang; G. Jo; M. Choe; W. Park; J. Yoon; T. Kwon; Y. Ho Kahng; D.Y. Kim; B. Hun Lee and T. Lee, *Appl. Phys. Lett.* **99**, 083306 (2011).

108. J. Wu; H.A. Becerril; Z. Bao; Z. Liu; Y. Chen and P. Peumans, *Appl. Phys. Lett.* **92**, 263302 (2008).

109. H. Park; S. Chang; M. Smith; S. Gradečak and J. Kong, *Sci. Rep.* **3**, 1581 (2013).

110. M. Garnica; D. Stradi; S. Barja; F. Calleja; C. Díaz; M. Alcamí; N. Martín; A.L. Vázquez de Parga; F. Martín and R. Miranda, *Nature Phys.* **9**, 368-374 (2013).

111. E. Bekyarova; S. Sarkar; S. Niyogi; M.E. Itkis and R.C. Haddon, *J. Phys. D: Appl. Phys.* **45**, 154009-154009 (2012).

112. W.H. Lee; J.W. Suk; H. Chou; J. Lee; Y. Hao; Y. Wu; R. Piner; D. Akinwande; K.S. Kim and R.S. Ruoff, *Nano Lett.* **12**, 2374-2378 (2012).

113. J. Sadowski; Y. Fujikawa; K. Kelly; K. Nakayama; T. Sakurai; E. Mickelson; R. Hauge and J. Margrave, *J. Cryst. Growth* **229**, 580-585 (2001).

114. S. Barja; M. Garnica; J.J. Hinarejos; A.L. Vázquez de Parga; N. Martín and R. Miranda, *Chem. Commun.* **46**, 8198 (2009).

115. J. Ren; S. Meng; Y.L. Wang; X.C. Ma; Q.K. Xue and E. Kaxiras, *J. Chem. Phys.* **134**, 194706 (2011).

116. H.G. Zhang; J.T. Sun; T. Low; L.Z. Zhang; Y. Pan; Q. Liu; J.H. Mao; H.T. Zhou; H.M. Guo; S.X. Du; F. Guinea and H.J. Gao, *Phys. Rev. B* **84**, 245436 (2011).

117. Y. Gao; Y. Zhang; J. Ren; D. Li; T. Gao; R. Zhao; Y. Yang; S. Meng; C. Wang and Z. Liu, *Nano Res.* **5**, 543-549 (2012).

118. S.K. Hämäläinen; M. Stepanova; R. Drost; P. Liljeroth; J. Lahtinen and J. Sainio, *J. Phys. Chem. C* **116**, 20433-20437 (2012).

119. H.G. Jee; J.H. Han; H.N. Hwang; B. Kim; H.S. Kim; Y.D. Kim and C.C. Hwang, *Appl. Phys. Lett.* **95**, 093107 (2009).

120. S. De Feyter and F.C. De Schryver, *Chem. Soc. Rev.* **32**, 139-150 (2003).

121. C. Faul and M. Antonietti, *Adv. Mater.* **15**, 673-683 (2003).

122. L.J. Prins; D.N. Reinhoudt and P. Timmerman, *Angew. Chem. Int. Ed.* **40**, 2382-2426 (2001).

123. P.J.M. Lehn, *Angew. Chem. Int. Ed.* **29**, 1304-1319 (1990).

124. J.V. Barth, *Annu. Rev. Phys. Chem.* **58**, 375-407 (2007).

125. Y.L. Huang and A.T.S. Wee, *Langmuir* **26**, 3329-3334 (2009).

126. Y.L. Huang; W. Chen and A.T.S. Wee, *J. Am. Chem. Soc.* **133**, 820-825 (2011).

127. Y.L. Huang; W. Chen; H. Li; J. Ma; J. Pflaum and A.T.S. Wee, *Small* **6**, 70-75 (2010).

128. J. Lu; P.S.E. Yeo; Y. Zheng; Z. Yang; Q. Bao; C.K. Gan and K.P. Loh, *ACS Nano* **6**, 944-950 (2012).

129. A. Varykhalov; W. Gudat and O. Rader, *Adv. Mater.* **22**, 3307-3310 (2010).

Chapter 2: Experimental

2.1 Scanning Tunnelling Microscopy/Spectroscopy

Since the invention of the STM by Binnig and Rohrer in 1982, the ability to image the surface with atomic precision has open up numerous research possibilities at the nanoscale.[1-5] Because graphene is two dimensional, STM is ideal for its characterization and many STM studies on graphene have been performed.[6-9] STM is able to probe important local physical and electronic details of both pristine and modified epitaxial graphene that other techniques are unable to access on the atomic scale.

In our experiments, low temperature scanning tunnelling microscopy (LT-STM) was carried out in a custom-built multichamber ultra high vacuum (UHV) system with base pressure lower than 1×10^{-10} mbar, which houses an Omicron LT-STM interfaced to a Nanonis controller (Nanonis, Switzerland).[10] Analysis of the STM images was carried out using the WSxM software.[11] The UHV environment is required to ensure that the rate of contamination of the surface is relatively low during the time scale of the *in situ* experiments. All STM imaging were carried out at 77K which is maintained by liquid nitrogen. The low temperature of the STM environment minimizes thermal diffusion of molecules on the surface which improves image quality as well as minimizes thermal broadening of electron energy states. The voltage bias is applied at the tip with the substrate grounded. Shown in Fig. 2.1 is the equipment used where the different chambers are labelled accordingly. Molecular deposition is carried out through thermal evaporation from effusion cells in the growth chamber and the STM experiments are carried out *in situ* within the adjoining chamber.

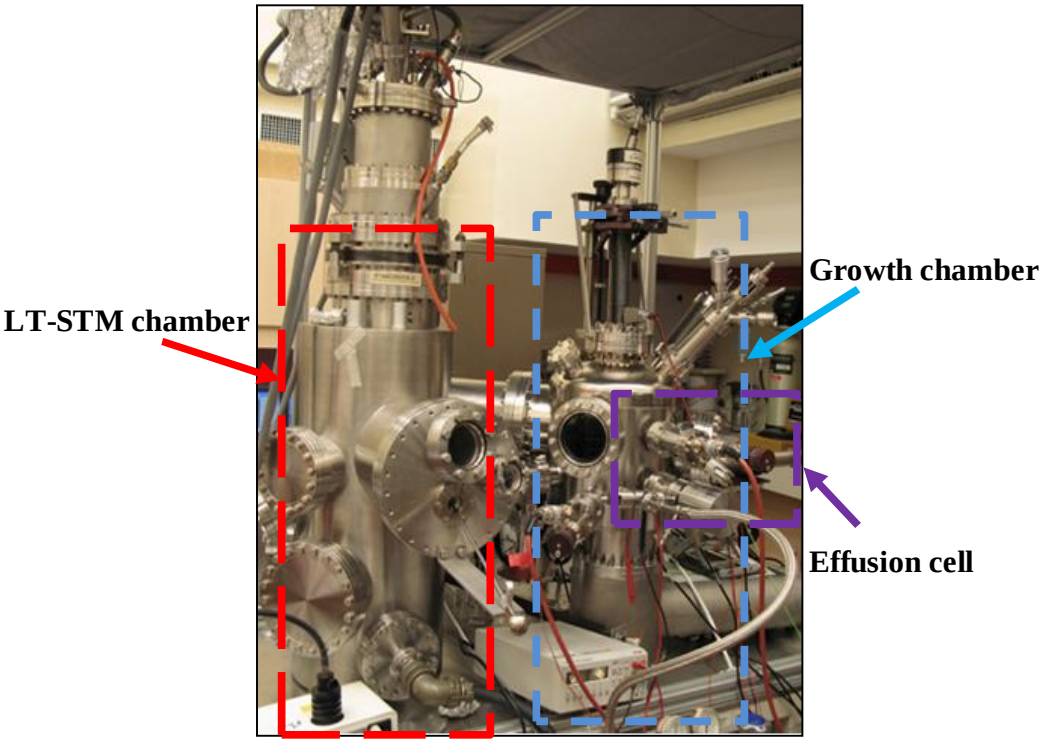

Figure 2.1 Photograph of multi-chamber UHV system used for LT-STM experiment.

2.1.1 Basic Operating Principles of STM

Quantum mechanical tunnelling of electrons between substrate surface and tip through a potential barrier posed by the empty space between them forms the basis of STM. Tunnelling occurs when the distance between the two is sufficiently close (in the range of nanometre scale) and a bias potential (a few milli-eV to a few eV) is applied across them. The tunnelling probability can be calculated using the Fermi golden rule, the barrier between tip and surface being approximated as a series of square potential wells described by the Wentzel–Kramers–Brillouin approximation.[12] The tunnelling probability is given by:

$$T\left(E,eV,r\right)\propto \exp\left(-\frac{2z\sqrt{2m}}{\hbar}\sqrt{\frac{\phi_s+\phi_t}{2}+\frac{eV}{2}-E}\right) \quad (2.1)$$

where E is the energy of the electronic state, m is the mass of the electron, z, is the distance between tip and surface, and ϕ_s, ϕ_t are the work functions of the sample and tip respectively. The potential barrier can be approximated by the term $\phi=\frac{\phi_s+\phi_t}{2}$ which is the average of the two work functions of the tip and substrate. The resultant tunnelling current that passes through the tip is therefore exponentially dependent on the distance between tip and sample surface, giving the STM its atomic resolution.

Due to the changes in tunnelling current with differing tip-surface distances as the tip is raster scanned across the surface, the spatial variation in surface topography and/or electronic structure of individual atoms and molecules can be observed. The tunnelling current that is received will be amplified and sent to the controller that further interprets the data in terms of the variations in height of the surface. In order to obtain atomic resolution in the scans, the motions of the tip in both vertical and lateral dimensions are required to be atomically precise. This is achieved by mounting it on a piezoelectric material which is highly mechanically sensitive to small changes in voltage bias applied in different directions across it.

The scanning of the tip has two modes. The constant current mode is one in which the tunnelling current is kept constant using a feedback loop as the tip scans. As the current increases (decreases) during the scan, the feedback loop instructs the tip to retract (approach) the surface. In this manner, the current received by the tip is kept

constant. The recorded variation in tip height with tip position is then translated as an STM topography image. Another mode is the constant height mode. In this mode, the current is allowed to vary as the tip is scanned across the surface while maintaining the original vertical configuration of the tip at the start of the scan. The variation in current as the tip scans is recorded as the STM image. For the experiments described in this thesis, the constant current mode is always used to obtain maximal resolution. A schematic of the STM working principle for both modes is shown in Figure 2.2a and b.

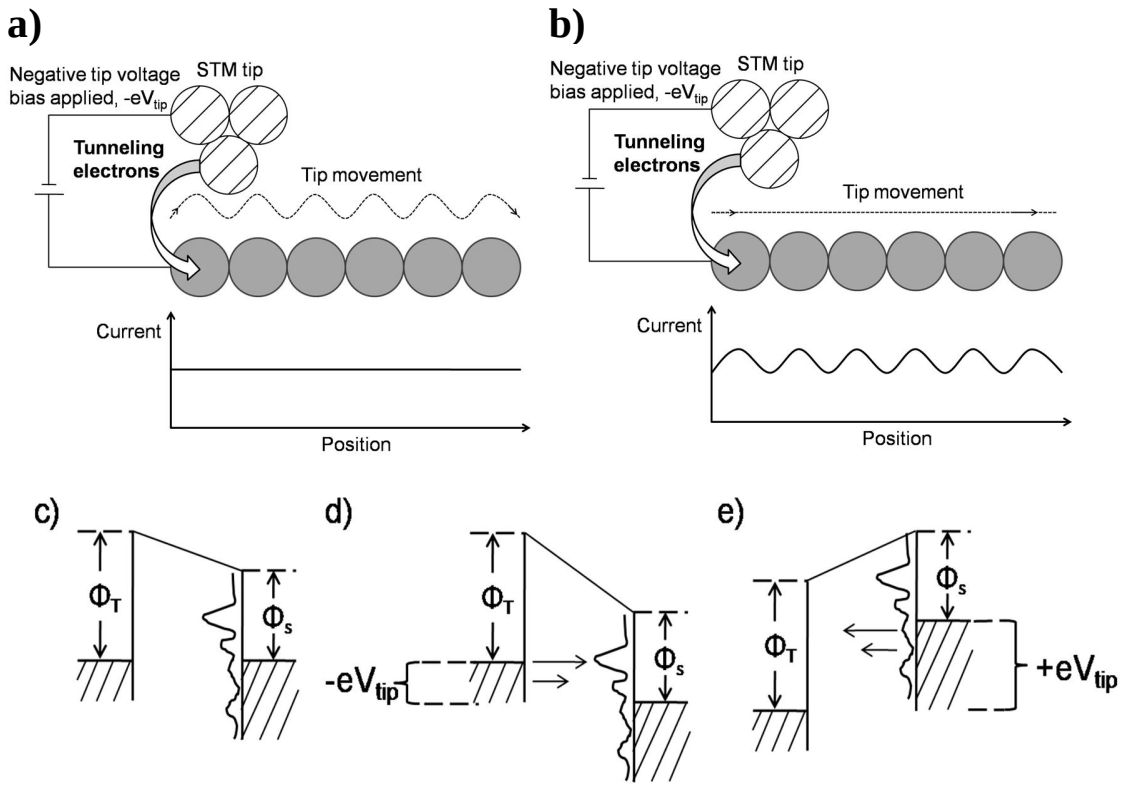

Figure 2.2 (a–b)Schematics of a scanning tunnelling microscope in (a) constant-current and (b) constant-height modes. (c–e)Energy level diagrams for the sample and tip, where Φ_s and Φ_T represent the corresponding work functions. The dashed lines are the vacuum levels, the solid horizontal lines are the Fermi levels below which sample states are occupied and the wiggly curve represent the sample density of states (DOS) (c) sample and tip at thermal equilibrium, separated by a small vacuum gap, with zero applied voltage bias; (d) same as (c) but with negative tip bias;(e) same as (c) but with positive tip bias, Figures (c)–(e) adapted from Reference 13.

In addition to the tip-surface distance, the tunnelling current involves a convolution of other factors and the current, I, obtained with an applied voltage bias, V, can be described by the equation:

$$I = \frac{4\pi}{\hbar}\int_{0}^{eV}\left[f\left(E_{\mathrm{F}} - eV + \varepsilon\right) - f\left(E_{\mathrm{F}} + \varepsilon\right)\right]\rho_s\left(r, E_{\mathrm{F}} + \varepsilon\right)\rho_t\left(r, E_{\mathrm{F}} - eV + \varepsilon\right)Td\varepsilon \qquad (2.2)$$

where ρ_s and ρ_t are the density of states of the surface and tip respectively as a function of position, r, and energy, ε, with respect to the Fermi level, E_{F}, of the metal electrodes. The Fermi level is defined as the energy at which the weighted density of states is half. The Fermi Dirac distribution function, *f*, reflects the occupancy of the electronic levels at a given temperature. The applied voltage bias determines the electronic energy range relative to the Fermi level over which tunnelling occurs. Thus, the tunnelling current is dependent on the convolution of the surface topography and electronic states of both tip and sample involved in tunnelling. In addition, the occupancy of the involved electronic states determines whether tunnelling is possible between tip and sample.

When the applied voltage bias is small, eV << ϕ, the density of states of the metallic tip, $\rho_t\left(r,(E - eV)\right)$, can be approximated to be a constant in a small energy range about the Fermi level. In addition, the barrier height can be assumed to be independent of V due to the relatively small bias. At low temperatures of 77K, we can assume the Fermi Dirac distribution as a step function. Taking these into consideration, Equation 2.2 can be simplified to give:

$$I = \frac{4\pi}{\hbar}\rho_t(0)\exp\left(-\frac{2z\sqrt{2m\phi}}{\hbar}\right)\int_0^{eV}\rho_s(r,E)\,dE \qquad (2.3)$$

Therefore, when STM measurements are performed, the obtained image is dependent on both the number of electronic states involved in tunnelling and the tip-sample distance.

The energy level diagrams of Figure 2.2d-f describe the electronic states which are involved in tunnelling.[13] In Figure 2.2d, when the tip and sample are brought close enough, a thermal dynamical equilibrium is reached and the Fermi level between the tip and sample is aligned. However, no tunnelling current occurs if no voltage bias is applied. In Figure 2.2e, when the tip (sample) voltage bias is negative (positive) with respect to the sample (tip), the Fermi level at the tip is shift to a higher energy than that of the sample. Electrons therefore tunnel from the occupied electronic states of the tip to the unoccupied electronic states in the sample surface. When the bias is reversed in Figure 2.2f, the Fermi level of the sample is now higher than that of the tip and electrons then tunnel from the occupied electronic states of the sample into the available electronic states of the tip.

For molecules, the electronic states have discrete energy levels known as molecular orbitals. In addition, the electron probability distributions associated with these molecular orbitals of different binding energies have well defined spatial distributions and shapes. This results in a variation of the tunnelling conductance as the tip is moved over different positions of an individual molecule which enables the mapping of a single molecule in real space with atomic precision. This allows us to identify specific molecules and their molecular orientations on the surface as well as their relation with the

underlying graphene lattice vectors. The interactions of the molecules and graphene can also be picked up by any variations in their molecular appearance when deposited on graphene.

2.1.2 Scanning Tunnelling Spectroscopy

The local density of states at the atomic scale can be measured by using a technique called STS. STS can probe the local electronic structure of both molecules and graphene and changes due to intermolecular and molecule-substrate interactions. This is achieved by measuring the differential tunnelling conductance (dI/dV). From Equation 2.3, we know that the tunnelling current is proportional to the number of electronic states involved in the tunnelling process. A negative tip (sample) bias would involve the density of states of the sample above (below) the Fermi level and vice versa. Taking the derivative of equation 2.3, we get:

$$\frac{\mathrm{d}I}{\mathrm{d}V} \propto \rho_s\left(r, eV\right) \tag{2.4}$$

Hence, the density of states which reflects the electronic structure can be obtained through the differential tunnelling conductance. During STS, the tip-sample distance is kept constant by removing the constant-current feedback loop. Following which, the voltage bias applied is then varied. The variation in current is measured and the current obtained is differentiated with respect to the applied voltage. The signal to noise ratio of doing this derivative numerically is small. Instead, a sinusoidal voltage modulation is introduced on top of the voltage bias applied during STS. The voltage modulation is small compared to the voltage bias applied. This ensures a negligible influence on the

tunnelling current. The frequency of the modulation is selected to be higher than the scanning rate to minimize interference of the topography obtained due to the voltage modulation during image acquisition. The first harmonic of the modulated current is then extracted and it is representative of the differential tunnelling conductance.

STS studies of graphene have been performed in numerous reports but a linear dependence of the DOS of monolayer graphene with energy is rarely observed, even though the conductance is directly proportional to the LDOS probed. Instead of tending to zero, the conductance at the Dirac point is represented by a local minima instead of a complete absence of conductance. Though the density of states of graphene tends to zero at the Dirac point, there are still electrons tunnelling from the underlying substrate in that region, contributing to a finite conductance being observed. Furthermore, electrons tunnelling from graphene to the tip and vice versa at low energies close to the Fermi level are suppressed due to the short decay length of the electron wave.[8] This occurs as the decay length is inversely proportional to the large in-plane crystal momentum ($k \approx 1.7 Å^{-1}$) of the graphene low energy electronic states involved in the tunnelling process. Thus, tunnelling can only occur via virtual excitations with the assistance of phonons to electronic states near the Γ point with $k \approx 0 Å^{-1}$ which have longer decay lengths. As the phonon requires a certain energy to be activated for tunnelling to occur, the conductance spectra is zero at the Fermi level while it begins to increase from zero once the tip bias applied satisfies the phonon activation energy required, further disrupting the ideal linearity of the conductance curve. In addition, as seen in equation 2.3, the condition of the STM tip also influences the conductance and hence overall shape of the curve.

2.2 Photoemission Spectroscopy

STM/STS allows us to observe the influence of the molecules on the physical and electronic structure of graphene at the local atomic scale with maximal scan sizes of 344 nm, but does not provide a complete picture of the electronic structure of the molecule-graphene system. In contrast, photoemission spectroscopy (PES) probes the changes to the electronic structure of graphene over a larger area (~ mm^2). Thus, core level PES, near edge x-ray adsorption fine structure (NEXAFS) and angular resolved photoemission spectroscopy (ARPES) measurements based on synchrotron radiation were carried out at the Surface, Interface and Nanostructure Science (SINS) beam line in the Singapore Synchrotron Light Source (SSLS)[14] as well as at the soft x-ray spectroscopy beam line at the Australian Synchrotron.[15] Shown in Fig 2.3a is the SINS beam line where the PES measurements of Chapter 3 are carried out while Figure 2.3b[16] describes a typical PES setup.

The photon energies used for each measurement is calibrated using the Fermi level (E_F) and Au $4f_{7/2}$ core level located at 84.4eV binding energy from an Ar sputter-cleaned poly gold reference sample. A hemispherical R4000 electron analyser records the kinetic energy of the detected photoelectrons and has an energy resolution of 50meV. The intensities of the spectra were normalized using the total incoming photon flux measured with a gold mesh in the path of the incoming beam. The photon beams used in the NEXAFS measurements are P – polarized (electric field of the incident ray lies in the same plane as the incident ray and the surface normal). Data obtained is compiled and analysed using the IgorPro software.

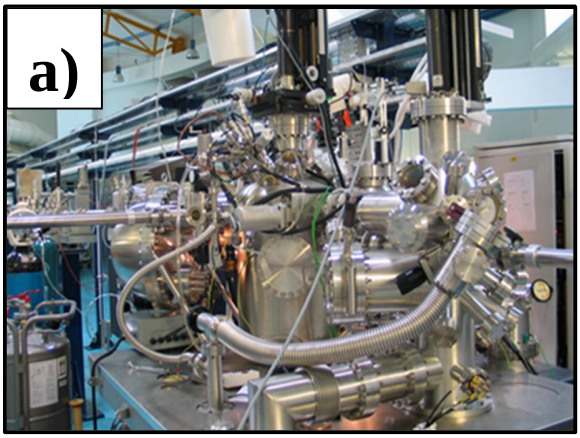

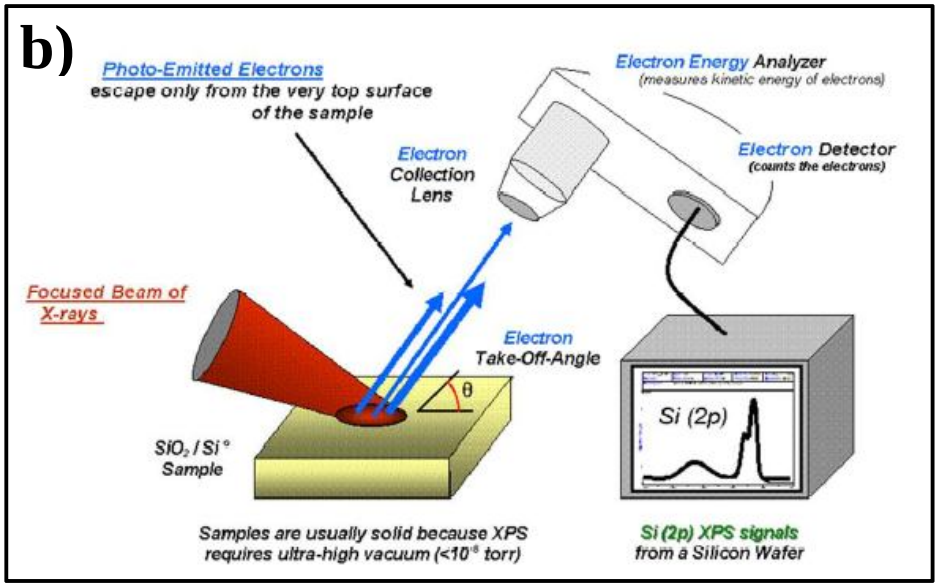

Figure 2.3 a) Photograph of SINS beam line at Singapore Synchrotron Light Source facility. b) A typical experimental setup for PES measurements. Figure 2.3b is reproduced from Reference 16.

2.2.1 Working Principle of Synchrotron Based PES Measurements

When electrons are accelerated at velocities close to the speed of light are forced to bend in their trajectories by strong magnetic fields, extremely bright radiation consisting a range of photon energies is continuously given off in a narrow cone in the

direction tangent to the electron orbit. Suitable photon energies are selected using a monochromator comprising four interchangeable spherical gratings capable of delivering tunable photons in the range of 50-110 eV, 110-220 eV, 220-440 eV and 440-1200 eV respectively.[14] During PES measurements, the photoemission event can be simplified and decomposed into a three step model[17] as described in Figure 2.4.[18] It includes i) optical excitation between the initial and final bulk Bloch eigenstates, ii) travel of the excited electron to the surface and iii) escape of the photoelectron into vacuum after transmission through the surface potential barrier.

During core level PES measurements, the incoming photon beam excites an electron in the core level of the atoms. If the energy of the photon beam is sufficient to overcome the binding energy and the work function of the sample, ϕ_s, the excited electron then travels through the sample and escapes from its surface to the vacuum.[19] The kinetic energy of the ejected electron is then measured by the analyser. The kinetic energy thus measured varies with both the binding energy (B.E) of the electron and the energy of the incident beam as shown in the equation below.

$$\text{B.E} = h\nu - \text{K.E} - \phi_a \qquad (2.5)$$

where K.E is the kinetic energy of the received photoelectrons, $h\nu$ is the energy of the incident photons, and ϕ_{a} is the work function (4.3eV) of the analyser used as the sample and analyser share a common electrical ground.

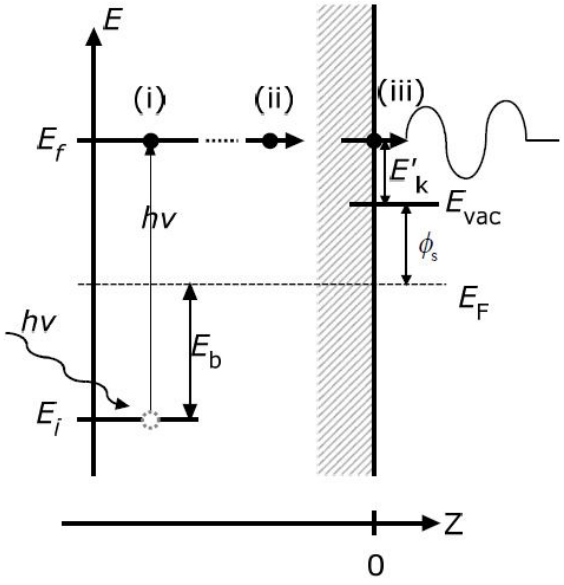

Figure 2.4 Illustration of a three-step model in photoemission process; (i) photoexcitation of an electron from an initial state to a final state; (ii) transport of excited electrons to the surface; (iii) escape from surface to vacuum. Figure 2.4 is reproduced from reference 18.

By employing equation 2.5, the binding energy of the electrons in the atoms and its associated element from which it was ejected from can be identified. From the shifts in the original binding energies of the various core level peaks or introduction of new ones as the amount of deposited material increases, we can detect the change in chemical environment of both the deposited material and the substrate, and the presence of any charge transfer between them. In addition, the intensity of the detected photoelectrons is directly proportional to the number of atoms probed, hence providing quantitative analysis of the amount of each species present in the sample.

Another advantage of using PES measurements is the high surface sensitivity of the measurements. During the photoemission process, not all photoelectrons are detected by the analyser. Many of them lose their energy through inelastic scattering processes as they travel through the substrate. The scattering processes are highly dependent on the

kinetic energies of the electrons. At low kinetic energies, the electrons do not possess sufficient energy to initiate scattering processes while at higher energies, the cross section of scattering is low. The escape depth or inelastic mean free path of the electron varies as a function of its kinetic energy as shown in the 'universal curve' of Figure 2.5.[20] We note that the escape depth of electrons with kinetic energies between 50 to 500eV is only a few angstroms, indicating that PES measurements probe only the first few layers of the substrate. The surface sensitivity can be further enhanced by increasing the angles away from the surface normal at which the photoemission electrons are detected, i.e. increasing the distance through which the detected photoelectrons have to travel.

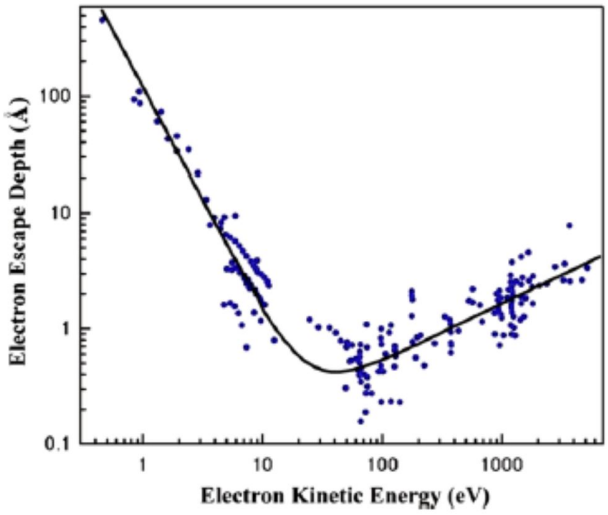

Figure 2.5 Typical electron escape depth as a function of its kinetic energy. Figure is reproduced with permission from reference 20. © 1979 Heyden & Son Ltd.

From the attenuation of the substrate associated photoelectron signal, one can then deduce the nominal thickness of the adsorbates deposited on the substrate surface by assuming a layer by layer growth mode of the layer:

$$I_d = I_0 \exp(\frac{-d}{\lambda \cos\theta}) \qquad (2.6)$$

For epitaxial graphene on SiC (0001), the attenuation of the Si 2p core level substrate signal is used. I_d is the photoelectron intensity after a film of thickness d is deposited, I_0 is the unattenuated photoelectron intensity prior to deposition, θ is the angle between analyser and the surface normal. λ (nm) is the inelastic mean free path of electrons in the molecular layer which is dependent on both electron kinetic energy, E_{kin} and density, ρ (in g/cm^3), of the organic film. It is approximated according the empirical relation[20]:

$$\lambda = (49E_{\text{kin}}^{-2} + 0.11E_{\text{kin}}^{1/2}) / \rho \qquad (2.7)$$

In addition, as the number of photoelectrons produced is proportional to the number of atoms of the said element present in the sample, the peak areas associated with the different chemical species can be used to determine their relative abundance after proper fits of the data are performed. However, one needs to note that each element also has its own photoemission sensitivity factor which is dependent on the incoming photon energy and is unique to specific electron orbitals of the element. Thus, the measured peak area is normalised against their respective sensitivity factors as well as the number of scans taken before comparing their relative abundance. Uncertainty of these measurements can be approximated from the difference in area between the fitted peaks and the actual data that is obtained.

2.2.2 NEXAFS

NEXAFS measurements, unlike PES measurements where free electrons ejected from the core levels are directly detected, involve transitions of photoexcited electrons from a core level to an unoccupied state above the Fermi level.[21] In addition, the photon energies of the beam are continuously varied during NEXAFS measurements unlike PES

where the beam energy is kept to a single value during data acquisition. The photo-excitation between the states is based on electric dipole transition and hence dependent on both the difference in energy levels between the two states as well as the extent of alignment between the electric field of the incoming photon beam and the electronic orbitals that are being probed.

The NEXAFS of the C K edge performed on graphene is used as an example and the processes involved during photon absorption are shown in Figure 2.5. When the varying photon energy matches the energy difference between the C1s states in the carbon atom and one of the anti-bonding states, π^* and σ^*, present in graphene is matched, a transition of electrons from the C1s state to one of these anti-bonding states occurs, leaving behind a hole in its C1s state. The core hole resulting from the absorption process can be filled via an Auger process. In an Auger process, an electron of a higher energy level would occupy the vacant state and, if the energy difference between the levels is sufficient, will excite another electron to be ejected from the sample. Conversely, the capture of an electron from a state of higher energy can result in emission of a fluorescent photon. The difference between NEXAFS and traditional photoemission experiments is that in the latter, the initial photoelectron itself is measured (Section 2.2.1), while in NEXAFS the fluorescent photon, Auger electron or inelastically scattered photoelectron is recorded.

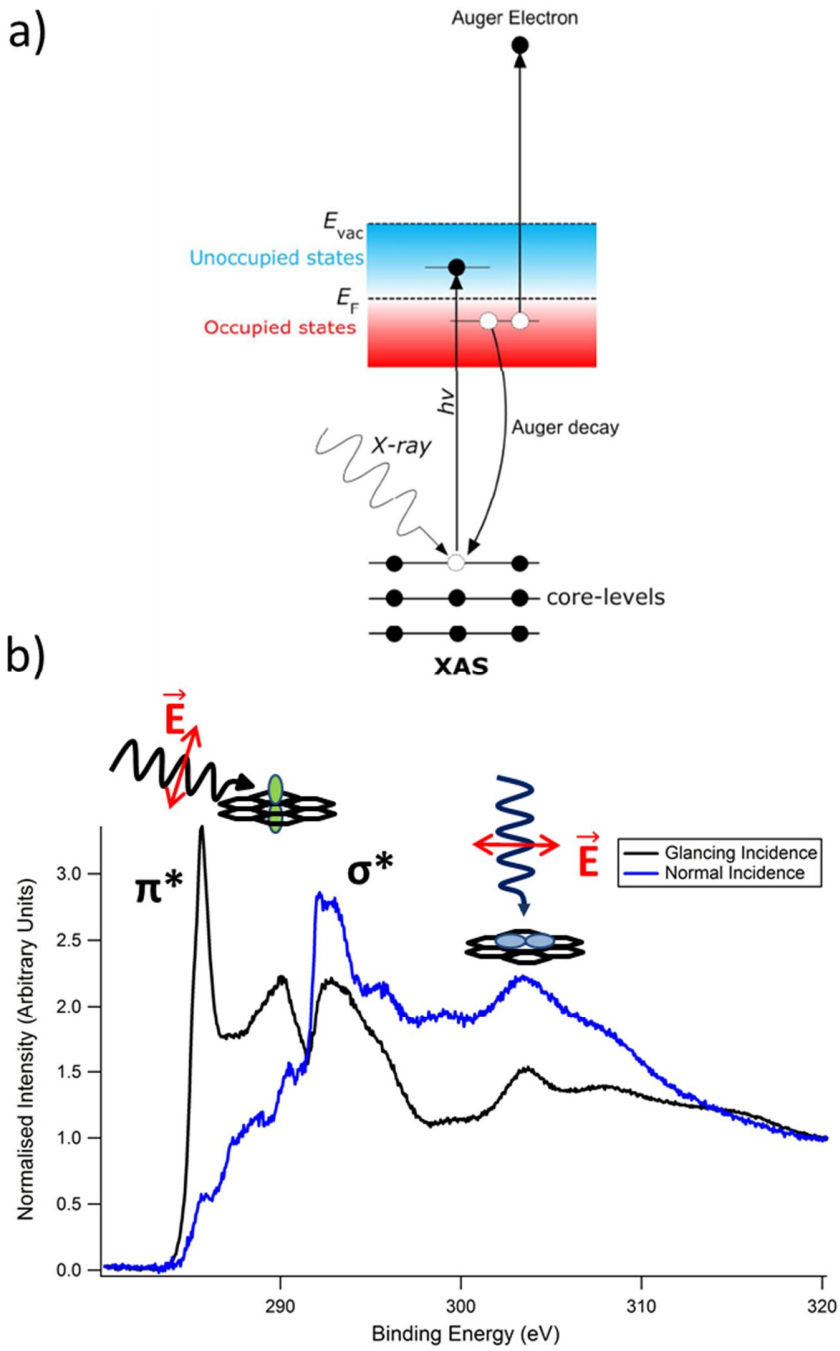

Figure 2.5 a) Photoemission processes involved in NEXAFS. b) Polarization dependent NEXAFS spectra of graphene, illustrating the capability to determine orientations of chemical bonds in graphene. (Black spectra) π* state intensity is maximised when incoming beam is at glancing angle to surface. (Blue spectra) Intensity of σ* states are maximised when incoming beam is aligned with surface normal. Figure a) is adapted with permission from Reference 18.

However, the orbitals of the π* anti-bonding states and σ* anti-bonding states are orthogonal to each other. π* anti-bonding orbitals are out of plane (aligned with the surface normal) while the σ* anti-bonding states are in plane. Therefore, the amount of electrons excited as well as intensity of detected ejected electrons is dependent on the extent of alignment of the P polarized electric field of the incoming photon beam and the orbitals. When the angle of beam incidence changes from a normal to a glancing one, we would expect to observe a change in intensities that is angular dependent as the π* and σ* anti-bonding states are orthogonal to each other.

Therefore, NEXAFS measurements are conducted at different angles to determine the orientation of the probed orbitals. NEXAFS thus allows probing of the anti-bonding states as well as their orientations. The variation in intensity with the above mentioned factors are exemplified in a NEXAFS measurement for pristine graphene in Figure 2.5b. When the π* anti-bonding states are aligned maximally with the electric field of the polarized incoming photon beam at a glancing incidence, the intensity is much higher than that associated with the σ* anti-bonding states and vice versa when the incident beam is impinging along the surface normal.

2.2.3 ARPES

During photoemission events, the electrons are ejected from the probed material and escape into the vacuum in all directions. By detecting these electrons with an analyser with well-defined acceptance angles in ARPES measurements,[22] one can determine the wave-vector or momentum of these free photoelectrons with mass, *m*, in vacuum through its kinetic energy, E_{kin} : $\boldsymbol{K} = \sqrt{2mE_{kin}}/\hbar$ with their components perpendicular (z direction) and parallel (x, y direction) to the surface:

$$\boldsymbol{K}_x = \frac{1}{\hbar}\sqrt{2mE_{kin}}\sin\theta\cos\phi \tag{2.8}$$

$$\boldsymbol{K}_y = \frac{1}{\hbar}\sqrt{2mE_{kin}}\sin\theta\cos\phi \tag{2.9}$$

$$\boldsymbol{K}_z = \frac{1}{\hbar}\sqrt{2mE_{kin}}\cos\theta \tag{2.10}$$

The polar (ϑ) and azimuthal (φ) emission angles of the electron are defined by the experimental setup and the geometry is shown in Figure 2.6a.[22]

Since the binding energy of the electron can be measured from the magnitude of its kinetic energy as described in Equation 2.5, to determine the electronic band dispersion from the emission angles of the electron, one has to consider the momentum conservation of the photoexcited electrons. As the electrons enter the vacuum from the material surface, it only experiences a potential change in the surface normal direction. Thus, only the parallel component of its momentum is conserved in the process and its modulus is described as:

$$\left|\boldsymbol{K}_{\parallel}\right| = \frac{1}{\hbar}\sqrt{2mE_{kin}}\sin\theta \qquad (2.11)$$

For the case of graphene, which is a two dimensional material, the uncertainty in the $\boldsymbol{K}_{\perp}$ is not relevant as graphene has negligible dispersion along the surface normal and its electronic dispersion is solely determined by $\boldsymbol{K}_{\parallel}$. Thus, one can map out the electronic band dispersion by determining the binding energies of the photoexcited electrons as a function of $\boldsymbol{K}_{\parallel}$ that is derived from the electron take off angles from the sample surface. This is particularly useful in observing the electronic changes of graphene when it interacts with the deposited molecules and is demonstrated in Chapter 5.

For ARPES measurements, the orientation of the Brilluoin zone with respect to the analyser has to be calibrated before carrying out the experiments. This is done by first using low energy electron diffraction (LEED) to locate the reciprocal lattice of graphene and therefore orientation of the Brilluoin zone with respect to the electron analyser. The azimuthal angle of the sample is then rotated to place the entrance slit of the analyser perpendicular to the Γ-K direction, as shown in Figure 2.6b. The obtained electronic band dispersion would hence be perpendicular to the Γ-K direction of the Brilluoin Zone. In this work, photon energies of 60eV are used to probe the electronic states close to the Fermi level, up to about 2eV in binding energy. The Dirac point of graphene is determined by doing ARPES measurements at different polar angles about the approximated position of the K point and then locating the correct polar angle at which the linear bands of graphene cross. The intensity of the bands are normalised against the photoelectron signals obtained about the Fermi edge of a gold reference sample in the same chamber.

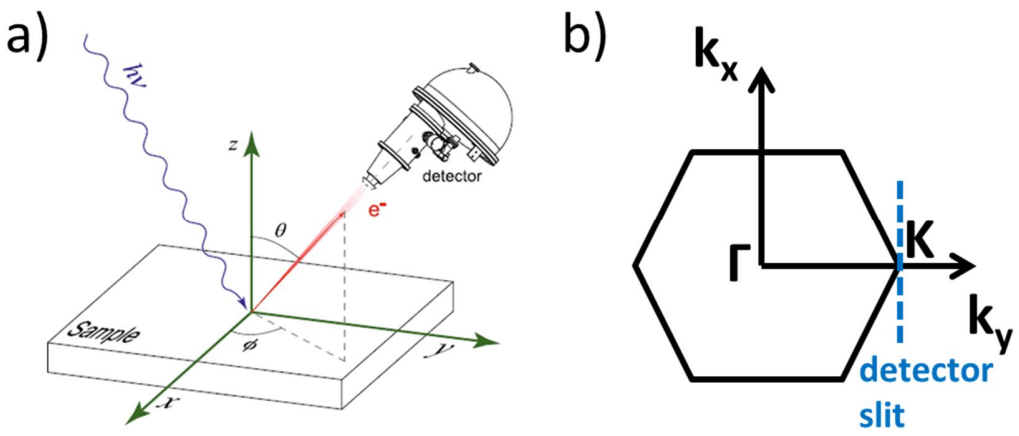

Figure 2.6 a) Geometry of ARPES measurements. b) Brilluoin zone of graphene with location of detector slit placed perpendicular to Γ – K direction indicated. Figure a) is reproduced from reference 22.

2.3 Epitaxial Graphene Grown from Silicon Carbide

As mentioned in the previous chapter, there are several methods used in the fabrication of graphene, some of which include mechanical exfoliation, chemical vapour deposition on metal substrates and also reduction of graphene oxides.[23] In particular, those grown on hexagonal SiC (0001) wafers provide a means for integration in existing device technology.[24-28] The type of graphene that is chosen for the experiment is epitaxially grown from the Si face of silicon carbide, SiC (0001). This is because the entire epitaxial graphene sheet grown on the Si face of SiC (0001) possesses the same orientation due to its formation process which involves a sequential detachment of the buffer layer from the substrate surface. The single crystal orientation of the graphene that is grown allows ease of STM and ARPES measurements. In contrast, the graphene grown from the C-face is turbostratic in nature that results in graphene domains with different crystallographic orientations and therefore not the subject of our investigations.[29]

The size of the epitaxial graphene grown is only limited by the dimensions of the SiC wafer used, allowing STM measurements to easily locate where graphene is as well as ensuring that the surface area probed by the photon beam in PES measurements is covered with graphene to minimize undesired contributions from the non-graphitized areas. The SiC wafer used is also highly doped and hence conductive due to intrinsic impurities, thereby preventing charging effects during PES measurements as well as providing a conductive substrate on which STM can be performed. The 4H silicon carbide polytype wafer used for graphene growth is commercially bought (Cree Inc.) and the Si-face of the substrate is used for graphene growth through graphitization under ultra-high vacuum conditions.[25,27,30] Epitaxial graphene on SiC (0001) used in our experiments are grown ex-situ in a separate UHV chamber before transferring to our LT-STM system. All samples are then thoroughly degassed at 1000°C to remove contaminants and checked under STM for cleanliness before the experiments are conducted.

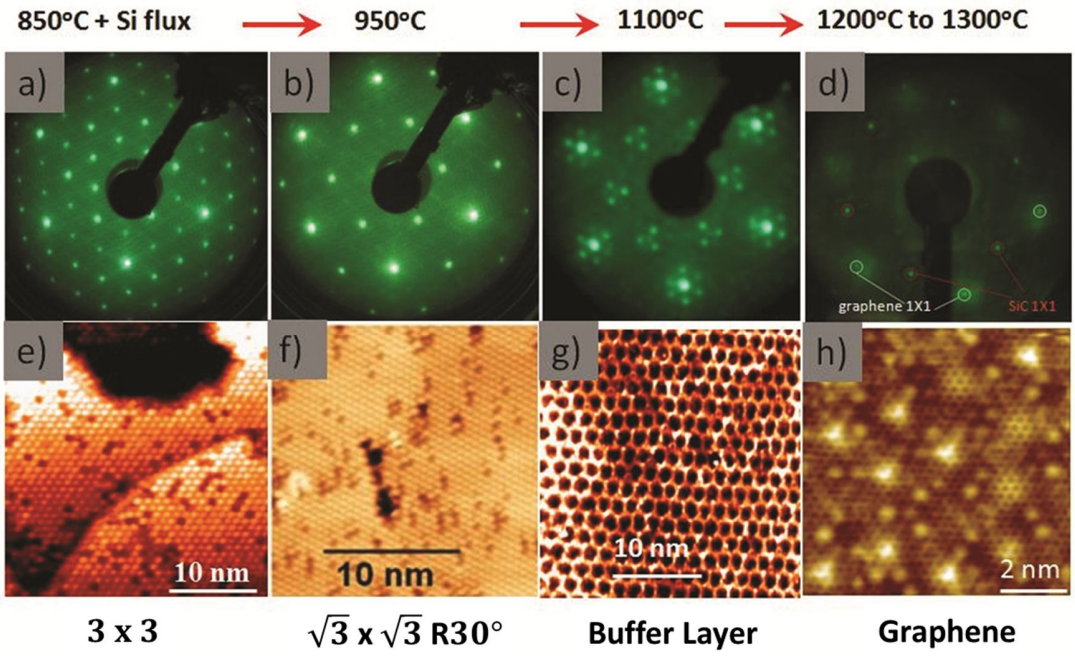

Figure 2.7 Series of STM and LEED images of the different stages of graphene growth on SiC(0001) a) and e) 3 x 3 Si rich reconstruction. b) and f) $\sqrt{3}$ x $\sqrt{3}$R30° Si rich surface reconstruction. c) and g) Buffer layer with $6\sqrt{3}$ x $6\sqrt{3}$R30° surface reconstruction. d) and h) Epitaxial monolayer graphene. Figures a) – h) are reproduced with permission from reference 31. © 2009 Elsevier Ltd.

Figure 2.7 describes the growth process of graphene on SiC (0001) with the corresponding (LEED) and STM images of the surface.[31] Firstly, the SiC substrate is annealed overnight at 700°C to allow outgassing of adsorbed impurities. Heating of the SiC substrate takes place by passing a current directly through it. As the resistance of the substrate is in the kΩs, the heat generated from the passing current can reach the temperatures required for graphene growth. The temperature of the sample is measured using an optical pyrometer. After degassing, the substrate is then heated at 900°C while under a silicon flux from a nearby Si source to remove any native oxides that are present. This procedure also produces a Si-rich 3 x 3 surface reconstruction as shown in Figure

2.7a. Following which, the temperature is raised to 1000°C and the surface is now transformed to a $\sqrt{3}$ x $\sqrt{3}$ reconstruction in as shown in Figure 2.7b.

As the temperature reaches 1100°C, a layer of carbon atoms is thus formed in Figure 2.7c and is termed the buffer layer. The buffer layer is made up of honey-comb structures of carbon atoms but has no π electron dispersion band as a third of the carbon atoms are bonded to the Si atoms of the SiC substrate below it, resulting in the buffer layer being an insulator. The buffer layer possesses a $(6\sqrt{3}$ x $6\sqrt{3})$R30° reconstruction with respect to the underlying SiC substrate that is equivalent to a 13 x 13 graphene unit cell of the same lattice vectors. After heating to a temperature of 1250°C, the bonds between the carbon and silicon atoms are broken and the released buffer layer is now transformed to graphene and displays its characteristic linear band dispersion. In its place, another buffer layer is formed. As the temperature increases beyond that (>1300°C), the buffer layer is once again detached and a larger number of graphene layers start to develop in sequence, with bilayer graphene starting to develop at 1300°C and so on. Note that the buffer layer always exists regardless of the number of graphene layers that are grown and can be imaged through the overlaying graphene layers by STM.

Such sequential bottom up formation of epitaxial graphene results in all the graphene layers having the same crystal orientation within the layer as well as between layers.[32] The graphene layers that are grown are of high atomic quality and can run continuously over step edges.[6,33] However, due to the presence of silicon dangling bonds in the buffer layer, the as grown monolayer graphene is highly electron doped in the region of ~10^{13} electrons cm^{-2}.[25,30] The Dirac point of pristine epitaxial graphene on SiC is therefore at 0.45eV below the Fermi level.[34] The doping level decreases with the

number of graphene layers with bilayer graphene having its Dirac point at 0.3eV below the Fermi level.[25] The doping from the buffer layer as well as its interaction with graphene greatly reduces the electron mobility in graphene.[35-37] Compared to mechanically exfoliated graphene with an electron mobility of up to 250,000 $cm^2V^{-1}s^{-1}$,[23] epitaxial graphene on Si-face of SiC can only manage values of 2000 $cm^2V^{-1}s^{-1}$.[28] Furthermore, the mobility is highly dependent on substrate temperature due to extensive phonon involved scattering induced by the presence of the buffer layer.[36] This issue will be addressed in Chapter 3 where intercalation is carried out to remove the buffer layer.

References

1. G. Binnig and H. Rohrer, *Rev. Mod. Phys.* **59**, 615-625 (1987).

2. G. Binning; H. Rohrer; C. Gerber and E. Weibel, *Phys. Rev. Lett.* **49**, 57-61 (1982).

3. R. Wiesendanger, *Scanning tunneling microscopy III: theory of STM and related scanning probe methods* (Springer-Verlag, 1993).

4. H. J. Güntherodt, R. Wiesendanger, *Scanning tunneling microscopy I: general principles and applications to clean and adsorbate-covered surfaces* (Springer-Verlag, 1994).

5. H. J. Güntherodt, R. Wiesendanger, *Scanning tunneling microscopy II: further applications and related scanning techniques* (Springer, 1995).

6. S.L. Wong; H. Huang; W. Chen and A.T. Wee, *MRS Bull.* **37**, 1195-1202 (2012).

7. Y. Wang; V.W. Brar; A.V. Shytov; Q. Wu; W. Regan; H.Z. Tsai; A. Zettl; L.S. Levitov and M.F. Crommie, *Nature Phys.* **8**, 653-657 (2012).

8. Y. Zhang; V.W. Brar; F. Wang; C. Girit; Y. Yayon; M. Panlasigui; A. Zettl and M.F. Crommie, *Nature Phys.* **4**, 627-630 (2008).

9. V. Brar; Y. Zhang; Y. Yayon; T. Ohta; J. McChesney; A. Bostwick; E. Rotenberg; K. Horn and M. Crommie, *Appl. Phys. Lett.* **91**, 122102 (2007).

10. S.L. Wong; H. Huang; Y.L. Huang; Y.Z. Wang; X.Y. Gao; T. Suzuki; W. Chen and A.T.S. Wee, *J. Phys. Chem. C* **114**, 9356-9361 (2010).

11. I. Horcas; R. Fernandez; J.M. Gomez-Rodriguez; J. Colchero; J. Gomez-Herrero and A. M. Baro, *Rev. Sci. Instrum.* **78**, 013705 (2007).

12. S. Lindsay, *Introduction to Nanoscience* (Oxford University Press, 2010).

13. R.J. Hamers, *Annu. Rev. Phys. Chem.* **40**, 531-559 (1989).

14. X.J. Yu; O. Wilhelmi; H.O. Moser; S.V. Vidyaraj; X.Y. Gao; A.T.S. Wee; T. Nyunt; H.J. Qian and H.W. Zheng, *J. Electron Spectrosc. Rela. Phenom.* **144**, 1031-1034 (2005).

15. K.J. Rietwyk; M. Wanke; H.M. Vulling; M.T. Edmonds; P.L. Sharp; Y. Smets; Q.H. Wu; A. Tadich; S. Rubanov; P.J. Moriarty; L. Ley and C.I. Pakes, *Phys. Rev. B* **84**, 035404 (2011).

16. X-ray photoelectron spectroscopy in *Wikipedia* Retrieved June 23, 2013, from http://en.wikipedia.org/wiki/X-ray_photoelectron_spectroscopy

17. C. N. Berglund and W. E. Spicer, *Phys. Rev.* **136**, A1030 (1964).

18. Qi D. *Organic molecules on diamond (001): a synchrotron study.* (Doctoral Dissertation). Retrieved from ScholarBank@NUS. (Accession Order no. 2010-04-08T11:03:32Z)

19. A. Einstein, *Ann. Phys.* **17**, 132 (1905).

20. M.P. Seah and W.A. Dench, *Surf. Interface Anal.* **1**, 2-11 (1979).

21. J. Stöhr, *NEXAFS Spectroscopy* (Springer Berlin, 1992).

22. W. Zhang, *Photoemission Spectroscopy on High Temperature Superconductor A Study of Bi2Sr2CaCu2O8 by Laser-Based Angle-Resolved Photoemission* (Springer Theses, 2013).

23. A. Geim, *Science* **324**, 1530-1534 (2009).

24. C. Berger; Z. Song; X. Li; X. Wu; N. Brown; C. Naud; D. Mayou; T. Li; J. Hass; A.N. Marchenkov; E.H. Conrad; P.N. First and W.A. de Heer, *Science (New York, N.Y.)* **312**, 1191-1196 (2006).

25. T. Ohta; A. Bostwick; T. Seyller; K. Horn and E. Rotenberg, *Science* **313**, 951-954 (2006).

26. C. Berger; X. Wu; P. First; E. Conrad; X. Li; M. Sprinkle; J. Hass; F. Varchon; L. Magaud; M. Sadowski; M. Potemski; Martinez G. and de Heer W.A., *Adv. Solid State Phys.* **47**, 145-157 (2008).

27. C. Riedl and U. Starke, *Phys. Rev. B* **76**, 245406 (2007).

28. K.V. Emtsev; A. Bostwick; K. Horn; J. Jobst; G.L. Kellogg; L. Ley; J.L. McChesney; T. Ohta; S.A. Reshanov; J. Röhrl; E. Rotenberg; A.K. Schmid; D. Waldmann; H.B. Weber and T. Seyller, *Nature Mater.* **8**, 203-207 (2009).

29. D. Siegel; C. Hwang; A. Fedorov and A. Lanzara, *Phys. Rev. B* **81**, 241417 (2010).

30. C. Riedl; A.A. Zakharov and U. Starke, *Appl. Phys. Lett.* **93**, 033106 (2008).

31. W. Chen; D. Qi; X. Gao and A.T.S. Wee, *Prog. Surf. Sci.* **84**, 279-321 (2009).

32. P. First; W. De Heer; T. Seyller; C. Berger; J. Stroscio and J. Moon, *MRS Bull.* **35**, 296-305 (2010).

33. H. Huang; W. Chen; S. Chen and A.T.S. Wee, *ACS Nano* **2**, 2513-2518 (2008).

34. S.Y. Zhou; G.H. Gweon; A.V. Fedorov; P.N. First; W.A. de Heer; D.H. Lee; F. Guinea; A.H. Castro Neto and A. Lanzara, *Nature Mater.* **6**, 770 (2007).

35. C. Riedl; C. Coletti; T. Iwasaki; A.A. Zakharov and U. Starke, *Phys. Rev. Lett.* **103**, 246804 (2009).

36. F. Speck; J. Jobst; F. Fromm; M. Ostler; D. Waldmann; M. Hundhausen; H.B. Weber and T. Seyller, *Appl. Phys. Lett.* **99**, 122106 (2011).

37. K.V. Emtsev; F. Speck; T. Seyller and L. Ley, *Phys. Rev. B* **77**, 155303 (2008).

Chapter 3: $C_{60}F_{48}$ on Epitaxial Graphene

3.1 Introduction

As mentioned in the previous chapter, there exist limitations in the usage of epitaxial graphene on SiC (0001) due to the high intrinsic electron doping ($\approx 10^{13}$ cm^{-2})[1,2] and lower electron mobility ($\approx$ 2000 $cm^2V^{-1}s^{-1}$).[3] These properties are purportedly due to the underlying $(6\sqrt{3}\ x\ 6\sqrt{3})R30$ reconstructed interfacial or buffer layer below the graphene layer.[2,4,5] For applications in devices, it is thus favourable if the doping level is reduced or the influence of the buffer layer on the overlying graphene is removed. The intrinsic electron doping can be reduced via deposition of electron withdrawing p-type dopants to lower the Fermi level. Organic molecules have been used as a surface transfer doping agent of graphene in numerous studies.[6-8] However, their packing arrangement as well as electronic and chemical interactions that these dopants have on graphene and vice versa on the atomic scale have not been studied in depth. For example, F_4-TCNQ, a commonly used p-type dopant, is not suitable for STM measurements unless deposited on highly modulated graphene grown on metals[9], as it has a high diffusion rate under the STM due to their intermolecular repulsion after charge transfer with graphene as well as their low molecular weight (276.15). For our experiments, the molecule $C_{60}F_{48}$[10-12] is employed. It is a well-known strong electron accepting dopant that has been used in surface doping of hydrogen terminated diamond with a doping extent of up to a single electron per molecule.[13] $C_{60}F_{48}$, having a larger molecular weight (1632.57) and hence being more stable under scanning conditions, makes it a suitable candidate for our studies of the properties and self-assembly of these p-type dopants when deposited on graphene.

Other than doping graphene, one can also remove the underlying buffer layer by introducing suitable intercalates. This has been performed using hydrogen, lithium, oxygen and fluorine intercalation which breaks the Si-C bonds holding the buffer layer and forms Si-F bonds in the case of fluorine, in turn converting it into graphene.[14-17] Intercalated products have been intensively studied using PES and Low Energy Electron Microscopy (LEEM) measurements[14-17] but local STM experiments have not been carried out to study the nanoscale effects that fluorine intercalation has on graphene and the interfacial layer. Fluorination of graphene has also been studied intensively both experimentally and theoretically recently.[18-21] Thus, it would be of interest to investigate the nature of fluorination of the graphene layer during the intercalation process. In this aspect, the $C_{60}F_{48}$ molecules that we are using can also serve as a fluorinating agent. It has been known to fluorinate the reactive Si (111) surface at room temperature[22,23] and also diamond surfaces when irradiated with synchrotron radiation of 800 eV photon energy.[24] This allows us to use these fluorinated fullerenes, with proper annealing parameters, as a fluorine source for the intercalation of the buffer layer on SiC (0001) to decouple it from the substrate by forming a graphene layer with a passivized interface. Such an intercalation process is also much safer than the usage of the traditional fluorinating agent, XeF_2 which is highly corrosive and toxic when vaporized.

In this chapter, we first discuss the self-assembly of these molecules on epitaxial graphene and the nature of their topographical appearance under STM. Following which, we investigate the changes that occur when $C_{60}F_{48}$ is used to introduce fluorine intercalates into the interface between the buffer layer and the underlying substrate. Successful fluorine intercalation was demonstrated and two states, namely semi-

intercalated graphene and quasi-freestanding graphene are formed at different annealing temperatures. The electronic and physical features of these new layers as well as associated nanostructures are measured using STM and STS. The fluorine intercalated model is further corroborated using synchrotron PES and the presence of an interfacial Si-F beneath the graphene is confirmed.

3.2 Experimental Setup

A 4H-SIC (0001) sample having surfaces containing both epitaxial monolayer graphene and buffer layer surface in equal coverage was used in the intercalation process. A reference 4H-SiC (0001) sample having a monolayer epitaxial graphene was also prepared and measured using PES to act as a reference. Both samples were grown via graphitization under ultrahigh vacuum conditions as described in Chapter 2 and the surface cleanliness was confirmed using STM before deposition of molecules was carried out. Fluorinated fullerene, $C_{60}F_{48}$ (95% purity, Term USA), was utilized. A monolayer of $C_{60}F_{48}$ was first deposited via evaporation from a Knudsen cell at 110°C with the sample kept at room temperature and then checked under LT-STM for purity and quality of the molecular layer. The properties of the self-assembled molecular layer were also studied prior to sample annealing and the molecules were also deposited on highly ordered pyrolytic graphite (HOPG) for comparison.

Fluorine intercalation was carried out by passing a direct current through the molecular covered graphene sample for an initial annealing at approximately 120°C to allow fluorine migration from the molecule to the interface below the buffer layer. A slightly higher temperature of about 150°C was applied through the same method to achieve a semi-intercalated stage. The same annealing method was then carried out at a

higher temperature of 850°C to complete the decoupling process. If annealing at 850°C was first performed without an initial annealing at 120°C, no decoupling or significant change of the graphene surface was observed. LT-STM and STS was carried out in-situ after each stage of molecular deposition and annealing to analyse the morphological and electronic properties of the thus-formed decoupled epitaxial graphene layer. The scanning is performed in constant current mode using a chemically etched tungsten tip. Core level PES was used to verify the structural and electronic changes of the sample after intercalation. The PES measurements were performed at the SINS beamline at the Singapore Synchrotron Light Source with a resolution of 0.05eV. Photon energy used for the Si 2p and C 1s spectra were 140eV and 350eV respectively. F 1s spectrum was obtained using a photon energy of 750eV.

3.3 Self-assembly of $C_{60}F_{48}$ on epitaxial graphene

Figure 3.1 shows epitaxial graphene before and after molecular deposition. As indicated in Figure 3.1a, the surface is made up of both monolayer graphene and the buffer layer as identified by the absence of the graphene honeycomb structure on the buffer layer at low tip bias (< 0.5 V).[25] The defects represented by the white objects are carbon clusters inherent on the buffer layer. In Figure 3.1b, after molecular deposition, the as-deposited sub monolayer of $C_{60}F_{48}$ molecules forms a hexagonal closed packed layer on graphene, with each spherical object representing a single $C_{60}F_{48}$ molecule. One particular D3 isomer of the fluorinated fullerene is shown in Figure 3.1f. We note that the molecules follow a layer by layer growth mode as there is no second layer observed prior to the complete formation of the first monolayer.

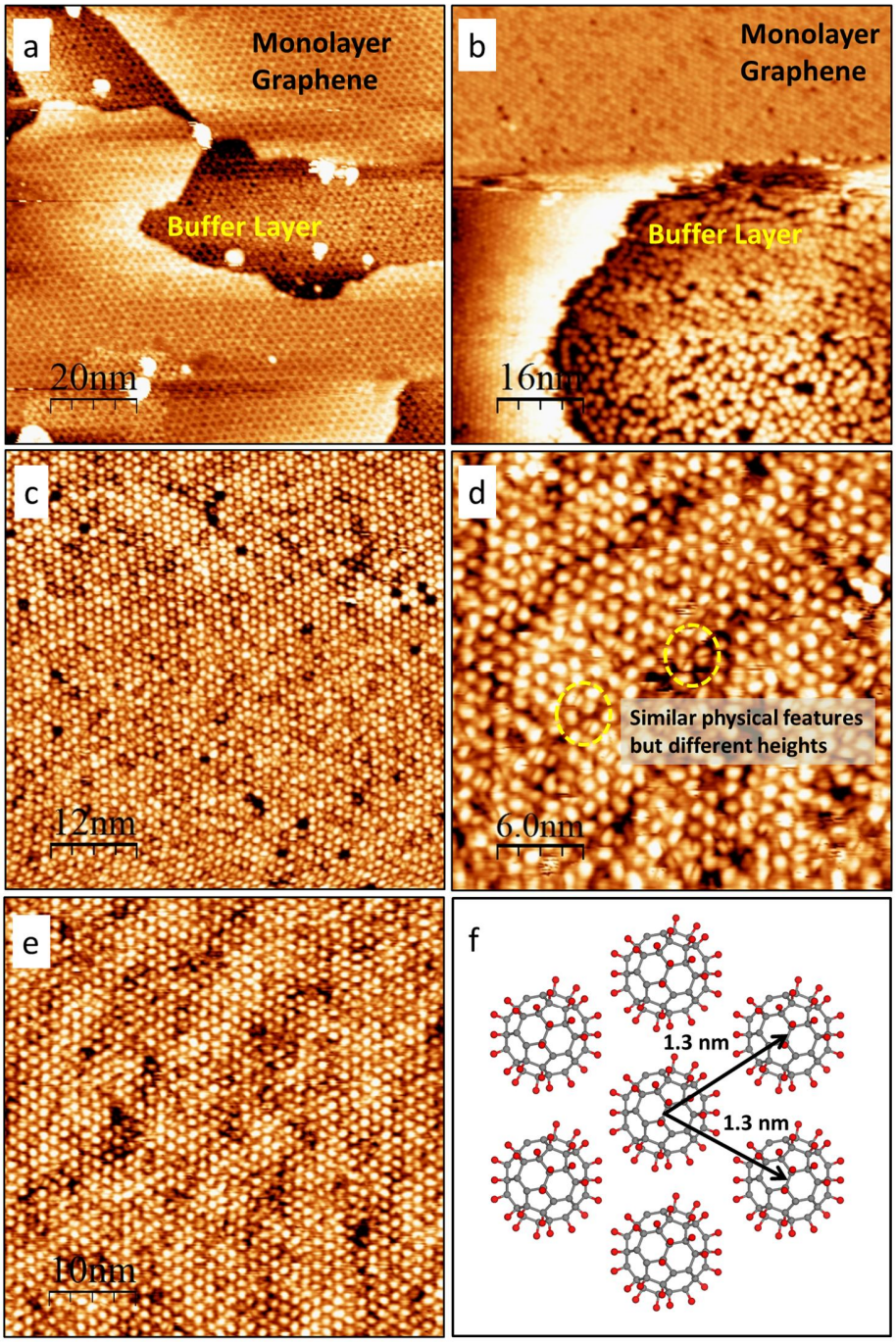

Figure 3.1 a) 150 x 150 nm^2 STM image showing bare buffer layer and graphene surface prior to deposition. (V_{tip} = -2.0V, I = 100pA) b) 80 x 80 nm^2 STM image of surface, (top) graphene and (bottom) buffer layer , covered by $C_{60}F_{48}$ (V_{tip} = -3.0V, I = 100pA). c) 60 x 60 nm^2 STM image of close packed $C_{60}F_{48}$ molecules (V_{tip} = -3.1V, I = 85pA).. d) 30 x 30 nm^2 STM image showing $C_{60}F_{48}$ monolayer with molecules with similar physical features (circled in yellow) but with different height (V_{tip} = -3.0V, I = 85pA). e) $C_{60}F_{48}$ monolayer on HOPG (V_{tip} = -3.1V, I = 85pA). f) Schematic showing packing structure of molecules.

The lattice parameters of the molecular layer as shown in the model of Figure 3.1f are given by a = b = 1.3 ± 0.1 nm, with an angle of 60 ± 2° between them. Due to the close packed arrangement, there are no observable domain boundaries within the molecular layer. As expected, unlike F_4-TCNQ, where the intermolecular repulsion and their low molecular weight renders scanning difficult, the $C_{60}F_{48}$ layer is stable under scanning conditions. On the buffer layer, the molecules are observed to adsorb in a disordered arrangement. This is likely to be due to higher molecular adsorption energy on the buffer layer which limits the diffusivity of the molecules and hence their ability to form close packed films.

In Figure 3.1c, we observe that the individual molecules deposited on graphene have different topographical contrast, despite being on the same terrace. The molecules themselves display two different internal structures, one being a simple featureless sphere and another showing up as a bean-like structure. These topographical fine features are most likely due to the different orientation of the molecules. Regardless of internal structural details, two molecules (as indicated in Figure 3.1d) with similar features possess distinct topographical contrast. We can thus exclude the possibility of the observed contrast being caused by differences in molecular orientation. In contrast, molecules deposited on the buffer layer do not display such variation, most likely due to the larger degree of adsorbate-substrate interaction in terms of charge transfer and a much stronger orbital overlapping which washes out individual variations in the appearance of the molecules under STM.

Deposition of $C_{60}F_{48}$ molecules are carried out on HOPG to ascertain the effects of a graphene substrate on the observed contrast and the deposited molecular layer is

shown in Figure 3.1e. The molecules are packed in the same arrangement as those on graphene with similar lattice parameters (within instrumental errors) of a = b = 1.3 ± 0.1 nm with the same included angle of 60 ± 2°. In addition, each individual molecule in the layer has the same random differences in perceived height when observed under STM. Thus, we can further exclude the influence of any variation in electronic properties on the molecular appearance within the graphene layer such as variation in doping levels.

Graphene has been measured to be slightly undulating across its surface.[26] In order to exclude any possible influence of minor height variations in the underlying graphene on the observed molecular height contrast, STM images of the same area were taken in succession with different tip biases applied and are shown in Figure 3.2. The indicated feature in Figure 3.2a acts as a reference point to ensure that the analysis region remains the same regardless of thermal drift. The root mean square (RMS) roughness is analysed at each bias voltage and is shown in the respective STM image panels. These values are indicative of the extent of variation in the molecular heights at different tip biases. We observe that the contrast between molecules increases with decreasing bias applied, with the largest RMS roughness of 0.89 ± 0.01Å obtained for Figure 3.2a at a bias of -1.9 V and a lowest RMS roughness of 0.56 ± 0.01Å measured at a bias of -3.4V for Figure 3.2e. Such a variation would not be possible if the underlying cause of the contrast is a purely topographical one. The change in contrast with increasing bias is likely to be due to a variation in electronic states involved in tunnelling.

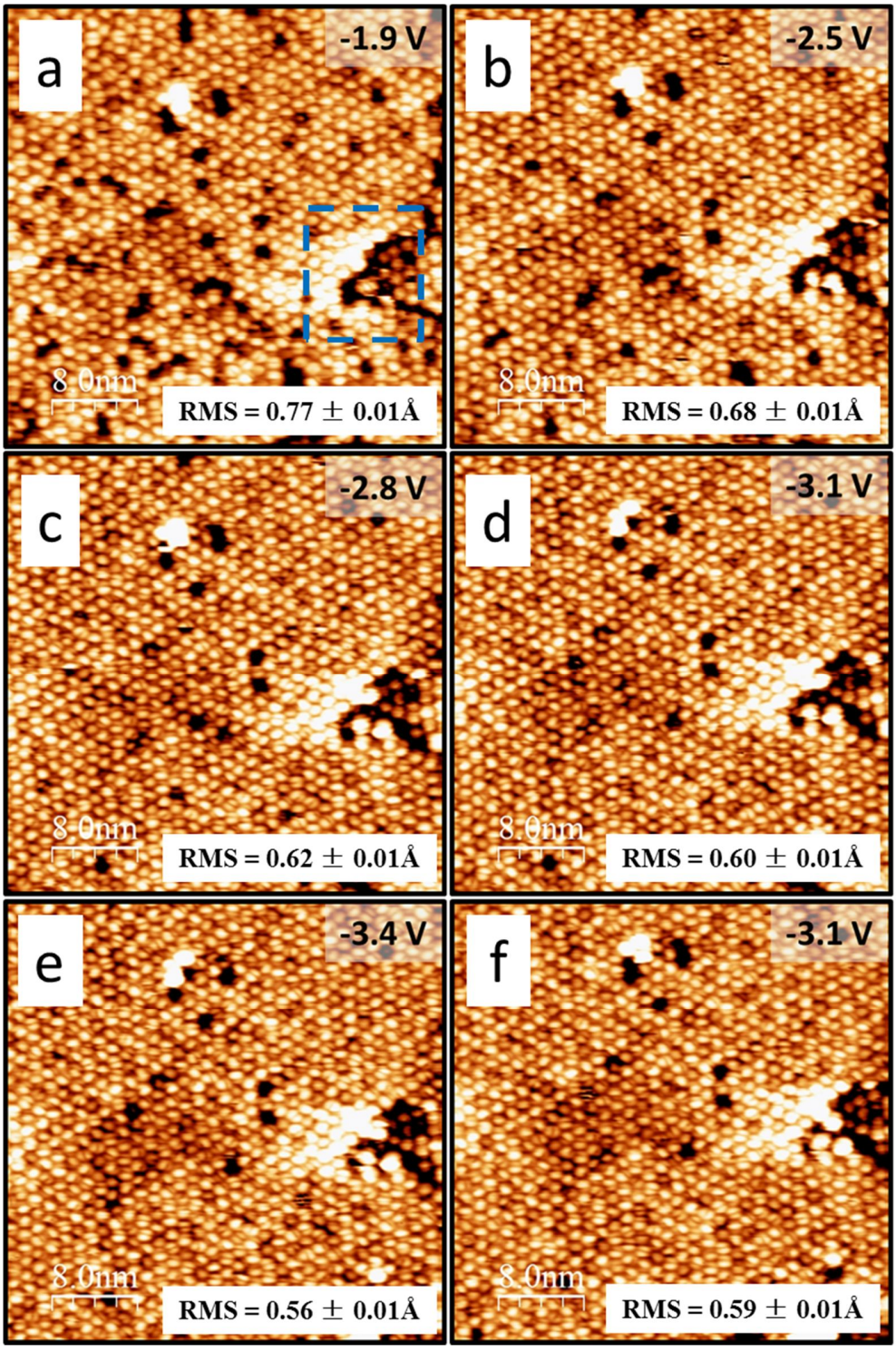

Figure 3.2 Series of STM images taken at different tip voltage bias. Images are in chronological order and are acquired at tunnelling currents of 95pA. Area of reference is indicated by a blue dotted box in a). Tip bias where images are acquired at is indicated. RMS values of respective images are also shown.

To ensure that the contrast is not tip driven, i.e.: physical perturbation of the molecules during scans, we measure the RMS roughness of the image obtained at one particular bias (-3.1V) before (Figure 3.2d) and after (Figure 3.2f) a series of other scans, in particular, Figure 3.2e at -3.4V and another at -1.9V (not shown). Similar RMS roughness is measured for both Figure 3.2d and 3.2f. The only perturbation that we observe between both images is a slight thermal drift as well as a shift in the molecular positions of some isolated molecules placed on the first molecular layer. Though we do not entirely exclude the possibility of a tip-induced molecular perturbation, the reproducibility of the RMS values and topographical features between images of the same bias that were taken at different times (Figure 3d and f) indicates that the observed contrast is most likely of an electronic origin as any tip-induced perturbations would have been random and resulted in substantial deviation of the molecular positions.

Taking into consideration the similarity in molecular appearance and contrast on both HOPG and graphene substrates as well as the bias dependent changes in height differences between molecules, we attribute the observed contrast to the number of fluorine atoms for each molecule. Such variation in fluorine content can be due to degradation over time or even thermal effects during the deposition process. In addition, the purity of the source is only 95%, thus there is a possibility of having $C_{60}F_{x<48}$. The differences in fluorine content would thus alter the electronic structure between each molecule and therefore the amount of tunnelling current under the same scanning conditions. This results in the observed contrast being due to electronic differences of fluorinated fullerenes with varying fluorine numbers and not due to substrate-induced height differences.

3.4 Fluorine intercalation of buffer layer using $C_{60}F_{48}$ molecules

3.4.1 Semi-intercalated graphene nanoribbon array

The intermediate stage of the intercalation process is measured and described in this section. When the substrate with the deposited molecular layers is annealed at 120°C, desorption of molecules from the graphene surface takes place but there are still molecules adsorbed in a non-close packed disordered arrangement on the buffer layer as observed under STM in Figure 3.3a. This is due to the higher adsorption energy of the molecules on the buffer layer. The streaks in the image are due to highly diffusive molecules on graphene which are insufficient in numbers to form stable molecular islands. We observed that there are no significant changes to the pre-existing graphene at all stages of the experiment. The subsurface buffer layer is always observed beneath, indicating no intercalation. This is likely due to the lower adsorption energy of the molecules, which results in molecular desorption at low temperatures prior to intercalation. Another likely reason is that the monolayer graphene acts as an additional barrier to intercalation, preventing intercalation at the interface between the buffer layer and the substrate.

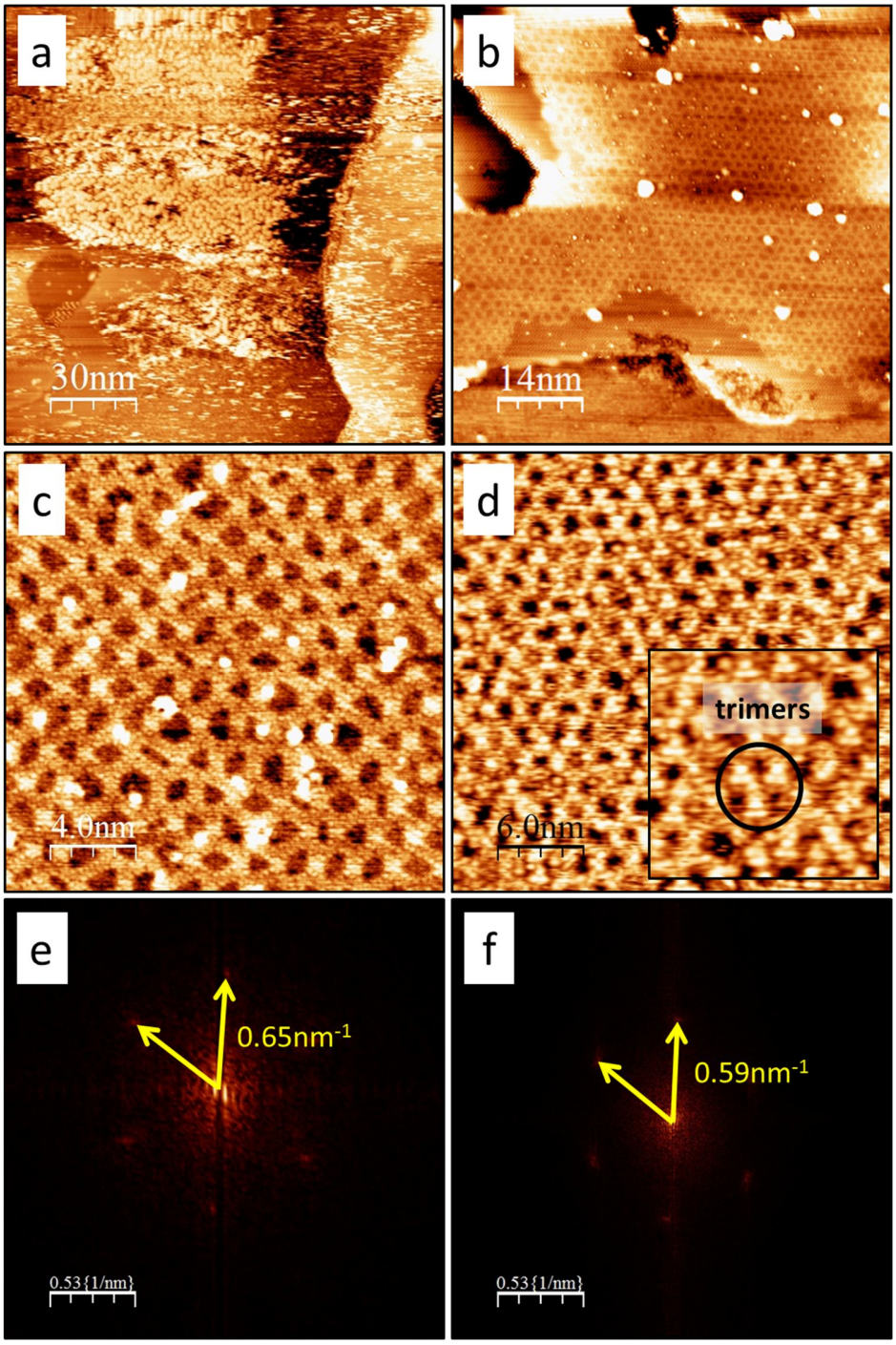

Figure 3.3 a) 150 x 150 nm^2 STM image of remaining $C_{60}F_{48}$ molecules on buffer layer after annealing at 150°C. (V_{tip} = -2.0V, I = 100pA) b) 20 x 20 nm^2 STM image of semi-intercalated graphene. (V_{tip} = -2.0V, I = 100pA) c) High resolution 20 x 20 nm^2 STM image of semi-intercalated graphene. (V_{tip} = 2.0V, I = 100pA) d) 30 x 30 nm^2 STM image of buffer layer. (V_{tip} = 2.0V, I = 100pA) Inset: Zoomed in 11.5 x 11.5 nm^2 STM image showing trimers in the buffer layer. e) FT image of c). f) FT of a 150 x 150 nm^2 STM image of a buffer layer.

Figure 3.3b shows a large scale STM image of the sample surface where the molecules have desorbed after annealing the substrate at 150°C. No molecules remain on either graphene or buffer layer surfaces. At negative tip biases (-2.0V), the buffer layer is displayed as a rough surface without distinct features while the graphene layer is observed as a relatively smooth surface. In addition to these two surfaces which existed before molecular deposition and annealing, there now exists a third type of surface which occupies the bulk of the image and has a rippled appearance made up of quasi-periodic valleys and ridges. We note the difference in appearance between this rippled surface in Figure 3.3c and the pre-existing buffer layer on the substrate as described in Figure 3.3d. The well-defined features (trimers) that we observed for the buffer layer in the inset of Figure 3.3d are not present in the rippled surface. Instead, the rippled surface is made up of a series of polygons (trapezoids, diamonds and hexagons) comprising of valleys and ridges. By performing Fourier Transformation (FT) (Figure 3.3e) of the STM image in Figure 3.3b and taking the inverse of the length of the reciprocal lattice vectors as indicated, we note that the lattice vectors of the rippled surface have a crystallographic direction with a rotation of 30° away from the primary 1 x 1 graphene lattice vectors (compared to Figure 3.4b) and a quasi-periodicity of 1.5 ± 0.1 nm. This is similar, at least within instrument errors, to the FFT (Figure 3.3f) taken of a large scale STM image of the buffer layer (not shown) that has similar (within instrumental errors) lattice vector direction and periodicity of 1.7 ± 0.1 nm. This implies that the observed valley and ridges might have originated from the buffer layer.

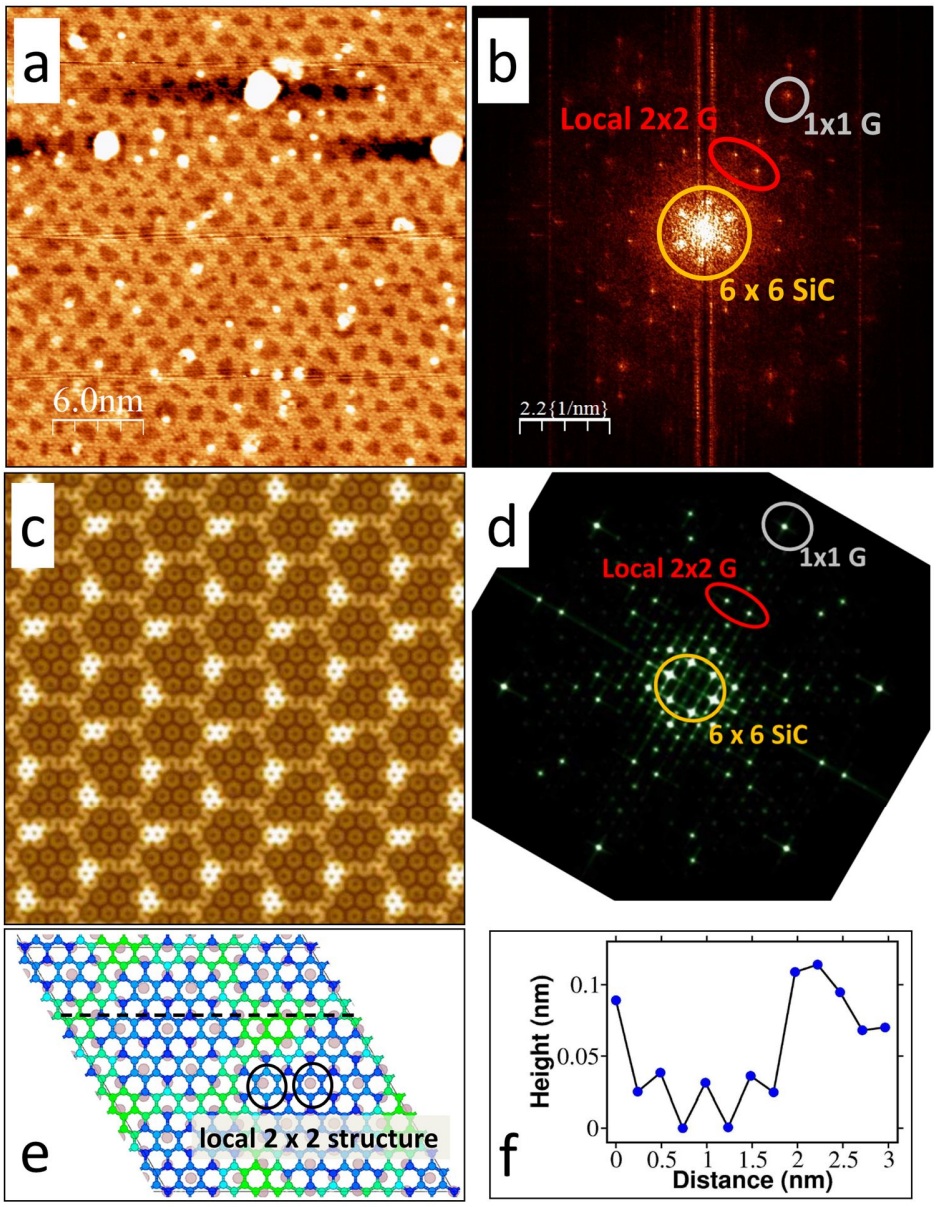

Figure 3.4 a) 30 x 30 nm^2 STM image of rippled surface (V_{tip} = 2.0V, I = 100pA) and its corresponding b) Fourier transformed image. c) *Ab initio* total charge density image of buffer layer on top of the Si-terminated SiC surface. White line indicates the 6 x 6 superlattice imposed by the polygons. d) FFT image of c). Note that the original image has been rotated to align the orientations of the simulated charge density image and our experimental FFT image in b). e) Atomic positions in the buffer layer in the *6R3* cell. Si atoms in the last SiC plane are in grey (larger circles). The colour of the carbon atoms in the buffer layer varies as a function of their height, ranging from blue, close to the substrate, to green for the uppermost atoms. Dark blue carbon atoms are bonded to the Si atoms below. Local 2 x 2 structure is indicated by black circles. f) Height profile of the buffer layer atoms along the line defined in e). Images c) – f) are reproduced with permission from Reference 27. ©2008, American Physical Society.

To further confirm this hypothesis, the structure of this surface is compared against previously reported theoretically simulated charge density images of the buffer layer in Figure 3.4.[27] Figure 3.4a displays the rippled surface and the corresponding FT is shown in Figure 3.4b. The FT of the theoretically simulated charge density image of the buffer layer (Figure 3.4c) reported by Varchon et. al.[27] are also reproduced in Figure 3.4d. The simulated image is based on a single layer of carbon atoms with identical physical structure to graphene being placed on the Si-face of SiC and is shown in Figure 3.4e. We note that the salient features of the FT image for the simulated buffer layer (Figure 3.4d) are also present in that of the rippled surface (Figure 3.4b).

The local 2 x 2 graphene (G) spots in the buffer layer are due to local periodicity formed from the lattice mismatch between the carbon layer and the underlying Si atoms of the substrate (Figure 3.4e).[27] This lattice mismatch results in the carbon atoms present in the overlying layer to bond with the Si atoms that are located directly under them. This leads to the observed local 2 x 2 configuration, i.e., each free benzene ring of the carbon layer is locally separated from each other by two times the graphene unit vector. The bonding also creates a variation in height of the carbon atoms away from the substrate as indicated in Figure 3.4f. The highlighted 6 x 6 SiC spots are due to the quasi-periodicity of the polygons formed in the buffer layer because of the Si-C bonds between the carbon layer and the substrate. We note that the polygons present in the simulated charge density image in Figure 3.4c resemble those observed for the rippled surface in Figure 3.4a. This further corroborates the hypothesis that the periodicity observed in the rippled surface is a direct consequence of its origin from the buffer layer with part of its physical structures retained.

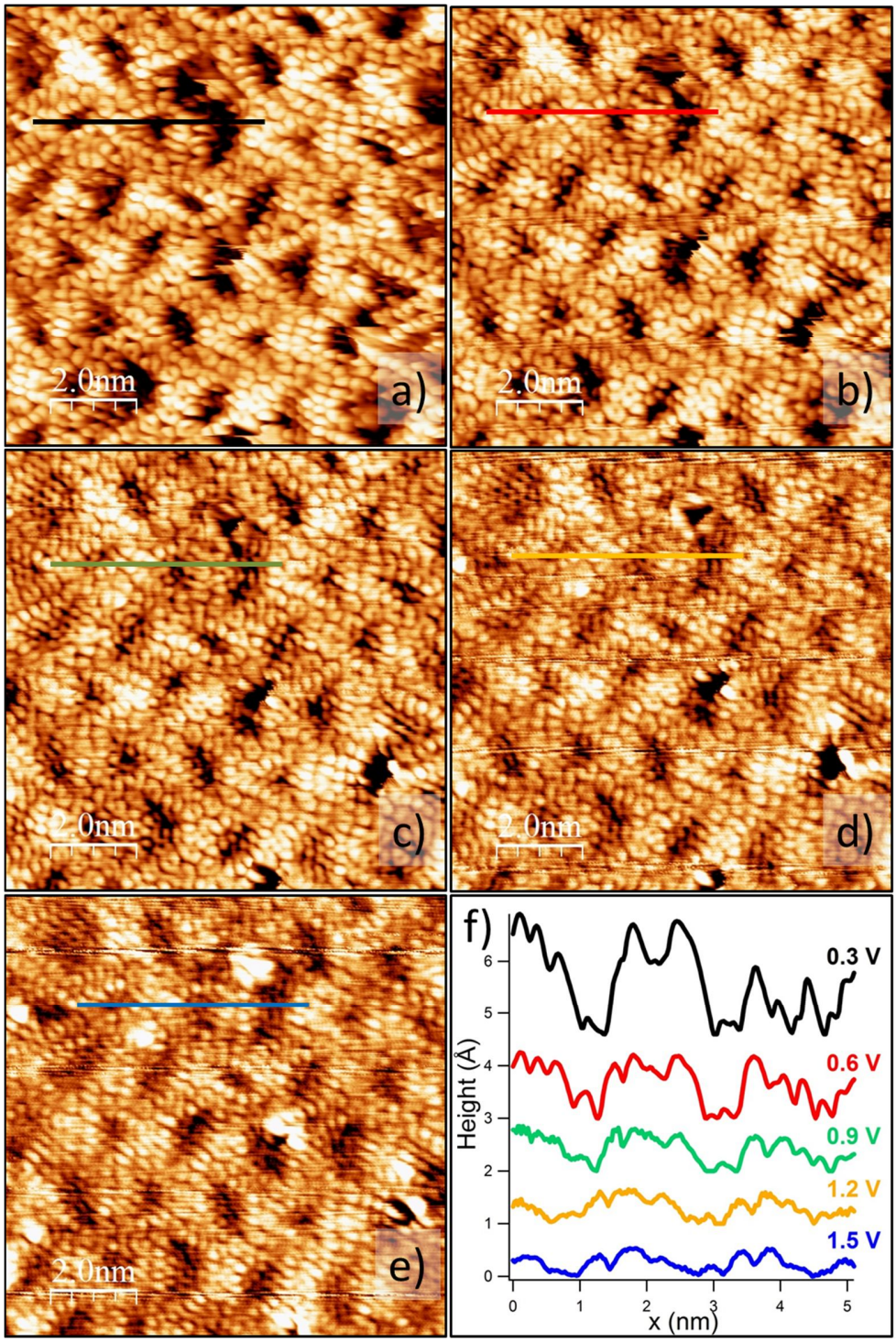

Figure 3.5 Series of 10 x10 nm^2 STM images with I = 90pA and bias of a) 0.3 V, b) 0.5 V, c) 0.7 V, d) 0.9 V and e) 1.5 V. f) Height profiles taken along the indicated green line for each STM image. Maximum peak to valley heights of 2.2Å (0.3V), 1.2Å (0.6V), 0.8Å (0.9V), 0.6Å (1.2V) and 0.5Å (1.5V) are measured. Lines are offset for clarity and bias of associated image is indicated.

A series of STM images of the rippled surface taken at different voltage bias (0.3V, 0.5V, 0.7V, 1.0V, 1.5V) is shown in Figure 3.5. We note that the contrast between the valleys and ridges increases with decreasing bias. The height profiles for each STM image, taking into account thermal drifts, are taken for a series of ridges and valleys and are displayed in Figure 3.5f. The largest difference in height between the ridge and the adjacent valley is measured to be 2.2 ± 0.1Å at a tip bias of 0.3V (Figure 3.5a) and the smallest contrast of 0.5 ± 0.1Å is measured at a tip bias of 1.5V (Figure 3.5e). This implies that the observed ridges and valleys are not purely of topographical origin but rather due to differences in both electronic structure and physical height.

In addition, we can also exclude the possibility of the fluorinated fullerenes being intercalated as their molecular heights of ~ 1nm are much larger than the height differences observed. Based on these observations, we hypothesize that these ridges consist of elevated graphene with fluorine intercalated underneath, while the valleys possess carbon atoms that are still bonded to the substrate. Due to the increased separation of these ridges from the substrate as compared to the conventional buffer layer, they exhibit properties of graphene. The variation in height difference with tip bias is thus attributed to the difference in electronic density of states close to the Fermi level of the ridges and valleys. The valley regions where the carbon atoms are still bonded to the silicon atoms of the underlying substrate would have no electronic states; while the elevated graphene would have electronic states at energies close to the Fermi level. Therefore, at low bias, there would be many electrons tunnelling to or from the tip to the ridges than to the valleys, giving rise to the observed larger height difference. When the tip bias is increased to ±1.5V, there will be an increased density of states from which

electrons tunnel in the valley regions, thereby reducing the apparent height differences. Thus, the rippled surface is termed as semi-intercalated graphene.

These elevated semi-intercalated graphene arrays could be formed due to selective fluorine intercalation in which intercalation takes place first in the regions below the buffer layer possessing Si dangling bonds at low annealing temperatures before spreading to the surrounding regions where C atoms are still bonded to the underlying substrate. Such an intercalation process would result in ridges which coincide with the quasi-periodic lattice parameter of the buffer layer as measured in the FT images in Figure 3.4. Similar observations have been reported by Cranney et. al. for gold intercalated epitaxial graphene on SiC (0001) but are attributed to standing waves formed due to a superlattice induced by the presence of gold nanoclusters between the graphene monolayer and the buffer layer.[28] However, in contrast to their STM results in which a continuous graphene sheet can be imaged above these clusters, we always observe the network of ridges and valleys of the semi-intercalated graphene at any bias. This indicates that in our experiments, the semi-intercalated graphene is formed through fluorine intercalation between the buffer layer and the substrate rather than between the graphene and the buffer layer.

To confirm the structure of the semi-intercalated graphene, the edges (armchair or zigzag) at which the semi-intercalated graphene is bonded have to be identified. As epitaxial graphene on SiC (0001) has the same crystallographic orientation throughout the entire surface,[4,29] its orientation is used as a reference to determine the termination edges of the semi-intercalated graphene in Figure 3.6. In Figure 3.6a, the reference graphene is measured on the same substrate and the direction of the armchair edge is

labelled accordingly. Due to the three fold symmetry of graphene, the angles at which the ridge edges differ from this labelled orientation would determine whether the ridge is terminated at a zigzag (angular difference in multiples of 30°) or armchair edge (0° or angular difference in multiples of 60°). Measuring the angular difference of the ridge edges against the reference direction (representative image in Figure 3.6b), we found that about 89 % of the semi-intercalated graphene are terminated along the zigzag edges. There exists a minority in which the ridge edges are made up of a mixture of armchair and zigzag components. The distances between the edge features in the high resolution STM image of Figure 3.6c is measured to be 0.51 ± 0.01nm, which is approximately equal to 2a, where a = 0.246nm is the graphene unit cell length. This is possible only if it is measured along the graphene zigzag edge as shown in Figure 3.6d.

Comparing our observations with the simulated charge density image of the buffer layer (Figure 3.4c), we note that the carbon atoms which are not bonded to the underlying silicon atoms are situated along the zigzag edges. The distance between the observed “semi-hexagons” at the edges also corresponds to a length of 2a. Hence, we hypothesize that the semi-intercalated graphene is made up of a graphene sheet that is bonded to the underlying substrate Si atoms with a quasi-periodicity of 1.5nm, similar to that of the buffer layer. At the same time, the Si dangling bonds that are present beneath the carbon layer are passivated by fluorine intercalation. This results in the carbon atoms in the intercalation region being sufficiently elevated from the substrate and possessing graphenic properties. The areas where there is a mixture of armchair of zigzag edges are due to additional breaking of the Si-C bonds present in the original buffer layer during the initial intercalation and annealing of the substrate.

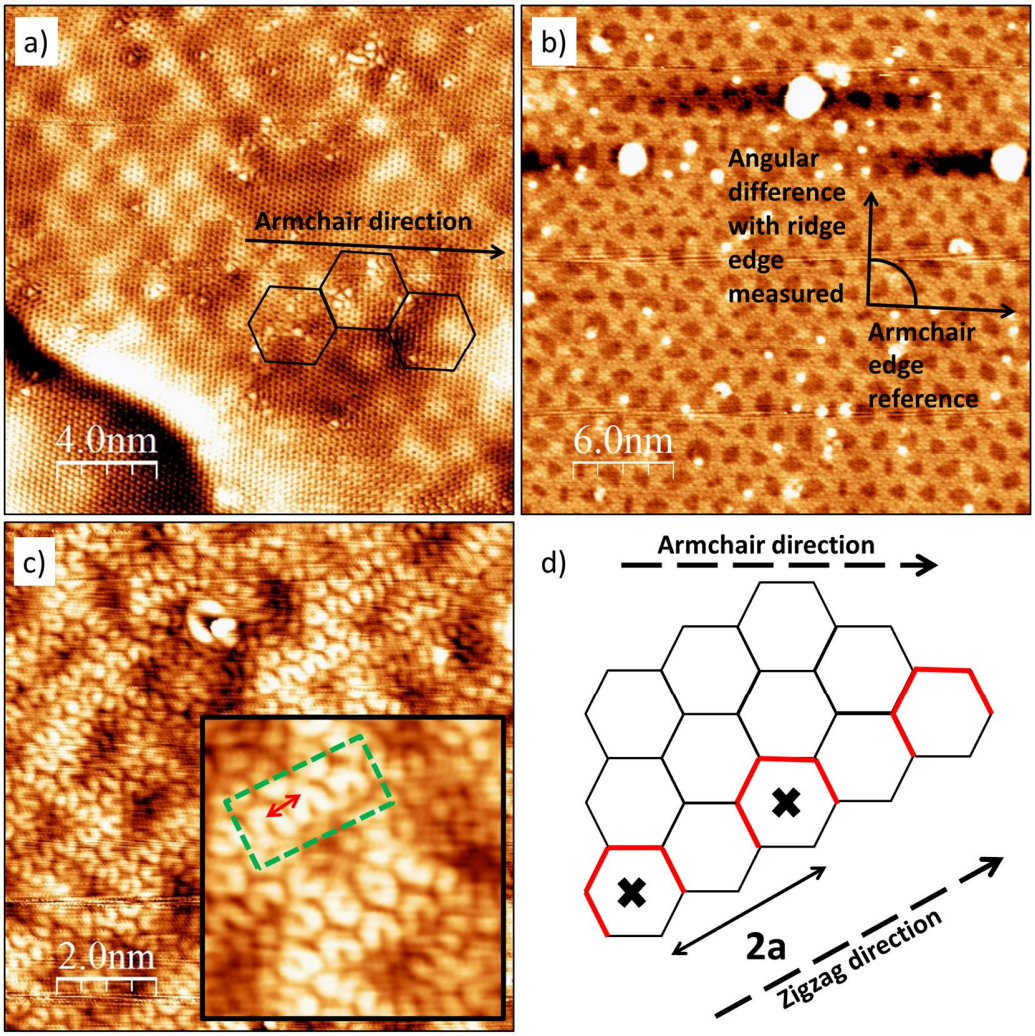

Figure 3.6 a) 20 x 20 nm^2 STM image of epitaxial monolayer graphene (V_{tip} = 0.4V, I = 100pA) with armchair direction labelled. b) 30 x 30 nm^2 STM image of semi-intercalated graphene used to determine orientation of ridge edges. (V_{tip} = 2.0V, I = 100pA. c) 10 x 10 nm^2 STM image of semi-intercalated graphene showing edge features. (V_{tip} = -1.0V, I = 150pA) Inset: Zoomed in 3.4 x 3.4 nm^2 STM image highlighting edge features (in green dotted box). Arrow indicates 0.51nm distance between features. d) Model of zigzag graphene edge with edge features observed in Figure d labelled as red outlines and crosses, indicating the centre of the features.

To differentiate the electronic structure of these ridges from the buffer layer, STS of these structures are performed in Figure 3.7. A lock-in voltage modulation of 600 Hz and 6 mV amplitude is applied to achieve the conductance measurement. A characteristic

spectrum of the buffer layer is presented in Figure 3.7b, with a band gap of 400 ± 10 meV about the Fermi level. We note that the band gap is located asymmetrically about the Fermi level with the centre of the gap at 0.1eV below the Fermi level. This is expected as the semiconducting buffer layer is electron doped by the presence of the dangling Si bonds beneath it.[4,29]

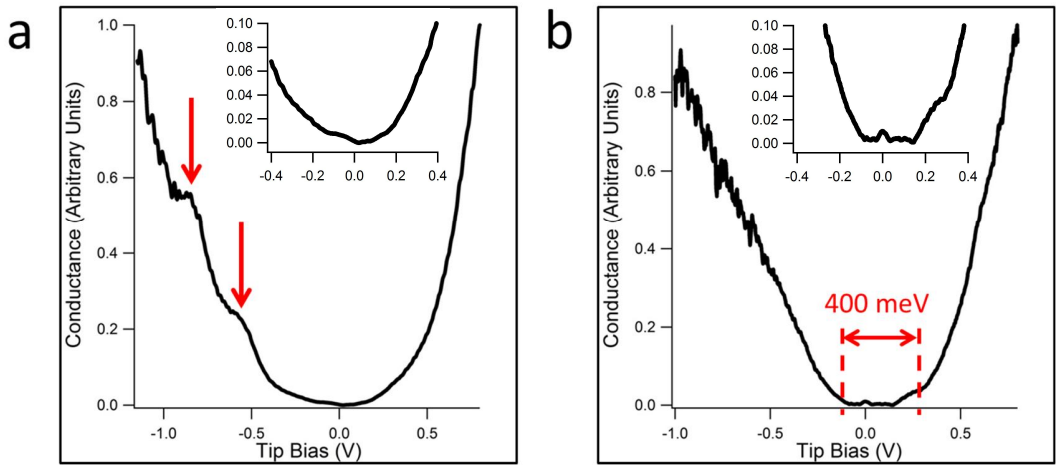

Figure 3.7 a) Averaged STS spectra of semi-intercalated graphene, taken with initial bias of -0.50V and tunnelling current of 100pA. Red arrows indicate location of conductance peaks. b) Averaged STS spectra of buffer layer, taken with initial bias of -0.30V and tunnelling current of 50pA. Absence of conductance about the Fermi level is indicated by the red dotted lines. Insets show zoomed in region of the conductance about the Fermi level for each spectra.

Figure 3.7a displays the averaged STS spectrum randomly measured from different areas of the semi-intercalated graphene. An average is taken as there was no observable difference between STS taken from the valleys and ridges of the semi-intercalated graphene. This is due to the finite size of the tip that makes it difficult to obtain separate tunnelling conductance characteristics from regions a few atoms from each other, (typical valley-ridge separation lengths are < 5Å). One major difference between the spectra taken for the semi-intercalated graphene and that of the buffer layer

is the absence of a band gap about the Fermi level. This is clearly shown in the insets of Figure 3.7 where we note the lack of conductance about the Fermi level for the buffer layer as compared to that of the semi-intercalated graphene. In its place is a local minimum that is present due to the presence of a phonon assisted inelastic tunnelling conductance phenomena as described in Chapter 2.[30] a suppression of electron tunnelling to the tip at low energies due to the short decay length of the electron wave.[30] This is because the decay length is inversely proportional to the large in plane crystal momentum ($k \approx 1.7\text{Å}^{-1}$) of the graphene low energy electronic states involved in the tunnelling process. Thus, tunnelling can only occur via virtual excitations with the assistance of phonons to electronic states near the Γ point with $k \approx 0\text{Å}^{-1}$ which has a much longer decay length. As the phonon requires a certain energy to be activated for tunnelling to occur, the conductance spectra is zero at the Fermi level while it begins to increase from zero once the tip bias applied satisfies the phonon activation energy required.

The spectrum, unlike those of monolayer epitaxial graphene[8,31-33], does not have a Dirac point at 0.5eV below the Fermi level, which would have been characterized by a decrease in LDOS and a corresponding conductance dip at a bias of the same value. Instead, the electronic structure of this new surface differs from those of epitaxial graphene and buffer layer. In addition to a minimum at the Fermi level, there are two conductance peaks at 850 ± 10meV and 570 ± 10meV, flanking a minimum at 710 ± 10meV above the Fermi level. Similar conductance peaks have been reported for bilayer epitaxial graphene on SiC (0001) in which an asymmetric doping level between the topmost and the bottom layer results in a small band gap and observation of two conductance peaks under STS.[34] The two conductance peaks occur due to a saddle point

at which the density of states is a maximum. These saddle points are formed at the conduction band minima and valence band maxima when a band gap is open in the electronic band structure.

Thus, the two conductance peaks observed for the semi-intercalated graphene are attributed to the enhanced density of states at the conductance band minima and valence band maxima when a band gap is formed. Broadening of the peaks is due to thermal effects as well as system resolution. The energy difference between the peaks approximates a band gap of about 280 ± 10 meV at the Dirac point. We hypothesize that the band gap observed is due to the quantum confinement produced by the quasi-periodic bonding of the carbon sheet to the silicon atoms beneath where the valleys of the semi-intercalated graphene are located. This is similar to the reports of Balog et. al., in which a patterned adsorption of hydrogen determined by the moiré features of graphene grown on Ir (111) generates a band gap of at least 450meV in graphene due to quantum confinement of the electrons in the graphene.[35]

A clear local minima indicative of the Dirac point is not observed between the two conductance peaks. This is likely due to contribution from electrons tunnelling from the underlying substrate. Note that we are unable to subtract an appropriate background conductance to remove this contribution as we cannot perform STS on the underlying interface region beneath the semi-intercalated graphene nor locate a similar surface to do so. Hence, we approximate its location to be at the middle of the two peaks, namely at 710 ± 10 meV. This represents a highly doped graphene, which is expected as the intercalation involves bonding of the underlying silicon with fluorine which is highly electron withdrawing. Additional theoretical calculations would be required to fully

justify these observations. Based on these observations, a model describing the physical structure of the semi-intercalated graphene is proposed in Figure 3.8.

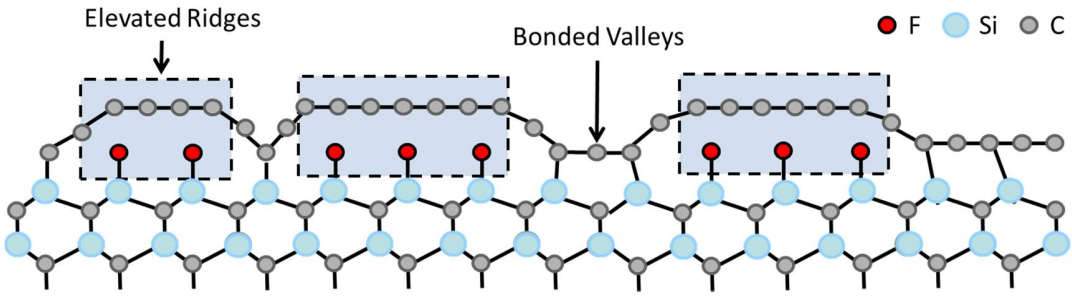

Figure 3.8 Schematic side view of semi-intercalated graphene, highlighted regions indicate regions of fluorine intercalation.

The semi-intercalated graphene, similar to the buffer layer, is still partially bonded to the silicon atoms of the substrate with similar periodicity of 1.5nm. The silicon-carbon bonds occur along the zigzag edges of the carbon sheet. The presence of the Si-C bonds in regions where the carbon atoms are directly above the silicon atoms (Figure 3.4c) is reflected in the observed local 2 x 2 configuration of the FT image (Figure 3.4b). However, unlike the buffer layer which has silicon dangling bonds beneath the carbon layer, these bonds under the semi-intercalated graphene are passivated due to the formation of Si-F bonds during the intercalation process. Thus, the carbon atoms above these Si-F bonds are elevated to a larger separation from the substrate as compared to those in the buffer layer. This increase in height results in a reduced interaction with the substrate and hence the carbon layer above the fluorine passivated regions display electronic properties of graphene as shown in the STS measurements. STS measurements have also verified that the superlattice structure formed due to the periodic bonding of the

carbon atoms of the elevated ridge-like graphene to the underlying substrate creates a band gap in the electronic band structure of the semi-intercalated graphene.

3.4.2 Fully intercalated quasi-freestanding monolayer graphene

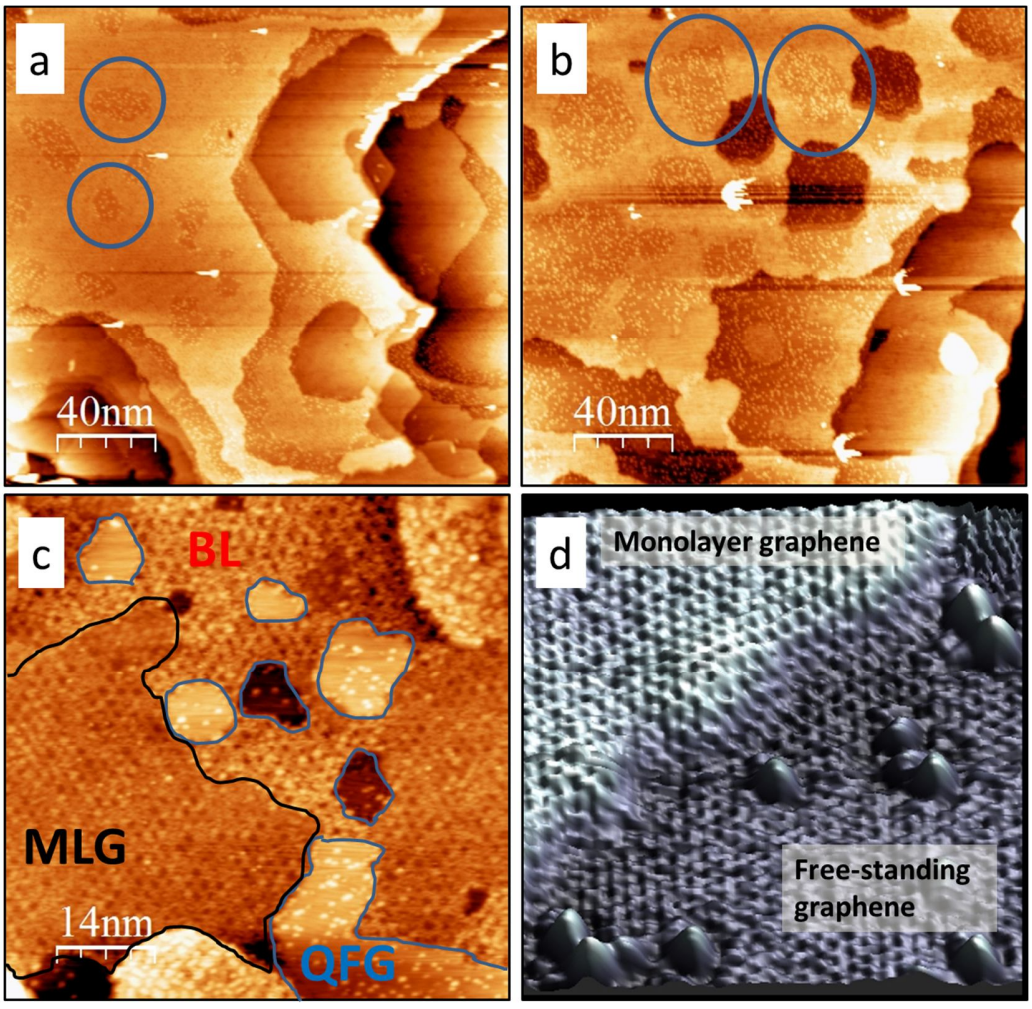

Figure 3.9 a) 200 x 190 nm^2 STM images of surface after applying procedures once and b) after applying procedure 4 times (Both images V_{tip} = -2.0V, I = 100pA). Some of the intercalated areas are circled in blue as a guide to the eye. c) 60 x 60 nm^2 STM image of a region consisting of three different types of surface. Quasi-freestanding graphene (QFG) is labelled and outlined in blue, buffer layer (BL) is indicated in red and pre-existing epitaxial monolayer graphene (MLG) is labelled and outlined in black (V_{tip} = 2.0V, I = 100pA). d) 3D topographical rendering of a 8 x 8 nm^2 STM image taken at the continuous boundary between pre-existing monolayer epitaxial graphene and quasi-freestanding graphene produced by fluorine intercalation (V_{tip} = -0.1V, I = 75pA).

When the sample is further annealed to 900°C, the intercalation process is complete and the surface produced is shown in Figure 3.9. Figure 3.9a and b are the STM images of the substrate surface after the deposition and annealing cycle was performed once and four times respectively. In the regions outlined with blue circles (Figures 3.9a and 3.9b), the underlying buffer layer was no longer observed under STM (as indicated in Figure 3.9c). The STM image in Figure 3.9c shows that unlike the pre-existing monolayer epitaxial graphene or semi-intercalated graphene, the $6\sqrt{3} \times 6\sqrt{3}R30°$ reconstruction of the interfacial buffer layer under the fully intercalated graphene cannot be observed regardless of bias applied. At low bias, the honeycomb structure of the graphene layer is clearly resolved (Figure 3.9d). This implies the absence of an interfacial buffer layer underneath a single layer of graphene after intercalation. Thus, in accordance to other similar studies, the term quasi-freestanding graphene is coined for surfaces in which the interaction with the substrate through the interfacial buffer layer is essentially removed.[15] In addition, semi-intercalated graphene is no longer observed and we attribute the semi-intercalated graphene to be an intermediate state prior to the formation of quasi-freestanding graphene.

From the observed coverage of this intercalated surface in the large scale STM image of Figures 3.9a and b, we note that complete intercalation is not achievable within a single cycle. The intercalated area can be increased after subsequent dose/anneal cycles. By calculating the decoupled graphene: buffer layer area ratio over STM images covering a total area of about 80 000 nm^2, the ratio is estimated to increase from 0.69 (after one cycle) (representative image in Figure 3.9a) to 1.87 after repeating the procedure thrice more (representative image in Figure 3.9b). We also note that the size of the final

intercalated surface is limited only by the size of the terrace that it resides on, similar to the intermediate stage as described in the previous section. The random locations of the surface where intercalation occurs as well as the requirement of repeated dose/anneal cycles are likely due to competing fluorine dissociation and desorption processes. This also implies that the intercalation process could have taken place in areas with lower barrier of entry to the fluorine molecules such as those at the step edges as well as pre-existing defects on the surface as observed by Bao et. al. using real time LEEM and PEEM studies which showed that Pb intercalation of graphene on Ru (0001) surface begins at the open edges of the graphene islands.[36] Similar to the intermediate stage, neither conversion of the pre-existing graphene monolayer into bilayer graphene nor modification of the monolayer graphene was observed. This was verified by repeating the same procedure on monolayer epitaxial graphene on SiC (0001) to no observable effect. This may be related to the weaker intercalation at a lower temperature of 150°C that results in fluorine penetrating a single buffer layer. In contrast, methods which involve direct application of H_2 and Li intercalants at elevated temperatures allow intercalation beyond the first graphene layer.[14-16]

This intercalated quasi-freestanding surface is also continuously connected to the surrounding pre-existing non-intercalated epitaxial graphene. A three dimensional topographical derivate of an STM image taken over one such boundary is shown in Figure 3.9d. The graphene layer is observed to flow continuously between the two regions without any electron scattering at the boundary, indicating that the boundaries between the non-intercalated and intercalated graphene are defect free. The protrusions observed are nanostructures present on the intercalated graphene and will be explained in

the following paragraphs. The intercalated surface is stable under ambient conditions and persists even after annealing at 1100°C higher than that of other intercalated products.[14-16] The experiments described in this report were repeated and carried out over a period of 5 months with no significant change in the measurements. The highly stable nature of the quasi-freestanding graphene is attributed to the strong Si-F bonds formed at the interface. In addition, if the sample is annealed directly to 900°C, there is no observed intercalation. At a higher temperature, the molecules desorb before sufficient fluorine migration to the interface occurs.

Apart from the absence of the underlying buffer layer, additional features due to the intercalation process are also observed and described in Figure 3.10a and c. Figure 3.10c depicts a high resolution STM image of these features. These features consist of circular protrusions with no distinct structure (indicated by a black box) and diffusive bright spots above which the honeycomb structures are still observed (indicated by a white box). The height of the protrusions is measured to be 0.04 ± 0.05 nm, much shorter than typical bond lengths ≥ 0.1nm. This precludes its origin from intercalated $C_{60}F_{48}$ molecules or associated molecular fragments left below the graphene layer. Furthermore, the areas surrounding the protrusions do not show any electron scattering patterns that have been observed around atomic vacancies or point defects of graphene.[37,38] Thus, we propose that these protrusions are due to isolated fluorine atoms bonded to the decoupled graphene. As their heights are only 0.04nm, much shorter than typical C-F bond lengths which are greater than 0.1nm, these fluorine atoms are likely to be located beneath the graphene layer. This will be further corroborated later by the observed electronic structural changes. The diffusive bright spots with heights < 0.1 nm are attributed to the

undulations of the graphene layer. STS measurements show no difference compared to those of quasi free-standing graphene.

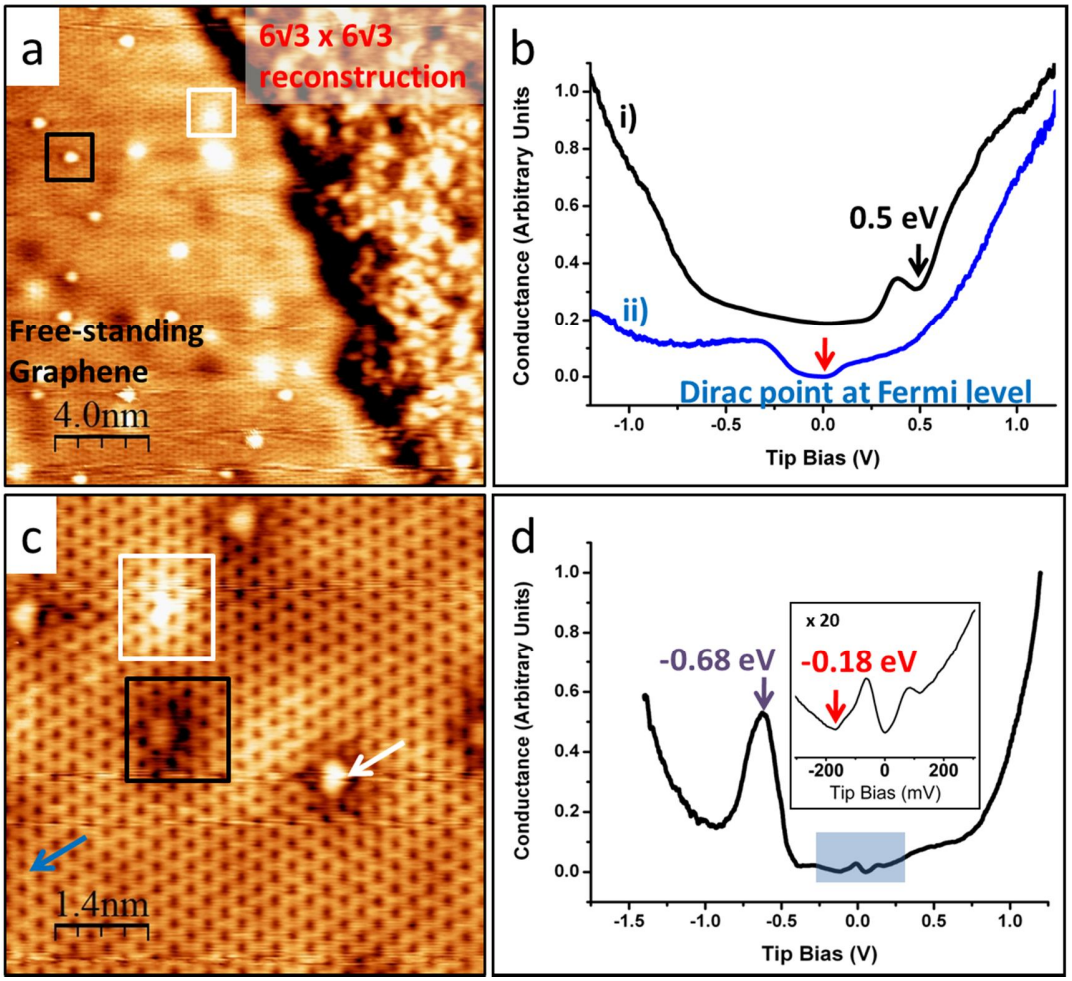

Figure 3.10 a) 20 x 20 nm^2 STM image showing intercalation induced quasi-free-standing graphene monolayer joined continuously with pre-existing graphene monolayer. (V_{tip} = -0.35V, I = 100pA) b) Averaged dI/dV spectra taken on i) pre-existing graphene and ii) on decoupled graphene at points away from protrusion, an example indicated by a blue arrow in c). c) 7 x 7 nm^2 STM image of surface, (V_{tip} = -0.25V, I = 100pA). d) dI/dV spectra taken over protrusions on decoupled graphene, as indicated by a white arrow. b) and d) Red arrows indicate position of Dirac point and purple arrow indicates position of resonance peak.

To ascertain any changes in the electronic band structure between quasi-freestanding and non-intercalated graphene, STS measurements were carried on each

surface respectively and are shown in Figure 3.10b. The STS measurements on quasi-freestanding graphene were taken sufficiently far away from any nanostructures to exclude any influence of their electronic perturbation. In Figure 3.10b, the characteristic spectrum (Spectrum i) with a minimum at Fermi level and a secondary minimum indicating the Dirac point at 0.50 ± 0.01eV below the Fermi level is observed for the pre-existing monolayer epitaxial graphene, due to electron doping from the buffer layer.[8,31-33] The first minimum is due to the suppression of tunnelling electrons to and from graphene as discussed earlier. The second minimum occurs due to the reduction in electronic density of states. As the DOS for graphene reduces linearly with energy, the DOS at the Dirac point should be zero. However, due to electrons tunnelling from the underlying substrate, there is still conductance picked up at the bias energy (0.5V) where the Dirac point is located. Thus, this is reflected by a second local minimum in Figure 3.10b. In contrast, there is no significant minimum besides the one at the Fermi level detected for the quasi free-standing graphene.

Hence within resolution limits and applying the same argument, the Dirac point of the free-standing graphene is taken to be at the Fermi level, i.e., the free-standing graphene is charge neutral. This indicates that the removal of the interfacial buffer layer results in a charge neutral surface. This is expected as the buffer layer has been reported to be the main contributor to the doping effect in graphene on SiC (0001). Such an observation is in contrast to the p-type doping (Dirac point 0.6eV above Fermi level) measured for the intermediate stage of semi-intercalated graphene. The difference in doping level could be due to the desorption of fluorine at the interface when annealed to 900°C. The continuity of this surface with the surrounding electron doped as-grown

epitaxial monolayer graphene could also contribute to the reduced p-type doping after intercalation.

Figure 3.10d shows the STS performed on the protrusions of the quasi-free-standing graphene. In addition to the expected STS of a graphene monolayer, there is a resonance peak located 600meV above the Fermi level in the conduction band. Furthermore, STS measurements performed away from the centre of the protrusion indicate an almost instant decay of this resonance peak beyond the edge of the protrusion, indicating a highly localized potential perturbation that a strongly adsorbed adatom would provide. Theoretical calculations by Pereira et. al. have shown that such a peak can be induced by a highly localized impurity on graphene causing a perturbation in the onsite potential energy at its location.[39] The location of the peak in the conduction band indicates that this impurity has an attractive potential. This impurity also induces a slight p doping of the graphene at its location as the Dirac point (inset of Figure 3.10d) is now observed to be at 175meV above the Fermi level. This is expected as an attractive impurity potential would draw electrons away from the regions of graphene in its vicinity.

We also note that the appearance of these round protrusions is different from those found in a recent report by Hong et. al. in which the points on the surface where fluorine is covalently bonded to are observed under STM to have a strong three-fold electronic scattering pattern around them.[40] Rather, the appearance of the protrusions in our STM measurements is similar to a study on graphite where a portion of the fluorine atoms was ionically bonded to the graphite surface without causing any significant electronic scattering.[41] This implies that in our experiments, fluorine atoms are also ionically bonded to the graphene layer from below, thus not completely disrupting the π

dispersion bands which would have caused observable electronic scattering. Thus, these STS measurements corroborate our hypothesis that the protrusions are due to electronegative fluorine atoms being bonded to the decoupled graphene from below. Hence, they exert a localized attractive impurity potential that causes the observed electronic structural changes. Deviations with theoretical calculations in terms of peak position is expected as the model used does not take into account the change from sp^2 to sp^3 hybridization of the C-C bonds after fluorine adsorption.

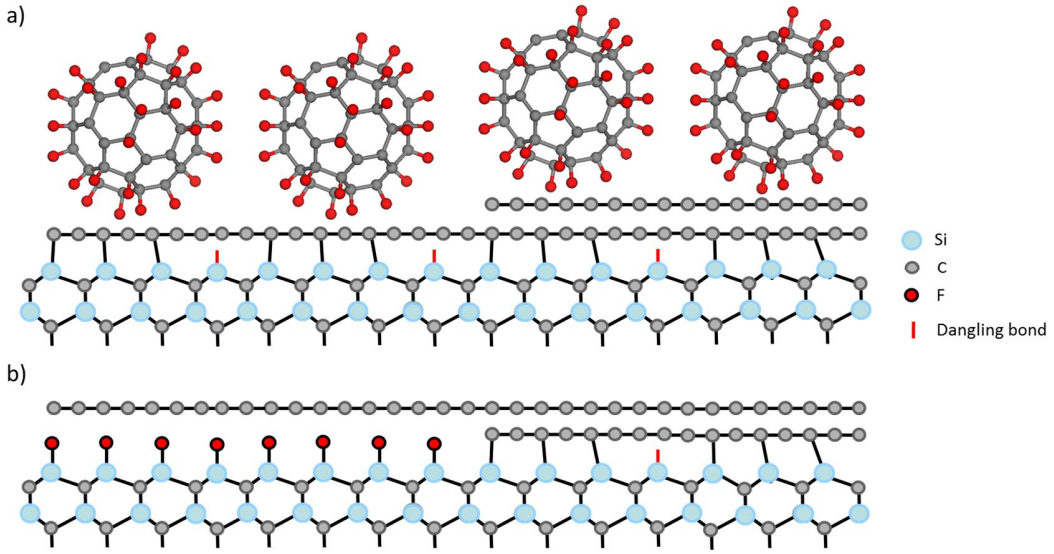

Figure 3.11 Schematic model describing a) $C_{60}F_{48}$ molecules deposited on a surface having both monolayer graphene and buffer layer and b) continuous surface of quasi-free-standing graphene monolayer and non-intercalated monolayer graphene after annealing at temperatures of 150°C and 850°C.

A model of the intercalation process is summarized in Figure 3.11. Fluorine penetrate only the buffer layer from the step edges or defects and break the Si-C bonds holding the buffer layer to the substrate. In the process, Si-F bonds are formed in place and the buffer layer, no longer covalently bonded to the substrate, now has graphenic

properties with the interface being terminated by Si-F elements. The intercalated graphene then forms a continuous surface with the surrounding pre-existing epitaxial graphene left untouched by the intercalation. Therefore, the produced graphene no longer has an interfacial buffer layer as observed under STM.

3.4.3 PES Measurements of Quasi-Freestanding Graphene

As the STM can only accurately probe the topmost layer, we employ PES measurements to investigate the new interface layer after intercalation. The as-produced sample was transferred to a different UHV chamber for measurements using synchrotron PES. In-situ annealing to 800°C was performed to remove possible surface contamination and the cleanliness was checked using PES to confirm the absence of atmospheric contaminants (H_2O and O_2) in the O 1s core level peaks. The integrity of the structure was maintained even after transport through ambient conditions and is confirmed by measuring it under LT-STM again after PES studies. For comparison, a reference graphene sample is included in the measurements to compare changes observed between intercalated and non-intercalated samples.

The results of the PES measurements are shown in Figure 3.12. Si 2p and C 1s spectra were measured for the fluorine intercalated product and also for a monolayer epitaxial graphene on SiC (0001), for comparison. The presence of fluorine is verified through the F 1s signal at binding energy of 686.7 ± 0.1eV, as measured for the fluorine intercalated sample in Figure 3.12e. The relative depth of various species in the substrates is differentiated by changing the angle of electron emission detected and hence surface sensitivity. Figure 3.12a and 3.12b show the Si 2p spectra for fluorine intercalated and monolayer epitaxial graphene respectively. The Si 2p peaks are made up of spin-orbit

split doublets and the binding energies are calibrated to the Si $2p_{3/2}$ position. Asymmetrical doublets are observed due to the difference in electron population of the $2p_{3/2}$ and $2p_{1/2}$ spin-orbit peaks. Both spectra consist of a dominant Si 2p peak at 101.4 ± 0.1eV due to the bulk SiC component and a shoulder at 100.7 ± 0.1eV is attributed to to another bulk component present in the $6\sqrt{3} \times 6\sqrt{3}R30°$ area of the SiC(0001) substrate as described by others.[42] The smaller satellite peaks are due to defects such as silicon vacancies present in the sample. The difference between that measured for the reference and the intercalated sample is the width in the Si 2p peaks. By performing fitting of the Si 2p doublets for the measured peaks, we discover that an additional Si 2p related doublet is required to fully account for the peak shape of the intercalated sample.

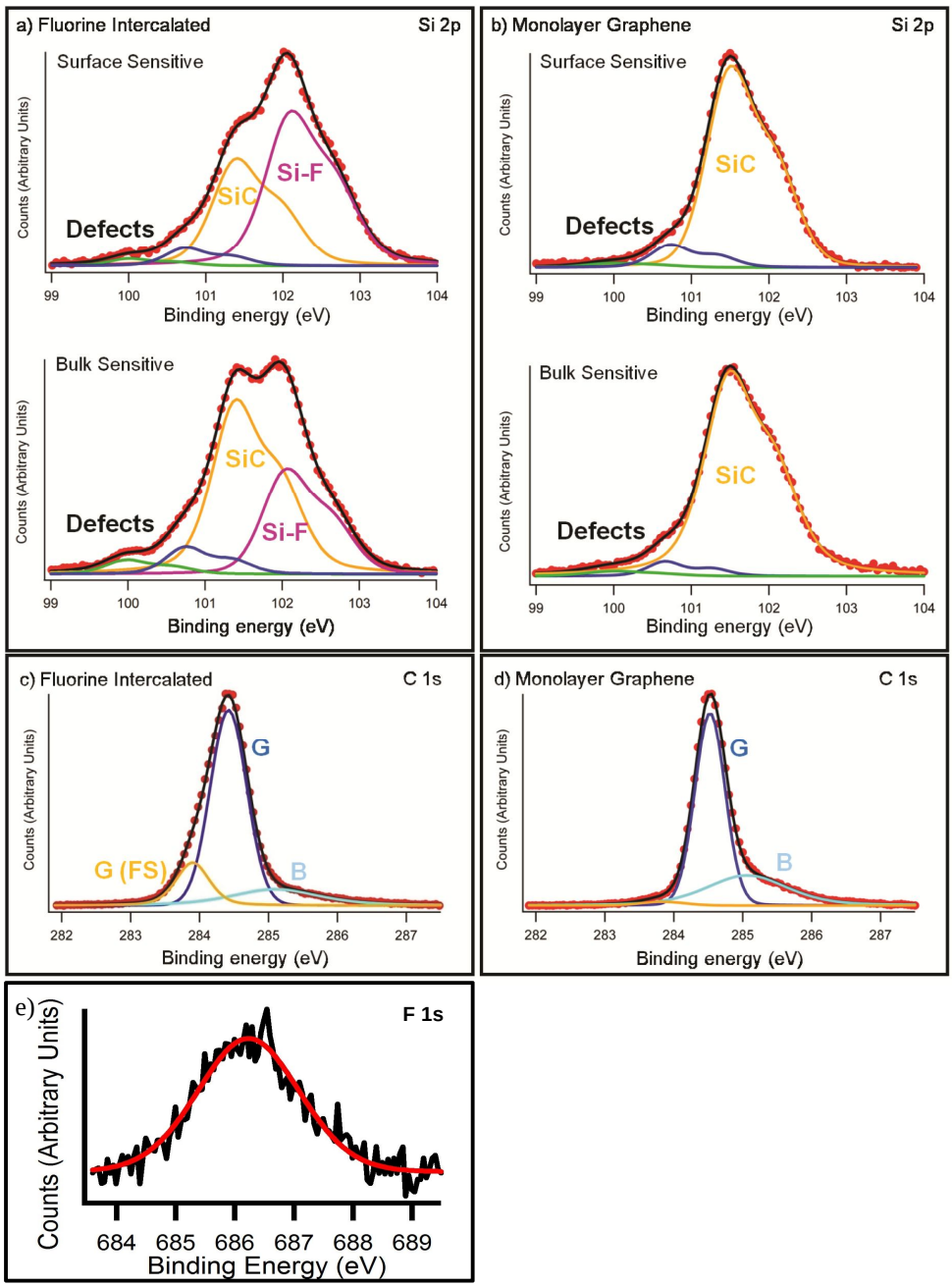

Figure 3.12 Si 2p core level spectra for a) fluorine intercalated graphene sample and b) monolayer graphene. The spectra in the top panel is collected with the beam entering at normal incidence (surface sensitive) while the spectra in the bottom panel is collected with the detector placed at an angle of normal emission (bulk sensitive). Photon energy =140eV for the Si 2p spectra. C 1s core level spectra for c) fluorine intercalated graphene sample and d) monolayer graphene. Photon energy = 350eV with the detector placed at normal emission angles for C 1s spectra. Experimental data are displayed in red dots. The black solid line is the envelope of the fitted components. e) F1s core level spectra taken with photon energy of 750eV at surface sensitive angle.

The additional Si 2p doublet is located at a higher binding energy of 102.1 ± 0.1eV. A higher binding energy indicates that the Si species are bonded to an electron withdrawing element, which in our case is fluorine. This indicates fluorine intercalation did successfully take place and has bonded with the underlying silicon. By decreasing the angle at which electrons are detected with respect to the surface normal, the probing depth is increased and the PES measurements taken are shown in the bottom panels of Figures 3.12a and b. The bottom panel of Figure 3.12a shows the photoelectron signal taken along the surface normal which results in a lower surface sensitivity. We note that the signal of the bulk associated Si 2p doublet increases in intensity while that of the Si-F related interfacial layer has decreased as compared to the surface sensitive measurements (taken at 50° away from surface normal) in the top panel of Figure 3.12a. Such an observation implies that the Si-F related peak is located closer to the surface than bulk SiC, i.e. just beneath the graphene layer. This further corroborates our model that an interfacial Si-F layer has formed in the intercalation process and has replaced the buffer layer. There is no observable shift in the bulk SiC component as compared to that of the reference sample, indicating that the band bending induced by the formation of surface Si-F bonds is similar to that of the Si-C bonds in the buffer layer.[29]

The C1s core levels are then measured to probe the electronic differences in the intercalated graphene. Figures 3.12c and d describe the C1s core level spectra taken using photon energies of 350eV at normal electron emission for both intercalated and reference samples. For both spectra, the highest peak at 284.4 ± 0.1eV belongs to that of graphene with an existing underlying buffer layer while the shoulder situated at a higher binding energy of 285.1 ± 0.1eV belongs to the buffer layer.[6,29] The difference between spectra is

the appearance of a component, labelled G(FS) in Figure 3.12c, at a lower binding energy of 238.9 ± 0.1eV in the C1s spectrum of the intercalated sample. This is attributed to the quasi-free-standing graphene and the difference of 0.5 eV between the two components agrees perfectly with the difference in Dirac point positions between the pre-existing and quasi free-standing graphene observed from STS measurements in Figure 3.10b. Due to the small amount of C-F bonds present (< 0.01%) as indicated by the dilute distribution of protrusions in the STM images, they are not detected in the C1s core level PES. The PES measurements hence confirm that fluorine intercalation was successful and corroborated our model of a charge neutral intercalated quasi free-standing graphene with a fluorine terminated Si-F interface.

3.5 Conclusion and Outlook

In this chapter, we have observed the properties of as deposited $C_{60}F_{48}$ molecules on epitaxial graphene on SiC (0001). The molecules are closely packed and have a layer by layer growth mode. Height variations observed between individual molecules are attributed to the varying fluorine content of the molecules and are verified through deposition on a reference HOPG substrate as well as bias dependent STM images. We have also successfully performed fluorine intercalation using the molecules as a source of fluorine and two different states of intercalation are observed at different annealing temperatures.

A low annealing temperature of 150°C results in a highly p-doped semi-intercalated graphene that is formed due to the initial fluorine bond formation with the underlying dangling silicon bonds. The remaining carbon atoms that are still bonded to the Si atoms below create periodic perturbations of the graphene lattice that induce an

electronic band gap of about 280 meV in the graphene layer. Such a semi-intercalation process provides a bottom up approach of producing graphene with periodic lattice perturbations to produce a desired band gap. In addition, compared to the process of lithographically producing graphene nanoribbons[43,44] to achieve a band gap, our method offers an opportunity of achieving a similar effect in graphene without resorting to top down techniques that may otherwise damage and create defects in graphene.[45,46] The size of these arrays is only limited by the size of the buffer layer terraces. Thus, if a complete surface of these arrays can be produced, it would be of interest to fabricate electronic devices on such a graphene array to study the influence that the confinement induced gap has on the electronic transport through it. Recent graphene nanohole arrays[47-50] fabricated using top down approaches have yielded on off ratios of up to 22 at room temperatures but the arrays (~5 nm to 75nm) are still much larger than the observed sub nm dimensions of our graphene ridges. An advantage that this method has over similar band gap opening produced by patterned adsorption of atoms is that the additional surface functionalization of semi-intercalated graphene may be performed. In addition, the elevated graphene ridges of the semi-intercalated surface may act as an adsorption template by atoms and molecules, similar to the moiré patterns present in graphene grown on Ir (111).[35]

Looking forward, quantitative analysis such as density functional theory calculations can be performed to compare the STM images obtained with our proposed model of the structure of the semi-intercalated graphene. Tight binding calculations can also be carried out to obtain the electronic band structure of such a system to corroborate

the STS findings. PES measurements should also be carried out to determine the electronic band structure of such a system.

In the final section of this chapter we have shown that at a higher annealing temperature of 900°C, complete fluorine intercalation occurs and charge-neutral quasi free-standing graphene layer is obtained. The as-formed quasi free-standing epitaxial graphene is investigated using STM/STS measurements. The STM/STS results confirm the associated physical and electronic changes due to intercalation and these changes were further verified using PES. The intercalation process is highly selective and only takes place on the buffer layer due to its weak nature of intercalation. This allows the formation of purely monolayer epitaxial graphene even if the initial substrate surface was inhomogeneous and had regions of monolayer graphene prior to intercalation.

In addition to the formation of a quasi-freestanding graphene layer, dilute amounts of nanostructures which locally alter the electronic structure of graphene are also observed and attributed to fluorine atoms bonded to graphene from below. Nanostructures formed due to fluorine adsorption could impact the electronic transport of the graphene by acting as localized scattering centres. However, such adatoms also provide the possibility of local tuning of the electronic properties of graphene. The samples are also stable up to 1200^{0}C, higher than other similar intercalated products.[14-16] It also remains very stable in ambient atmospheres for up to five months with no change detected under core level PES, STM and STS measurements. This stability under ambient conditions indicates its robustness for implementation in future applications.

Intercalated quasi-free-standing graphene have potential applications in future devices where higher mobility is required, a quality that Si-face epitaxial graphene lacks due to the interaction with the buffer layer. Recent reports have shown that a removal of the buffer layer improves the electron mobility of graphene as well as its temperature dependence.[51] In order to fully exploit this property, large surface areas of quasi free-standing graphene are required. As the size of the quasi-freestanding graphene is only limited by the amount of buffer layer on the sample surface, this can be achieved by using samples with sufficient areas of buffer layer. This is attainable under argon growth environments as demonstrated by Emtsev et. al..[3] Future works would include growing large areas of quasi-free-standing graphene for ARPES measurements to detect any novel electronic structures. Transport measurements should also be performed to quantify its electrical properties at the mesoscopic scale.

References

1. T. Ohta; A. Bostwick; T. Seyller; K. Horn and E. Rotenberg, *Science* **313**, 951-954 (2006).

2. C. Riedl; A.A. Zakharov and U. Starke, *Appl. Phys. Lett.* **93**, 033106 (2008).

3. K.V. Emtsev; A. Bostwick; K. Horn; J. Jobst; G.L. Kellogg; L. Ley; J.L. McChesney; T. Ohta; S.A. Reshanov; J. Röhrl; E. Rotenberg; A.K. Schmid; D. Waldmann; H.B. Weber and T. Seyller, *Nature Mater.* **8**, 203-207 (2009).

4. C. Riedl and U. Starke, *Phys. Rev. B* **76**, 245406 (2007).

5. P. Mallet; F. Varchon; C. Naud; L. Magaud; C. Berger and J.Y. Veuillen, *Phys. Rev. B* **76**, 041403(R) (2007).

6. W. Chen; S. Chen; D.C. Qi; X.Y. Gao and A.T.S. Wee, *J. Am. Chem. Soc.* **129**, 10418-10422 (2007).

7. C. Coletti; C. Riedl; D.S. Lee; B. Krauss; L. Patthey; K. von Klitzing; J.H. Smet and U. Starke, *Phys. Rev. B* **81**, 235401 (2010).

8. J. Choi; H. Lee; K.J. Kim; B. Kim and S. Kim, *J. Phys. Chem. Lett.* **1**, 505-509 (2010).

9. S. Barja; M. Garnica; J.J. Hinarejos; A.L. Vázquez de Parga; N. Martín and R. Miranda, *Chem. Commun.* **46**, 8198-8200 (2009).

10. L.G. Bulusheva; A.V. Okotrub and O.V. Boltalina, *J. Phys. Chem. A* **103**, 9921-9924 (1999).

11. S. Troyanov; P. Troshin; O. Boltalina; I. Ioffe; L. Sidorov and E. Kemnitz, *Angew. Chem. Int. Ed.* **40**, 2285-2287 (2001).

12. K. Kniaz; J. Fischer; H. Selig; G. Vaughan; W. Romanow; D. Cox; S. Chowdhury; J. McCauley; R. Strongin and A. Smith III, *J. Am. Chem. Soc.* **115**, 6060-6064 (1993).

13. M.T. Edmonds; M. Wanke; A. Tadich; H.M. Vulling; K.J. Rietwyk; P.L. Sharp; C.B. Stark; Y. Smets; A. Schenk; Q.H. Wu; L. Ley and C.I. Pakes, *J. Chem. Phys.* **136**, 124701 (2012).

14. C. Virojanadara; S. Watcharinyanon; A. Zakharov and L. Johansson, *Phys. Rev. B* **82**, 205402 (2010).

15. C. Riedl; C. Coletti; T. Iwasaki; A.A. Zakharov and U. Starke, *Phys. Rev. Lett.* **103**, 246804 (2009).

16. S. Oida; F. McFeely; J. Hannon; R. Tromp; M. Copel; Z. Chen; Y. Sun; D. Farmer and J. Yurkas, *Phys. Rev. B* **82**, 041411(R) (2010).

17. A.L. Walter; K.J. Jeon; A. Bostwick; F. Speck; M. Ostler; T. Seyller; L. Moreschini; Y.S. Kim; Y.J. Chang; K. Horn and E. Rotenberg, *Appl. Phys. Lett.* **98**, 184102 (2011).

18. H. Şahin; M. Topsakal and S. Ciraci, *Phys. Rev. B* **83**, 115432 (2011).

19. K.J. Jeon; Z. Lee; E. Pollak; L. Moreschini; A. Bostwick; C.M. Park; R. Mendelsberg; V. Radmilovic; R. Kostecki; T.J. Richardson and E. Rotenberg, *ACS Nano* **5**, 1042-1046 (2011).

20. D.K. Samarakoon; Z. Chen; C. Nicolas and X.Q. Wang, *Small* **7**, 965-969 (2011).

21. R.R. Nair; W. Ren; R. Jalil; I. Riaz; V.G. Kravets; L. Britnell; P. Blake; F. Schedin; A.S. Mayorov; S. Yuan; M.I. Katsnelson; H.M. Cheng; W. Strupinski; L.G. Bulusheva; A.V. Okotrub; I.V. Grigorieva; A.N. Grigorenko; K.S. Novoselov and A.K. Geim, *Small* **6**, 2877-2884 (2010).

22. Y. Fujikawa; J. Sadowski; K. Kelly; K. Nakayama; E. Mickelson; R. Hauge; J. Margrave and T. Sakurai, *Jpn. J. Appl. Phys* **41**, 245-245 (2002).

23. J. Sadowski; Y. Fujikawa; K. Kelly; K. Nakayama; T. Sakurai; E. Mickelson; R. Hauge and J. Margrave, *J. Cryst. Growth* **229**, 580-585 (2001).

24. K.J. Rietwyk; M. Wanke; H.M. Vulling; M.T. Edmonds; P.L. Sharp; Y. Smets; Q.H. Wu; A. Tadich; S. Rubanov; P.J. Moriarty; L. Ley and C.I. Pakes, *Phys. Rev. B* **84**, 035404 (2011).

25. S.W. Poon; W. Chen; A.T.S. Wee and E.S. Tok, *Phys. Chem. Chem. Phys.* **12**, 13522 (2010).

26. U. Bangert; M.H. Gass; A.L. Bleloch; R.R. Nair and A.K. Geim, *Phys. Status Solidi A* **206**, 1117-1122 (2009).

27. F. Varchon; P. Mallet; J.Y. Veuillen and L. Magaud, *Phys. Rev. B* **77**, 235412 (2008).

28. M. Cranney; F. Vonau; P.B. Pillai; E. Denys; D. Aubel; M.M. De Souza; C. Bena and L. Simon, *EPL* **91**, 66004 (2010).

29. A. Bostwick; K. Emtsev; K. Horn; E. Huwald; L. Ley; J. McChesney; T. Ohta; J. Riley; E. Rotenberg; F. Speck and Seyller Th., *Adv. Solid State Phys.* **47**, 159-170 (2008).

30. Y. Zhang; V. Brar; F. Wang; C. Girit; Y. Yayon; M. Panlasigui; A. Zettl and M. Crommie, *Nature Phys.* **4**, 627-630 (2008).

31. V. Brar; Y. Zhang; Y. Yayon; T. Ohta; J. McChesney; A. Bostwick; E. Rotenberg; K. Horn and M. Crommie, *Appl. Phys. Lett.* **91**, 122102 (2007).

32. B. Premlal; M. Cranney; F. Vonau; D. Aubel; D. Casterman; M.M. De Souza and L. Simon, *Appl. Phys. Lett.* **94**, 263115-263115 (2009).

33. J. Choi; H. Lee and S. Kim, *J. Phys. Chem. C* **114**, 13344-13348 (2010).

34. P. Lauffer; K.V. Emtsev; R. Graupner; T. Seyller and L. Ley, *Phys. Rev. B* **77**, 155426 (2008).

35. R. Balog; B. Jørgensen; L. Nilsson; M. Andersen; E. Rienks; M. Bianchi; M. Fanetti; E. Lægsgaard; A. Baraldi; S. Lizzit; Z. Sljivancanin; F. Besenbacher; B. Hammer; T.G. Pedersen; P. Hofmann and L. Hornekær, *Nature Mater.* **9**, 315-319 (2010).

36. L. Jin; Q. Fu; R. Mu; D. Tan and X. Bao, *Phys. Chem. Chem. Phys.* **13**, 16655 (2011).

37. G.M. Rutter; J.N. Crain; N.P. Guisinger; T. Li; P.N. First and J.A. Stroscio, *Science* **317**, 219-222 (2007).

38. L. Simon; C. Bena; F. Vonau; D. Aubel; H. Nasrallah; M. Habar and J.C. Peruchetti, *Eur. Phys. J. B* **69**, 351-355 (2009).

39. V. Pereira; J. Lopes dos Santos and A. Castro Neto, *Phys. Rev. B* **77**, 115109 (2008).

40. X. Hong; S.H. Cheng; C. Herding and J. Zhu, *Phys. Rev. B* **83**, 085410 (2011).

41. K. Kelly; E. Mickelson; R. Hauge; J. Margrave and N. Halas, *Proc. Natl. Acad. Sci. USA* **97**, 10318-10321 (2000).

42. L. Johansson and F. Owman, *Phys. Rev. B* **53**, 13793-13802 (1996).

43. L. Tapaszto; G. Dobrik; P. Lambin and L. Biro, *Nature Nanotech.* **3**, 397-401 (2008).

44. M. Han; B. Özyilmaz; Y. Zhang and P. Kim, *Phys. Rev. Lett.* **98**, 206805 (2007).

45. M.Y. Han; J.C. Brant and P. Kim, *Phys. Rev. Lett.* **104**, 056801 (2010).

46. P. Gallagher; K. Todd and D. Goldhaber-Gordon, *Phys. Rev. B* **81**, 115409 (2010).

47. X. Liang; Y.S. Jung; S. Wu; A. Ismach; D.L. Olynick; S. Cabrini and J. Bokor, *Nano Lett.* **10**, 2454-2460 (2010).

48. J. Bai; X. Zhong; S. Jiang; Y. Huang and X. Duan, *Nature Nanotech.* **5**, 190-194 (2010).

49. N.S. Safron; A.S. Brewer and M.S. Arnold, *Small* **7**, 492-498 (2011).

50. M. Wang; L. Fu; L. Gan; C. Zhang; M. Rümmeli; A. Bachmatiuk; K. Huang; Y. Fang and Z. Liu, *Sci. Rep.* **3**, 1238 (2013).

51. F. Speck; J. Jobst; F. Fromm; M. Ostler; D. Waldmann; M. Hundhausen; H.B. Weber and T. Seyller, *Appl. Phys. Lett.* **99**, 122106 (2011).

Chapter 4: Selective fluorination of graphene using $C_{60}F_{36}$

4.1 Introduction

Fluorination of graphene has attracted numerous studies recently due to its scalability and ease of process. Fluorinated graphene has a wide range of applications that varies with the fluorine concentration. Dilute fluorinated graphene has been shown to exhibit colossal negative magnetoresistance due to the influence of the fluorine adatoms and their presence induces local magnetic moments and spin-flip scattering in graphene.[1,2] At higher concentrations of fluorine, a band gap in the electronic structure of graphene is formed when sufficient amounts of fluorine are covalently bonded to the surface, breaking the delocalised π bond network. Such high concentrations of fluorination result in an electronic band gap of up to 3eV while still maintaining the mechanical strength of pristine graphene.[3-5] Fluorinated graphene has also been employed in the promotion of neural stem cell formation.[6]

Initial methods of graphene fluorination involve exfoliation of graphite fluoride[7,8] but the process has a low yield and the structural quality of the fluorinated graphene produced is compromised. Recent methods of synthesis involve usage of fluorine containing gaseous species. Such methods include the use of F plasma or high temperature exposure of F_2 gas to the graphene surface.[9,10] However, exposure of graphene to plasma and high temperature processes affect the quality of the fluorinated graphene formed. A low temperature procedure which involves decomposition of toxic XeF_2 has also been demonstrated to fluorinate graphene.[3,4,11] However these processes result in an undirected functionalization of the sample. In order to achieve selectivity of

the area to be functionalized, a directed form of fluorination is required. Localized methods of functionalization are currently limited to using a laser to selectively excite fluorinated polymers coated on graphene.[12]

In this section, $C_{60}F_{36}$ molecules are deposited on top of graphene to provide an alternative means with which to selectively fluorinate the surface using the molecules as a source. $C_{60}F_{36}$ molecules are chosen as a similar molecule, the $C_{60}F_{48,}$ has been employed by Rietwyk et. al. as a fluorine source to selectively fluorinate the (0001) surface of diamond using photon beams.[13] In our experiment, synchrotron radiation is also used to excite the molecular layers of $C_{60}F_{36}$ deposited on the graphene surface. During irradiation, electrons are excited from both substrate and molecules. Fluorine dissociation then takes place through electron impact ionization of the fluorofullerenes or through the capture of thermal electrons by the molecules. The fluorine radicals produced then bond to the graphene surface. Since the photon beam is only 0.5 x 2 mm^2 in area and thus does not encompass the entire sample surface (3 x 10 mm^2), only the irradiated region of the molecular layer is excited, thus allowing selective fluorination. In the following discussion, we present our method of selective functionalization as well as the corresponding PES measurements. Further works as well as possible prospects of this technique are discussed at the end of this chapter.

4.2 Experimental Setup

PES measurements as well as fluorine dissociation by synchrotron radiation were carried out at the soft x-ray spectroscopy beam line of the Australia Synchrotron in a UHV chamber at a base pressure of 10^{-10} mbar.[13] All molecular deposition, annealing of the sample and PES studies were performed in-situ. Deposition of the molecules was

carried out by thermal evaporation from an effusion cell at 250°C while keeping the substrate at room temperature. The deposition rate of the molecules was calibrated using a quartz crystal microbalance (QCM) which has the density setting approximated to literature values of 2.71 g/cm^3. PES measurements were performed before deposition to check for purity of the surface as well as after deposition to ensure that the deposition rate indicated from the QCM was properly calibrated. C1s peaks belonging to graphene and $C_{60}F_{36}$ were used for the calibration.

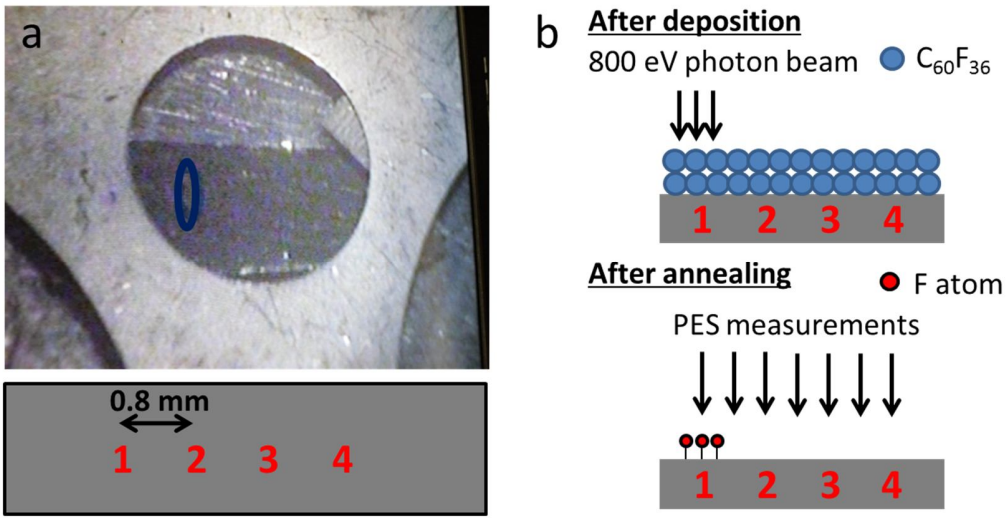

Figure 4.1 a) Top: Sample set in holder to be used. Bottom: Positions 1-4 marked on the sample. b) Schematic showing fluorination process and PES measurements. Top: Irradiation of the molecular layer only at position 1. Bottom: PES measurements carried out for all four positions to identify location and efficiency of fluorination.

The sample holder used in this experiment is shown in Figure 4.1a. The location of the beam as well as its spot size on the sample is represented by the blue oval on the sample. This is determined by allowing the beam to first impinge on an yttrium aluminium garnet (YAG) crystal which fluoresces on irradiation. To find out whether localized fluorination is achieved, we select four positions (1 - 4) on the sample,

separated by 0.8 mm, which is longer than the width of the beam spot (indicated in Figure 4.1a). The area on the extreme left (position 1) is selected for fluorination, i.e. beam irradiation of the deposited molecules is carried out only at this spot. In order to determine the efficiency and localisation of the fluorination process, 3 other locations, namely position 2-4 are analysed using PES after the molecules have been desorbed from the surface.

The fluorination process shown in Figure 4.1b and is described as follows. 2 ML of $C_{60}F_{36}$ is first deposited onto the sample at room temperature. This quantity of $C_{60}F_{36}$ is chosen to ensure maximal coverage of the graphene surface as well as sufficient amounts of fluorine for the process. Next, photon beams with energies of 800eV is used to irradiate position 1 for a period of 2 hours. Beam energy of 800eV was chosen to allow simultaneous excitation of the molecules and monitoring of the evolution of the C 1s peaks during irradiation. After irradiation, annealing of the sample at 250°C is carried out to remove the molecules from the surface and PES measurements are then carried out at all four positions. This sequence of events is repeated four times with PES studies performed before and after each procedure. The photon energies used in the PES measurements are calibrated against the binding energy of Au 4f core levels of a clean sputtered gold foil in the chamber. For NEXAFS, the intensity variations of the photon beam at different energies are normalised using reference signals taken from carbon residue present on the gold mesh which is in the path of the beam. The Auger electron yield is collected in the NEXAFS measurements to obtain surface sensitive information.

4.3 Results and Discussion

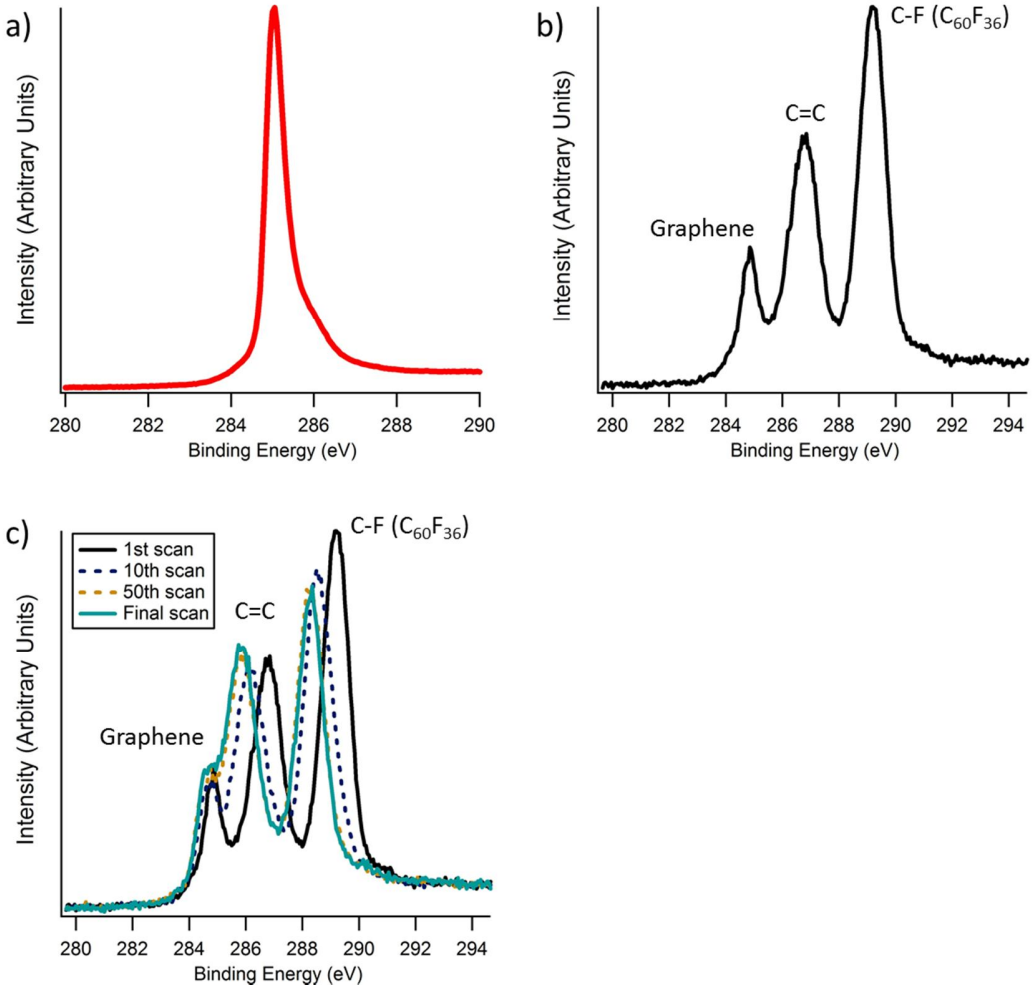

Figure 4.2 a) C1s spectra of pristine epitaxial graphene on SiC (0001) with photon energy 350eV. b) C1s spectra after molecular deposition with photon energy 800eV. c) Successive scans of C1s spectra of graphene taken after molecular deposition at photon energy of 800eV. Legend indicates the order of the spectra. Subsequent scans after the 50^{th} scan result in no further changes to the signals. The intensities each spectrum has been normalised against the photon flux present at the time of measurement.

A representative C1s spectrum before and after molecular deposition is shown in Figure 4.2a and b respectively on the next page. In Figure 4.2a, the C 1s peak of pristine epitaxial graphene is measured to be located at 285.1 ± 0.1eV with a shoulder at 286.0 ± 0.1eV belonging to the C 1s orbitals of the atoms in the buffer layer. After deposition, we

observe three C 1s core level peaks in Figure 4.2b. The graphene associated peak is located at 284.9 ± 0.1eV. This peak is 0.2eV lower than the binding energy for the C 1s peak of pristine graphene due to the doping of the electron acceptor $C_{60}F_{36}$ molecules which shifts the Fermi level of graphene towards the C 1s core level. The other two C1s core level peaks are attributed to the $C_{60}F_{36}$ molecules.

The carbon atoms in the molecules exist in two different chemical environments. The first peak at a binding energy of 286.7 ± 0.1eV is attributed to sp^2 hybridized carbon atoms (labelled C=C) not bonded to fluorine. The carbon atoms bonded to fluorine (labelled C-F) give rise to a photoelectron signal at the highest binding energy of 289.2 ± 0.1eV.[14,15] The binding energies of the C 1s states associated with the molecules are higher than those of pristine graphene due to to the environment of electron withdrawing fluorine. Note that the C1s peak values are based on the first PES spectrum taken immediately after molecular deposition to minimize shifts in the binding energies away from their original values due to beam damage.

After molecular deposition, repeated PES measurements were performed at position 1 with photon energies of 800eV to locally excite the molecules in the irradiated region and induce fluorine dissociation. The evolution of the C1s peaks with the number of scans is monitored and the representative spectrum taken at different scan intervals is described in Figure 4.2c. As the number of scans increases, we note that the intensity and binding energies associated with the C1s core levels of the $C_{60}F_{36}$ molecules vary. The C1s peak intensity from the C=C species increases and shifts towards a lower binding energy. Likewise, the C1s peak associated with the C-F species also shifts to lower binding energies, albeit with decreasing intensity. The binding energy for the C1s signal

of the C=C species shifts from a binding energy of 286.7 ± 0.1eV to 286.1 ± 0.1eV after 10 scans. The shift eventually saturates after 50 scans (note that each scan has been normalized against the photon flux at time of data acquisition) and the final position of the binding energy is at 285.9 ± 0.1eV. Similarly, the C1s signal of the C-F species shifts to a lower binding energy of 288.5 ± 0.1eV and stops at a binding energy of 288.4 ± 0.1eV after the 50th scan. Further scans induce no additional variations in their intensity and position. This shift is attributed to fluorine dissociation from the parent molecules. As the C-F bonds are broken and fluorine is removed, the carbon atoms of the C=C and C-F species are now in a less electron withdrawing environment and hence the binding energies associated with the carbon atoms in both chemical environments decrease. Fluorine dissociation also results in a decrease in C-F species in the molecules while at the same time increasing the relative population of C=C species in the molecules. This is reflected in a slight increase (2 ± 3 %) and decrease (16 ± 3%) in the intensity of the C=C and C-F related C 1s peaks respectively. As the C=C related peak intensity increases by 2% while the C-F related peak intensity decreases by 16%, we infer that not all C atoms of the molecules form double bonds after fluorine is removed. Not all the C atoms of the molecules form a double bond after fluorine is removed. Saturation in the binding energy level shifts indicates that 50 scans at 800eV are sufficient for complete fluorine dissociation.

The variations in binding energies and intensities of the molecular related peaks indicate fluorine dissociation due to the photon irradiation with energies of 800eV. The dissociation, according to analogous experiments performed for $C_{60}F_{48}$ on diamond, most likely take place via electron impact ionization of the fluorofullerenes by the

photoexcited electrons generated from the substrate[13] or through the capture of low energy secondary electrons by the molecules which then forms an energetic anion from which fluorine atoms dissociate.[16] The C1s peak signal belonging to graphene experiences no change in both intensity and binding energy with repeated scans. This implies that there is no damage done by the synchrotron radiation to graphene. Likewise, there is no significant desorption of the molecular layers during irradiation. Such desorption would have resulted in an increase in the graphene C 1s substrate signal due to decreased molecular coverage. After repeated PES scans at 800eV, the sample is annealed at 250°C for an hour to desorb the molecules. Note that the entire cycle is repeated four times and measured with PES at every stage of the process, with each cycle starting with molecular deposition, followed by photon-induced fluorine dissociation and finally desorption of the molecules through sample annealing.

After desorption of $C_{60}F_{36}$ molecules, PES measurements are taken at all 4 positions on the sample and the spectra are shown in Figure 4.3. The C 1s, Si 2p, F 1s core level signals are obtained after every cycle at various photon energies and measurement angles. Only one irradiated region (position 1) and two non-irradiated regions (position 2 and 3) are shown for clarity. PES data for position 4 (not shown) is identical to those taken at position 2 and 3. Figure 4.3a shows the C 1s related signals taken at 800eV after the fourth and final dissociation is carried out. The lack of signature signals associated with the $C_{60}F_{36}$ molecules, namely the C=C and C-F related signals at 286.7 ± 0.1eV and 289.2 ± 0.1eV, implies that the molecules have desorbed from the surface after annealing and do not interfere with the PES measurements. The peak and shoulders associated with epitaxial graphene on SiC (0001) are observed. The main

graphene C 1s peak is situated at 285.0 ± 0.1eV, the buffer layer associated signal is at 285.8 ± 0.1eV and the signal contributed by the bulk SiC atoms is located at 284.3 ± 0.1eV. The region irradiated (position 1) has much higher intensity of the C-F and C-F_2 related signals, located at 288.3 ± 0.1eV and 290.4 ± 0.1eV respectively, compared to the surrounding regions that were not irradiated. These binding energies are similar to previous reports for fluorinated graphene.[4,11]

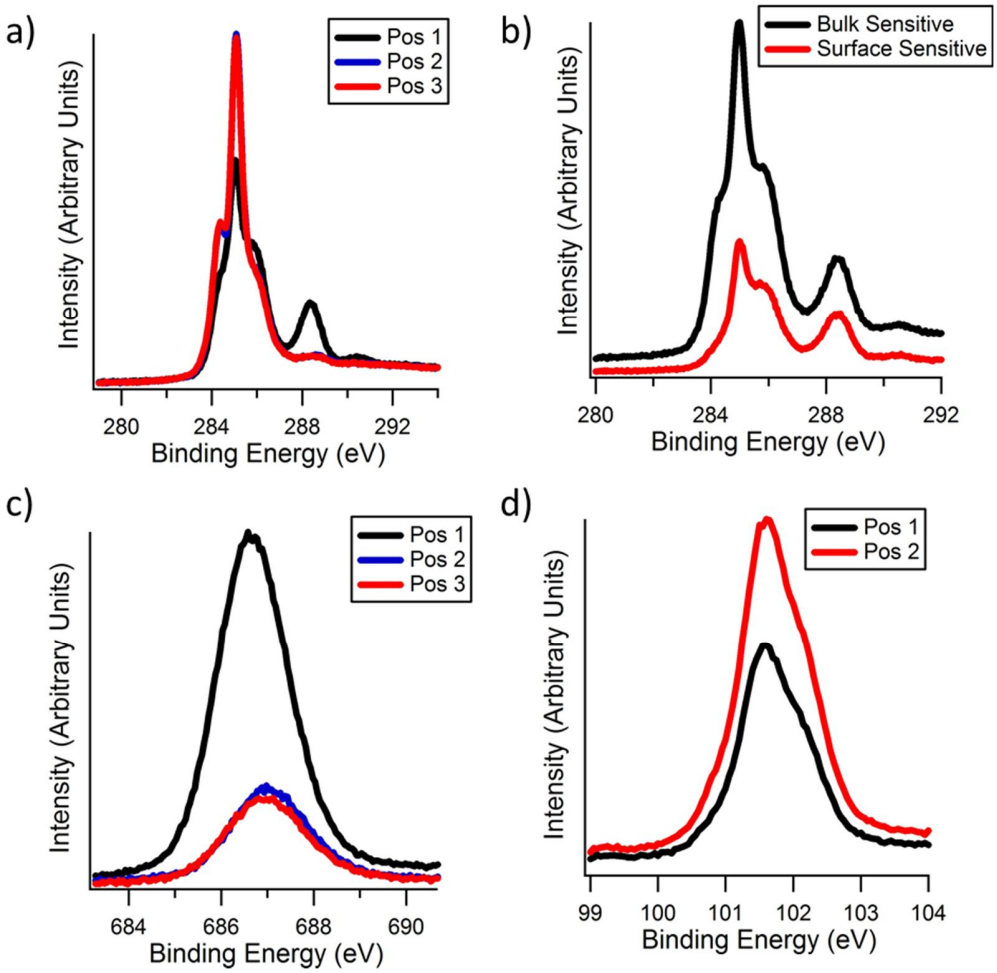

Figure 4.3 a) C1s core level spectra measured at positions 1, 2 and 3 with photon energy of 800eV. Spectrum of position 2 (blue) and 3 (red) are overlapped. b) C1s core level spectra measured at position 1 with photon energy of 800eV. Measurements are taken at two emission angles, normal emission (black) and glancing emission (red). c) F1s spectrum taken at positions 1, 2 and 3 with photon energy of 800eV. d) Si 2p spectrum taken at positions 1 and 2 with photon energy of 160eV. Spectra have been offset for clarity.

The higher binding energy of the C-F_2 related signal is due to a larger fluorine concentration in the surroundings of the carbon atoms probed. C-F_2 species could have been formed at the defect or edge sites of the graphene layer. The binding energies for both C-F related signals after annealing are lower than those of the $C_{60}F_{36}$ molecules (Figure 4.3b) due to the lower concentration of fluorine which results in less electro-positivity of the carbon atoms. To determine the coverage of covalently bonded fluorine, we compute the ratio of the amount of fluorine bonded to the carbon atoms against the total amount of graphene carbon atoms as such:

$$\frac{\left(\text{C-F}\right)_{\text{peak area}} + 2\,\text{x}\left(\text{C-F}_2\right)_{\text{peak area}}}{\left(\text{C-F}\right)_{\text{peak area}} + 2\,\text{x}\left(\text{C-F}_2\right)_{\text{peak area}} + \left(\text{C signal for graphene}\right)_{\text{peak area}}} \qquad (4.1)$$

The coefficient of 2 for the (C-F_2) peak area is due to the bonding of two fluorine atoms to a single carbon atom. Following the equation, we obtain coverage of covalently bonded fluorine of 49 ± 2% for position 1 and a much lower coverage of 4.2 ± 0.4% for positions 2 and 3. These observations point towards a much higher extent of fluorination of the surface in the irradiated regions compared to the surrounding ones. Thus, it implies that the extent of fluorination of a region can be selectively enhanced by using a photon beam to excite the molecules. In addition, there seems to be a reduction in the graphene related C1s peak signal for the irradiated region. This reduction can be explained by the formation of C-F bonds between the graphene carbon atoms and fluorine. The bond formation breaks the C=C bonds present in graphene and therefore results in the reduction of its associated C1s signal.

In order to determine the depth at which these C-F bonds are located, angular dependent PES investigations are performed. Figure 4.3b shows the comparison between the surface (red) and bulk (black) sensitive measurements taken for the C 1s core level of the irradiated regions. We observe that the relative intensity of both the graphene and C-F related peaks to the bulk C 1s signals of the SiC substrate at 284.3 ± 0.1eV are larger in the surface sensitive measurements as compared to that in the bulk sensitive measurements. This implies that the C-F related C 1s signals originate from the surface, similar to that from the graphene carbon atoms. Hence, fluorination takes place on the graphene surface rather than in the sub-surface bulk substrate.

Figure 4.3c shows the F 1s signal after irradiation and desorption of the molecules for the irradiated and non-irradiated regions. The peak area under the F 1s signal taken from the irradiated region is 3.6 times larger than those of the other regions, which should be expected from the much larger C-F related C 1s signal discussed earlier. However, when we compute the $F/C_{graphene}$ ratio using peak area of F 1s divided by peak area of C 1s signal of graphene carbon atoms, position 1 yields an $F/C_{graphene}$ ratio of 0.67 ± 0.02 while a ratio of 0.18 ± 0.01 and 0.14 ± 0.01 is obtained for positions 2 and 3 respectively. The calculated $F/C_{graphene}$ ratios are larger than the computed values for the coverage of covalently bonded fluorine. The discrepancy is attributed to non-covalently bonded fluorine. We hence take the difference between the F/C ratio and the ratio of covalently bonded fluorine atoms to give us the percentage of physisorbed fluorine against graphene carbon atoms. For position 1, the percentage obtained is 18 ± 4% while for position 2 and 3; a percentage of 14 ± 1% and 10 ± 1% are computed. Majority of the fluorine atoms on position 2 and 3 do not form covalent bonds with the graphene carbon atoms. The

similarity in these values for all three positions indicates that there exist physisorbed fluorine atoms that have diffused across the sample surface. These atoms could be left behind by the molecules during the thermal anneal as well as migration of fluorine atoms from the irradiated region to the surrounding areas after the irradiation/anneal procedure.

This is corroborated in the difference in binding energy between the F 1s core level signals of the irradiated and non-irradiated regions. The binding energy of the F 1s core level signal for the irradiated region, 686.6 ± 0.1eV is 0.4eV lower than that of the rest which is located at 687.0eV ± 0.1eV. We hypothesize that the lower binding energy is due to the covalent bonding of fluorine to the graphene carbon atoms. This results in a charge transfer and hence electronegativity of the fluorine atoms which causes the F 1s electron binding energy to decrease. Meanwhile, the majority of the fluorine on the other regions is not covalently bonded to the graphene surface as analysed from the ratios computed previously. This measurement once again indicates that the irradiation enhances the concentration of fluorine bonded formation with graphene (covalent bonding on irradiated regions versus non-covalently bonded fluorine on regions that were not irradiated).

In contrast to our previous experiment in which fluorine was intercalated when the sample was annealed at lower temperatures of 150°C in the absence of any irradiation, there are no traces of it detected in the Si 2p core levels. Figure 4.3d describes the Si 2p core levels located at 101.6 ± 0.1eV for both irradiated and non-irradiated areas. Note that the peak observed for either region is characteristic of only a single 2p doublet, in contrast to our previous results (Figure 3.12a in Chapter 3) for fluorine intercalation, in which the Si 2p signal measured consists of two doublets. This confirms that the Si atoms

of the substrate exist only in its original chemical environment and hence no fluorine intercalation has taken place. This disparity with our observations for $C_{60}F_{48}$ in the previous chapter is attributed to the higher temperature of 250°C during annealing which causes molecular desorption prior to any sufficient intercalation taking place. It has also been shown in mass spectrometric studies that thermal dissociation of fluorofullerenes produces fluorine in even numbers, i.e.: in the molecular form.[17] Thus, this facilitates diffusion of fluorine into the interface between buffer layer and substrate as compared to irradiation of the fluorofullerene layer which would have produced fluorine atoms[13,16] that bond immediately to the graphene surface prior to any intercalation.

To ascertain the effect of fluorination on the graphene structure, NEXAFS is performed and the results are shown in Figure 4.4. The measurements are done prior to any molecular deposition and after undergoing the irradiation-anneal cycle twice and for four times respectively. NEXAFS measurements are only shown for the irradiated regions as the measurements for the non-irradiated regions have no observable deviation from that of pristine graphene. Only Auger electron yield is shown for both incident angles as there are no observable differences for the fluorescence yield data obtained between irradiation/anneal cycles, indicating that only the near surface regions are affected by the fluorination process. Figure 4.4a describes the NEXAFS results for an incoming photon beam at a glancing incidence angle of 20° to the surface plane. This particular beam incidence angle would result in an enhanced amount of the electrons being excited from the C 1s to the out-of-plane π anti-bonding states, otherwise known as the π^* resonance.

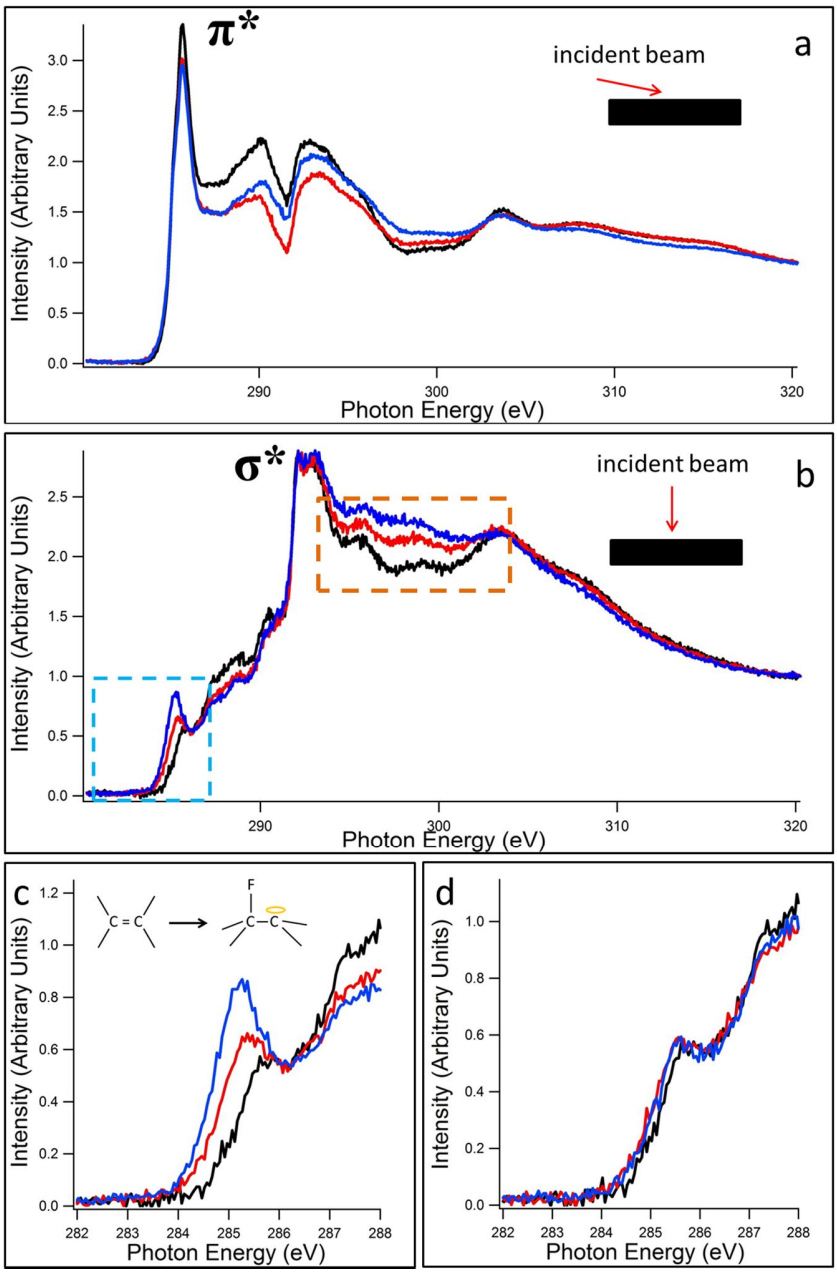

Figure 4.4 NEXAFS taken about the K edge of C1s orbitals at irradiated region (position 1) with incident angle of a) 90°, b) 20° and c) is a close up of the data in the region (outlined by a blue box in b)) about 285eV photon energy, where a new peak is observed. Inset: Schematic process showing in plane dangling bond state formed after fluorination. Three spectra are shown for each figure, (black) pristine epitaxial graphene, after irradiation and annealing procedure twice (red) and four times (blue). d) NEXAFS taken at an incident angle of 90° for the non-irradiated region (position 4) showing absence of new states in the same photon energy range of c). All spectra have been normalised against the background intensity at 282eV photon energy.

The labeled peak at 285.7 ± 0.1eV is related to the C1s → π* transitions while the peak located at 290.0 ± 0.1eV is attributed to the transitions to the interlayer state present in graphene as reported by Pacilé et. al..[18] The intensity of the electrons excited from the C 1s to the in-plane σ* state at 292.1 ± 0.1eV is suppressed as the alignment of the electric field of the photon beam with the associated orbitals is minimal. We note that the graphene related π* and interlayer peaks decreases with each irradiation/anneal cycle. This decrease is due to the breaking of the sp^2 configuration and hence elimination of the out of plane π* of the C=C bonds present in graphene by the formation of C-F bonds. This is consistent with the lower C 1s peak intensity of graphene measured in position 1 (Figure 4.3a). Figure 4.4b describes the NEXAFS measurements taken with a photon beam along the surface normal. In this configuration, the excitation of electrons from the C 1s orbitals to the in-plane σ* anti-bonding states is enhanced. The C 1s transitions to the graphene related σ* peaks are labeled and are located at 292.1 ± 0.1eV and 292.9 ± 0.1eV. The peaks (outlined by a brown box) present for the photon energies of 295.7eV ± 0.1eV and 298.4 ± 0.1eV are related to the bulk 4H-SiC peaks as reported by Tallarida et. al..[19] These peaks are observed to be increasing with additional irradiation/anneal cycles. Such an increase implies that there may be etching of the graphene surface, resulting in a decrease attenuation of the bulk signals and hence enhanced intensity of these bulk related peaks. In addition, after the region is irradiated and annealed, changes in the NEXAFS spectra occur near the Fermi level.

Figure 4.4c and d shows a zoom-in view for the photon energies (outlined by a blue dotted box in Figure 16b) used in electronic transitions between states near the Fermi level of the irradiated and non-irradiated regions respectively. Pristine epitaxial

graphene has a peak at 285.7 ± 0.1eV which belongs to the bulk 4H-SiC and can be seen in both Figure 4.4c and d. We note that after position 1 goes through each irradiation-anneal cycle, a new peak evolves at 285.4 ± 0.1eV in Figure 4.4c. This peak was not observed for pristine epitaxial graphene as well as the other non-irradiated regions (Figure 4.4d). This peak is attributed to the in-plane σ dangling bond states of graphene which are produced when fluorine atoms covalently bond to one of the carbon atoms, breaking the π bond present in the original C=C bond to form a single C-F bond while leaving an in plane dangling bond state behind (inset of Figure 4.4c), as reported by Kiguchi et. al..[20] In their experiments, nanographene in activated carbon fibers was fluorinated and new σ dangling bond related states were observed at photon energies smaller than that of the π* state by 0.6eV. This is similar to our observations of an energy difference of 0.4eV between the π* state of pristine graphene and this new peak.

Therefore, the NEXAFS observations imply that irradiation of the molecule covered graphene surface prior to annealing does promote the formation of covalently bonded fluorine as this peak was not detected in the other regions. C-F bond related peaks at about 290eV are not detected in our experiments due to the overlapping of other signals from the substrate as well as graphene. Furthermore, fluorine etching of the surface also took place, resulting in an increased intensity of the SiC bulk peaks.

4.3 Conclusion and Outlook

In summary, selective fluorination of graphene using $C_{60}F_{36}$ molecules and synchrotron radiation as a writing tool has been demonstrated. The extent of fluorination and formation of covalently bonded fluorine, as seen in the C1s and F1s signals, is greatly enhanced in the region that was irradiated with the photon beam as compared to

its surrounding regions. This was corroborated by NEXAFS measurements which showed that only the region that was irradiated prior to annealing display peaks related to σ dangling bond states produced by covalent bonding of fluorine. Compared to stepwise thermal annealing of $C_{60}F_{48}$ (Chapter 3), fluorine intercalation was not observed. However, the measurements also imply that there is noticeable etching of the graphene surface. Such etching can be detrimental when the exposed carbon vacancy sites are passivated by unwanted elements when the graphene is exposed to ambient surroundings. These edge states may also have interesting properties, depending on the type of edge it consists as well as the termination element (vacancy or fluorine).[20-23]

As this writing process can be used to direct the fluorination of the graphene surface, hybrid graphene-fluorinated graphene structures can be patterned and used to electronically isolate graphene. Such a method also circumvents the need for conventional patterning techniques that may introduce unwanted contaminants or damage to the graphene surface such as photolithography, etching and usage of masks to protect the desired areas. Selective fluorination using solid molecular sources also ensure that the risk and toxicity is kept to a minimum.

Additional investigations such as STM measurements can be done to ascertain the actual physical configuration of the graphene at the atomic scale after the fluorination process as well as to probe the properties of the fluorinated graphene. Well isolated covalently bonded fluorine may serve as source of magnetism and measurements to detect it can be performed in the future.[1,2] The fluorination process can also be further optimized by varying the annealing temperature as well as the photon energy used to minimize etching and maximize the extent of fluorination. Other types of halogenation

using chlorine and bromine or chemical modification of graphene may also be carried out using molecular carriers with different functional groups. An alternate source of excitation, such as lasers, which was demonstrated by the recent report on fluoro-polymers[12], can also be considered for carrying out the procedure in an ambient environment.

References

1. X. Hong; S.H. Cheng; C. Herding and J. Zhu, *Phys. Rev. B* **83**, 085410 (2011).

2. X. Hong; K. Zou; B. Wang; S.H. Cheng and J. Zhu, *Phys. Rev. Lett.* **108**, 226602 (2012).

3. K.J. Jeon; Z. Lee; E. Pollak; L. Moreschini; A. Bostwick; C.M. Park; R. Mendelsberg; V. Radmilovic; R. Kostecki; T.J. Richardson and E. Rotenberg, *ACS Nano* **5**, 1042-1046 (2011).

4. R.R. Nair; W. Ren; R. Jalil; I. Riaz; V.G. Kravets; L. Britnell; P. Blake; F. Schedin; A.S. Mayorov; S. Yuan; M.I. Katsnelson; H.M. Cheng; W. Strupinski; L.G. Bulusheva; A.V. Okotrub; I.V. Grigorieva; A.N. Grigorenko; K.S. Novoselov and A.K. Geim, *Small* **6**, 2877-2884 (2010).

5. K.J. Jeon; Z. Lee; E. Pollak; L. Moreschini; A. Bostwick; C.M. Park; R. Mendelsberg; V. Radmilovic; R. Kostecki; T.J. Richardson and E. Rotenberg, *ACS Nano* **5**, 1042-1046 (2011).

6. Y. Wang; W.C. Lee; K.K. Manga; P.K. Ang; J. Lu; Y.P. Liu; C.T. Lim and K.P. Loh, *Adv. Mater.* **24**, 4285-4290 (2012).

7. R. Zbořil; F. Karlický; A.B. Bourlinos; T.A. Steriotis; A.K. Stubos; V. Georgakilas; K. Šafářová; D. Jančík; C. Trapalis and M. Otyepka, *Small* **6**, 2885-2891 (2010).

8. S.H. Cheng; K. Zou; F. Okino; H.R. Gutierrez; A. Gupta; N. Shen; P.C. Eklund; J.O. Sofo and J. Zhu, *Phys. Rev. B* **81**, 205435 (2010).

9. J. Wu; L. Xie; Y. Li; H. Wang; Y. Ouyang; J. Guo and H. Dai, *J. Am. Chem. Soc.* **133**, 19668-19671 (2011).

10. F. Withers; M. Dubois and A.K. Savchenko, *Phys. Rev. B* **82**, 073403 (2010).

11. J.T. Robinson; J.S. Burgess; C.E. Junkermeier; S.C. Badescu; T.L. Reinecke; F.K. Perkins; M.K. Zalalutdniov; J.W. Baldwin; J.C. Culbertson; P.E. Sheehan and E.S. Snow, *Nano Lett.* **10**, 3001-3005 (2010).

12. W.H. Lee; J.W. Suk; H. Chou; J. Lee; Y. Hao; Y. Wu; R. Piner; D. Akinwande; K.S. Kim and R.S. Ruoff, *Nano Lett.* **12**, 2374-2378 (2012).

13. K.J. Rietwyk; M. Wanke; H.M. Vulling; M.T. Edmonds; P.L. Sharp; Y. Smets; Q.H. Wu; A. Tadich; S. Rubanov; P.J. Moriarty; L. Ley and C.I. Pakes, *Phys. Rev. B* **84**, 035404 (2011).

14. H.Y. Mao; R. Wang; J.Q. Zhong; S. Zhong; J.D. Lin; X.Z. Wang; Z.K. Chen and W. Chen, *J. Mater. Chem. C* **1**, 1491 (2013).

15. S. Kawasaki; T. Aketa; H. Touhara; F. Okino; O.V. Boltalina; I.V. Gol'd; S.I. Troyanov and R. Taylor, *J. Phys. Chem. B* **103**, 1223-1225 (1999).

16. Y.V. Vasil'ev; O.V. Boltalina; R.F. Tuktarov; V.A. Mazunov and L.N. Sidorov, *Int. J. Mass Spectrom. Ion Processes* **173**, 113-125 (1998).

17. A.A. Tuinman; P. Mukberjee and L.A. Adcock, *J. Phys. Chem.* **96**, 7584-7589 (1992).

18. D. Pacilé; M. Papagno; A. Rodríguez; M. Grioni; L. Papagno; Ç. Girit; J. Meyer; G. Begtrup and A. Zettl, *Phys. Rev. Lett.* **101**, 066806 (2008).

19. M. Tallarida; D. Schmeisser; F. Zheng and F. Himpsel, *Surf. Sci.* **600**, 3879-3883 (2006).

20. M. Kiguchi; K. Takai; V.L.J. Joly; T. Enoki; R. Sumii and K. Amemiya, *Phys. Rev. B* **84**, 045421 (2011).

21. G. Li; A. Luican-Mayer; D. Abanin; L. Levitov and E.Y. Andrei, *Nat. Commun.* **4**, 1744 (2013).

22. I.Y. Jeon; H.J. Choi; M. Choi; J.M. Seo; S.M. Jung; M.J. Kim; S. Zhang; L. Zhang; Z. Xia; L. Dai; N. Park and J.B. Baek, *Sci. Rep.* **3**, 1-7 (2013).

23. M. Maruyama; K. Kusakabe; S. Tsuneyuki; K. Akagi; Y. Yoshimoto and J. Yamauchi, *J. Phys. Chem. Solids* **65**, 119-122 (2004).

Chapter 5: Bimolecular Network on Epitaxial Graphene

5.1 Introduction

Periodic potentials (with lattice parameters larger than carbon interatomic distances) have been theoretically predicted to anisotropically renormalize the Fermi level of graphene, depending on the lattice parameters of the periodic potential as well as its amplitude.[1-5] This has been recently verified experimentally in angle resolved photoemission spectroscopy (ARPES) measurements of iridium atomic clusters deposited on a Graphene/Ir(111) substrate.[5] The deposited iridium atoms bond to specific regions of the moiré pattern found on the epitaxial graphene/Ir(111) surface, resulting in a potential superlattice as the carbon atoms at these regions change from a sp^2 to a sp^3 hybridization. The periodic potential resulted in a highly anisotropic Dirac cone with a difference of 70% between the group velocity of the electronic band in the ΓK direction and that perpendicular to it. A drawback of this method is the requirement of a specific metallic substrate to create the necessary moiré pattern on the graphene sheet as well as covalent bond formation between the adsorbates and graphene which can significantly affect the charge mobility in the graphene layer. Thus, it would be of interest to generate these periodic potentials without resorting to covalent bonding and study their effects on the electronic band structure of graphene.

This chapter describes an alternative implementation of these periodic potential through the use of two types of organic molecules, one having a p-type doping effect (F_4-TCNQ) and the other (6T) having no charge transfer with graphene. Bimolecular networks have been studied on graphite substrates and are expected to adsorb similarly

on graphene since their atomic structure and chemistry are similar.[6-8] As these molecules have unique packing arrangement in accordance with the ratio of their respective coverage[9], the lattice parameters of the potential superlattice on the graphene layer can be tuned by controlling the relative amounts of molecules deposited. For such a periodic potential to work, a few conditions need to be met. Firstly, the doping effect on graphene by these molecules needs to be localized sufficiently to create an effective periodic potential, as opposed to homogenously doping the entire graphene surface. In addition, the number of orientations and types of these networks should be minimized for ease of analysis of the ARPES data in the event of an observable effect. Hence, STM studies are first performed to characterize the bimolecular networks on graphene, followed by ARPES measurements to determine the effects of such these self-assembled molecules on graphene.

In this chapter, we demonstrate the successful formation and LT-STM characterization of a bimolecular network consisting of 6T and F4-TCNQ molecules deposited on a surface having both monolayer and bilayer epitaxial graphene on SiC(0001). Two dominant bimolecular networks corresponding to 1:1 and 1:2 F4-TCNQ to 6T molecular coverage ratio are observed. There is no discernible difference between the packing arrangements of molecules deposited on different number of graphene layers. The range of the doping effect of these molecules is found from STS performed over exposed graphene surfaces to be limited to a radius of about 4 nm. On further deposition of 6T molecules, a single bimolecular network can be obtained. PES and ARPES measurement are then performed for similar molecular coverages on monolayer epitaxial

graphene to determine the influence of this network on the graphene electronic band structure.

5.2 Experimental Details

Molecular deposition was carried out on a SiC (0001) substrate with both epitaxial monolayer and bilayer graphene of equal surface coverage on the same sample to verify the substrate effect on the resultant bimolecular network. The choice of molecules to create the aforementioned periodic potential is as such: F4-TCNQ, a known electron acceptor[10,11] and 6T,[11-13] are co-deposited on epitaxial graphene. Their chemical structures are shown in Figure 5.1. 6T is chosen as it has sulphur atoms, making it easier to identify the relative ratio between the 6T and F_4-TCNQ molecules when performing PES measurements.

The purpose of the LT-STM studies is twofold. First, any influence of graphene (monolayer and bilayer) on their packing arrangement is ascertained. Secondly, the orientations and lattice parameters of the superlattice generated by these molecules are determined. For this experiment, deposition of 6T (99% purity, Sigma Aldrich) and F4-TCNQ (99% purity, Sigma Aldrich) via evaporation from a Knudsen cell is always carried out at 110°C and 80°C respectively with the epitaxial graphene on SiC(0001) kept at room temperature. Molecules are deposited sequentially and not simultaneously. The order of deposition does not matter as they give the same bimolecular arrangements. The bimolecular network generated on the graphene surface is investigated under the LT-STM.

The preparation procedure for the molecular layer is then repeated on a fresh monolayer epitaxial graphene and the growth is monitored using synchrotron radiation based PES at room temperature performed at the Singapore Synchrotron Light Source. Deposition of the bimolecular network is carried out in-situ in an adjoining growth chamber and the temperature of evaporation for either molecule remains the same as before. The coverage of the F_4-TCNQ molecules is approximated using nominal thickness, which is determined through the attenuation of the Si 2p core level intensity of the SiC substrate. 6T molecules are deposited in increasing amounts after the initial deposition of F_4-TCNQ molecules. Since the 6T molecules and the F_4-TCNQ molecules have unique S 2p and N 1s photoelectron signatures respectively (refer to chemical structure in Figure 5.1), the coverage of 6T molecules deposited relative to the F_4-TCNQ molecules are compared using the S 2p and N 1s photoelectron signals. Deposition of the 6T molecules is ceased once the desired ratio between the populations of the two molecular species is attained.

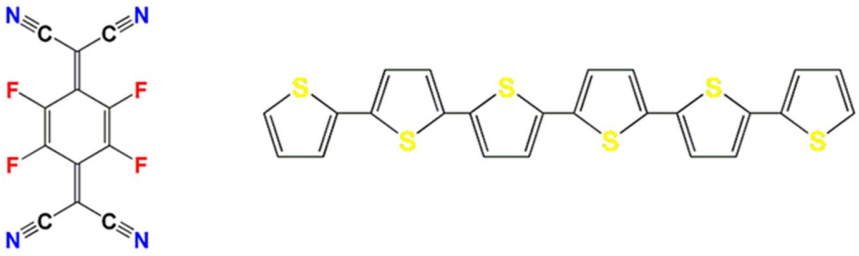

Figure 5.1 Chemical Structure of a) F_4-TCNQ and b) 6T molecule.

After the desired molecular coverage is obtained, low temperature ARPES (120K) is then conducted in situ to investigate the effects that the molecular network has on the electronic band structure of graphene. Three separate coverages are measured, i) pristine

monolayer graphene before deposition, ii) graphene with 0.1 nm of F_4-TCNQ deposited and iii) graphene with 1.8 : 1 ratio of 6T to F_4-TCNQ molecular coverage deposited. ARPES is conducted perpendicular to the Γ-K direction about the K point of the graphene Brilluoin Zone (Figure 5.6e) which is located at about $k_y = 1.7Å^{-1}$. The angular mode of the analyser is employed for data collection. Acceptance angles of 30° with 600 active channels are used in photoelectron detection with 0.1° steps used in the integration of electron counts.

UPS measurements were also conducted for 6T molecules deposited on epitaxial graphene on SiC (0001) with the substrate kept at room temperature. He Iα (21.2 eV) was used as the excitation source with an energy resolution of 0.1eV and an analyser work function of 4.3eV. The work function of the sample, ϕ can be determined through the equation:

$$\phi = h\nu - W \tag{5.1}$$

where $h\nu$ is the photon energy and W is the energy difference between the substrate Fermi level and low kinetic energy onset, otherwise known as secondary electron cut-off (SECO).[10] This energy difference, W is given by:

$$W = h\nu + V - \phi_a - \text{SECO} \tag{5.2}$$

Since we know the sample analyser, ϕ_a = 4.3eV and that a sample bias V = 5V was added, we can derive the work function of the material through the value of the SECO in the low photoelectron kinetic energy region of the UPS spectra.

5.3 STM/STS Measurements on Bimolecular Network

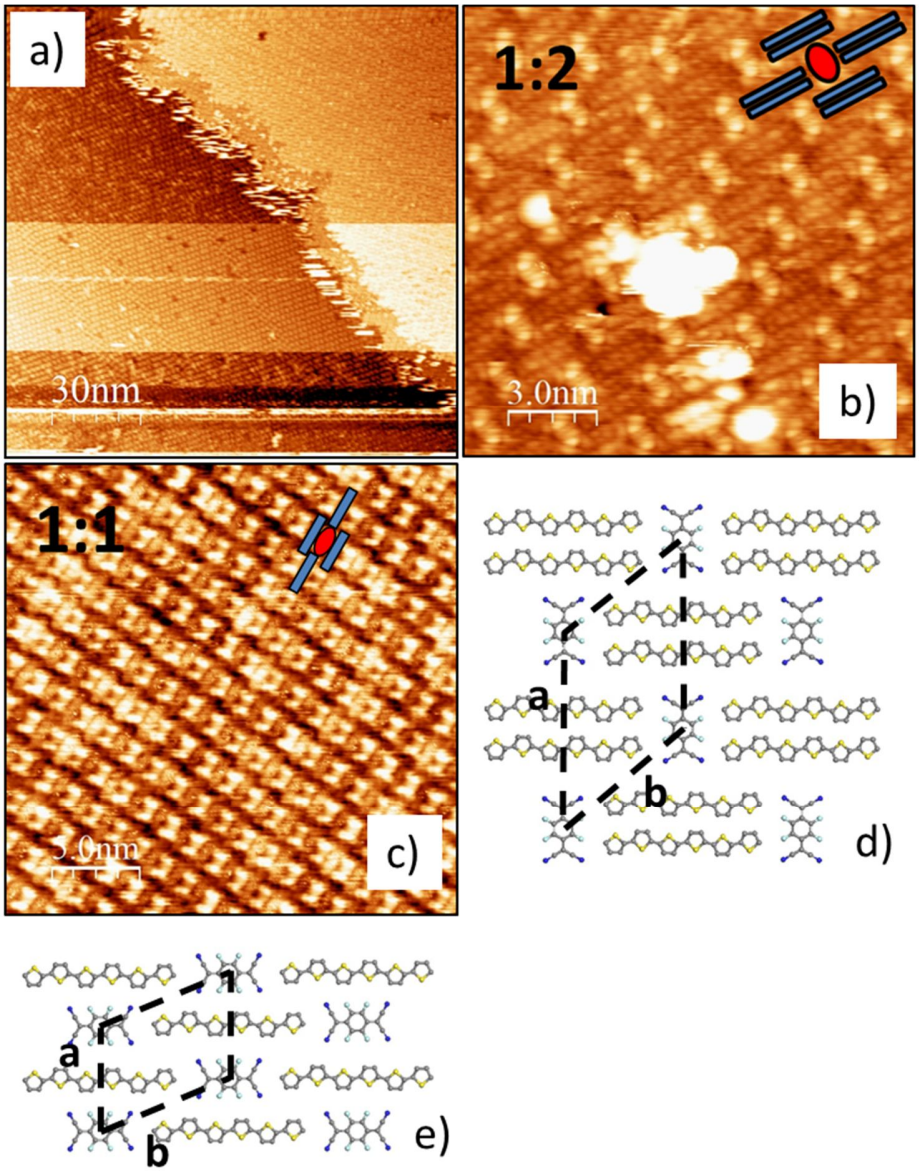

Figure 5.2 a) 150 x 150 nm^2 STM image showing coexistence of 2 different bimolecular networks formed after deposition of 6T and F_4-TCNQ. (V_{tip} = -1.65V, I = 100pA) High resolution STM image of b) 15 x 15 nm^2 showing bimolecular network with 1:2 F4-TCNQ to 6T coverage ratio (V_{tip} = -1.65V, I = 100pA) and c) 12 x 12 nm^2 showing bimolecular network with 1:1 F_4-TCNQ to 6T coverage ratio. (V_{tip} = -1.50V, I = 100pA) Molecular models are superimposed over their respective positions as a guide. Red ovals and blue rods represent F_4-TCNQ and 6T molecules respectively. Model of molecular packing structures for d) 1:2 F_4-TCNQ to 6T and e) 1:1 F_4-TCNQ to 6T coverage ratio. Lattice vectors **a** and **b** are indicated.

Figure 5.2a is the STM image showing the coexistence of two kinds of packing arrangement after 2.5 minutes of 6T and 2 minutes of F_4-TCNQ molecular deposition. F_4-TCNQ molecules are represented by shorter rods of 1.4 nm length (under positive tip bias) or "bow-tie shapes" (under negative bias) while 6T molecules are observed as long rods of about 3.1 nm in length under both negative and positive bias. This distinction in appearance corresponds to the chemical structure of each individual molecule (Figure 5.1). The two types of bimolecular networks have unit cells corresponding to F_4-TCNQ : 6T molecular ratios of 1:2 and 1:1 and are seen in the upper right and lower left of the STM image respectively.

Figure 5.2b and 5.2c shows the high resolution STM image of these particular networks and their corresponding models are described in Figures 5.2d and 5.2e. The lattice parameters are as such: $a = 2.8 \pm 0.1$ nm, $b = 2.3 \pm 0.1$ nm with an included angle of $50 \pm 2°$ for the 1:2 coverage ratios and $a = 1.6 \pm 0.1$ nm, $b = 2.1 \pm 0.1$ nm with an included angle of $71 \pm 2°$ for the 1:1 coverage ratio. These networks are formed due to the formation of hydrogen bonds between the peripheral F and N atoms of the F_4-TCNQ molecules with the H atoms present on the 6T molecules. Other bimolecular networks of low coverage also exist but do not have regular periodicity and therefore not shown. The coexistence between molecular networks of different molecular ratio is due to the variation in concentrations of the molecules deposited at different areas of the sample. No discernible differences are observed between the molecules deposited on monolayer or bilayer graphene.

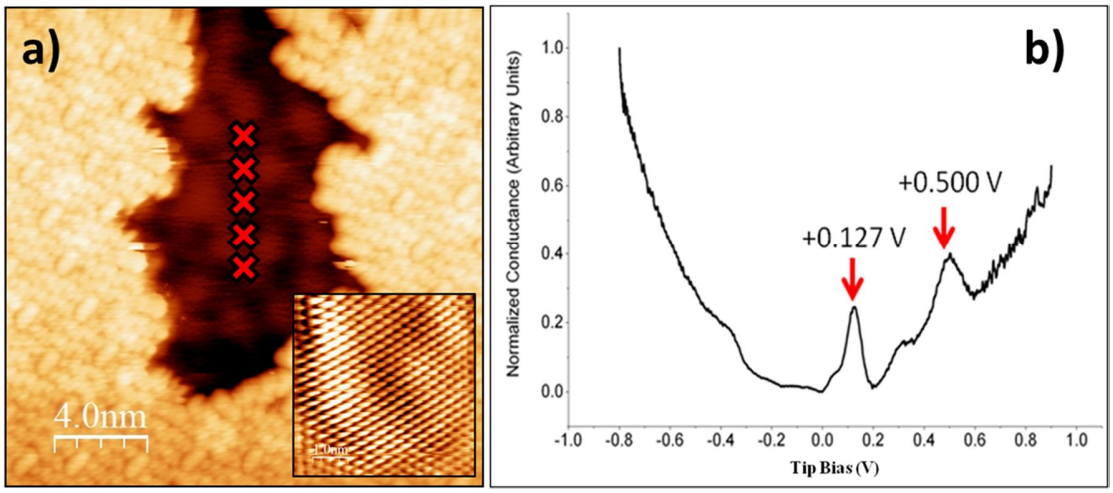

Figure 5.3 a) 20 x 20 nm^2 STM image showing defects in the molecular layer having 1:2 6T:F_4-TCNQ coverage ratio that exposes a region of bilayer graphene (V_{tip} = + 2.00V, I = 80pA) Red crosses indicate locations where STS is taken. Inset: 5 x 5 nm^2 STM image showing triangular lattice of bilayer graphene observed at low bias (V= 0.12V, 80pA). b) Averaged dI/dV spectra taken from random spots over the bilayer graphene. Red arrows indicate location of peaks in the local density of states.

To investigate the spatial range of the doping effect induced by the respective molecules, STS is performed over epitaxial graphene exposed within defects present in the molecular layer. An example of such a defect is shown in the STM image of Figure 5.3a. The exposed graphene layer is determined to be bilayer graphene from a high resolution low bias scan which shows only 3 out of the 6 atoms present in the honeycomb structure of graphene in the inset of Figure 5.3a. The STS is then measured in Figure 5.3b. The data is averaged over 500 spectra taken from 5 random spots taken about the centre of the exposed bilayer graphene within the defect so as to be collected sufficiently far away from the molecules to prevent measuring tunnelling conductance from the molecules themselves. No observable difference is noted between spots of different areas. The STS spectra obtained is characteristic of the bilayer graphene.[14] The peaks at 130 meV and 500 ± 10meV below the Fermi level are attributed to the increased density of

states at the saddle point of the apex of the bilayer graphene valence band and the bottom of the bilayer graphene conduction bands respectively. Such an increased density of states is due to the presence of band gap caused by an asymmetric charge distribution with more charge transferred from the substrate to the bottom graphene layer than to the top graphene layer.[14,15] The asymmetric charge distribution thus creates a potential difference between the two graphene sub-lattices which results in an electronic band gap. Taking the average of these two values thus approximates the location of the Dirac point at 310 ± 20meV below the Fermi level. As mentioned earlier, the conductance at the Dirac point does not tend to zero due to contribution from the underlying substrate. This value is similar to literature values obtained for bilayer graphene on SiC (0001).[14,15] This would mean that the extent of doping from the molecules decays completely within 4 nm from the molecules. Hence, there is a possibility of an effective periodic potential generated by this bimolecular network on graphene.

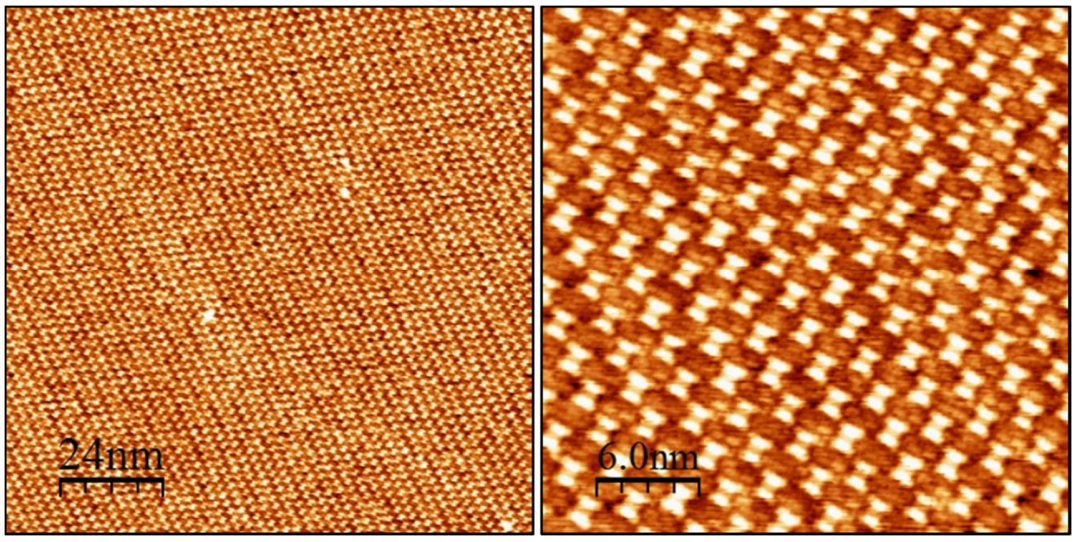

Figure 5.4 Left: 120 x 120 nm^2 STM image showing the dominant bimolecular packing arrangement after depositing 6T molecules in excess. Right: High resolution 30 x 30nm^2 STM image describing the 1:2 F_4-TCNQ to 6T molecular coverage ratio of the packing arrangement. (V_{tip} = -1.80V, I = 80pA)

A single bimolecular network on the entire graphene surface is generated when 6T molecules are further deposited in excess (an additional 5 minutes of 6T deposition) to the pre-existing molecular mixture as described in Figure 5.2. From large scale STM images, other than defective sites with missing molecules, the majority of the graphene surface is observed to be covered by only a single bimolecular network with a small coverage of 6T molecules in the second layer starting to develop. The F_4-TCNQ to 6T molecular coverage ratio of the dominant bimolecular network is 1 : 2, as shown in the STM image of Figure 5.4.

5.4 PES measurements of bimolecular network on monolayer epitaxial graphene

The molecular network that was observed previously under LT-STM is reproduced on epitaxial monolayer graphene to carry out PES measurements to ascertain the effect that the bimolecular network has on the graphene electronic structure. A 40s deposition of F_4-TCNQ, corresponding to nominal thickness of 0.1 nm, roughly equivalent to a coverage of 1/3 ML based on the assumption that a typical molecular layer of about 0.3nm in height[16], is first deposited followed by excess 6T molecules. As there is no *in-situ* STM to determine the ratio of the molecular composition on the surface, S 2p core levels of the sulphur atoms present on 6T and the N 1s core levels of the nitrogen atoms present on F_4-TCNQ are used to calibrate their relative ratio to achieve the desired 1:2 ratio between the two species.

Shown in Figure 5.5 is the core level PES data taken at different coverages of molecules. The N 1s peaks belonging to F_4-TCNQ shown in Figure 5.5a are located at binding energies of 398.0 and 401.5 ± 0.1eV.[10,17] The peak centred at the lower binding

energy is due to negatively charged anionic N^{1-} species present in F_4-TCNQ after it undergoes charge transfer and receives electrons from graphene, resulting in the N atoms of the molecule being electronegative and thus having a higher binding energy. The peak at 401.5eV is due to the shakeup peaks associated with the main N 1s peak.[18]

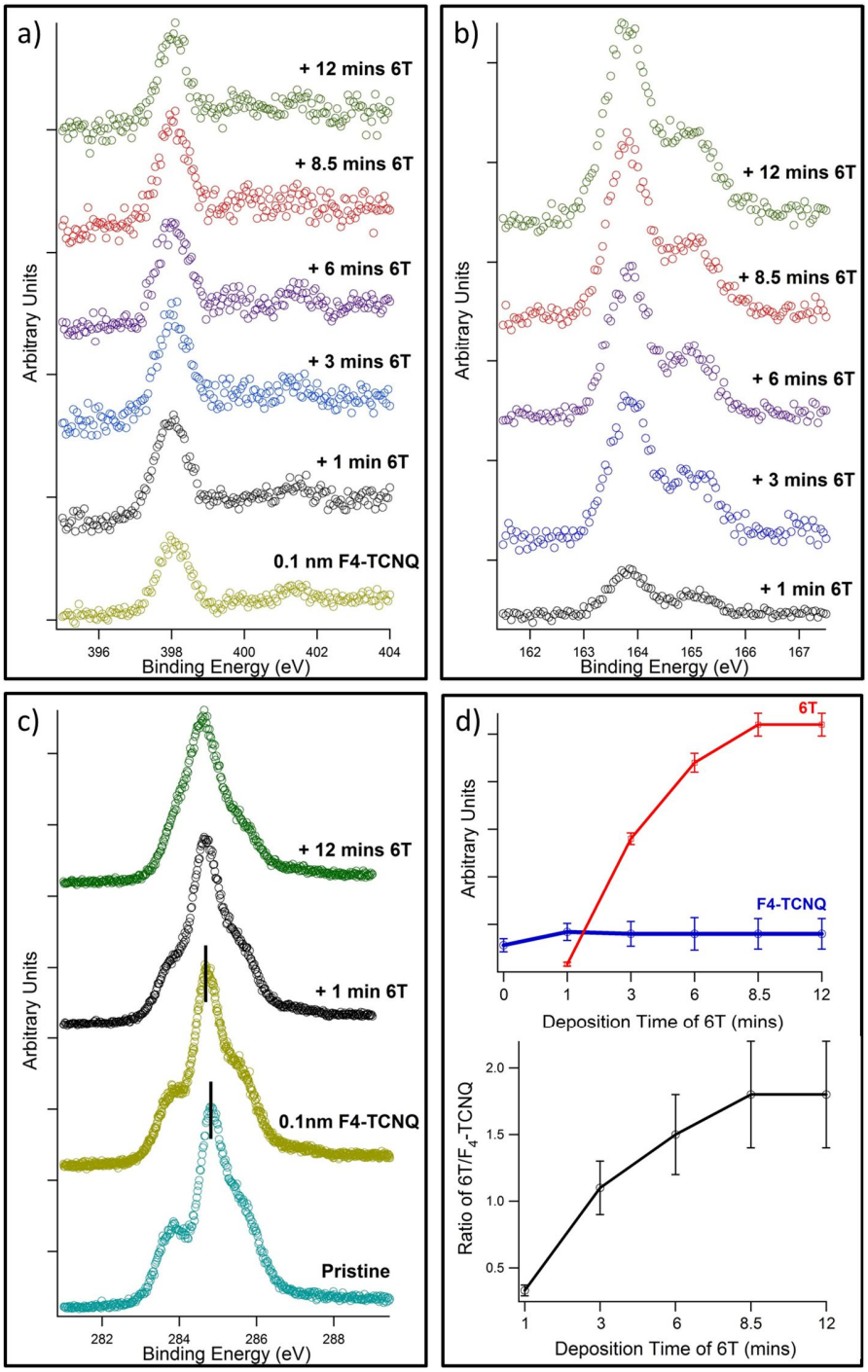

Figure 5.5 a) N 1s and b) S 2p core levels of a mixture of 6T and F_4-TCNQ molecules taken at different deposition times. The spectra associated with each deposition are labelled according to the deposition times of the molecules. c) C 1s core levels measured at different deposition times. Lines indicate position of graphene C 1s peak. All spectrums are taken with photon energy of 500eV. d) (Top) Comparison between relative amounts of 6T and F_4-TCNQ molecules using N 1s and S 2p photoelectron signal intensity. (Bottom) Ratio of 6T : F_4-TCNQ molecular coverage.

Shake up processes occur when photoelectrons simultaneously excite an atom and ejects an electron, resulting in a reduced kinetic energy of the electrons and therefore higher binding energy for the electrons emitted from the same core level. We do not observe the presence of the charge neutral N 1s peaks at 398.8eV. This is similar to previous reports of surface transfer doping of graphene by the same molecules where the charge neutral peaks appear only after sufficient amounts of F_4-TCNQ has been deposited and the charge transfer between the molecular layer and graphene has saturated.[10] We note that both N 1s and its associated shake up peaks experience no shifts in binding energy with increasing amounts of 6T deposited. This indicates that there is no observable chemical interaction between the two molecular species.

In Figure 5.5b, the S 2p peak of 6T molecules is located at a binding energy of 163.8 ± 0.1eV (with reference to the larger S $2p_{3/2}$ peak).[13] It is made up of a doublet with 2:1 intensity ratio due to the spin-orbit coupling of the $2p_{3/2}$ and $2p_{1/2}$ orbitals. Figure 5.5d plots the evolution of the S 2p and N 1s associated photoelectron intensities with increasing amounts of 6T molecules deposited. As more 6T molecules are being deposited, we note that the corresponding S 2p peaks increases while the F_4-TCNQ related N 1s peak intensity remains the same. This implies that the 6T molecules are not deposited directly on the F_4-TCNQ molecules, which would have resulted in an attenuation of the related N 1s peaks. This matches our observation of their growth behaviour under LT-STM, in which the deposited 6T molecules form an in-plane bimolecular network with F_4-TCNQ. In addition, we note that the S 2p signal stops increasing in intensity after 8.5 minutes of deposition. This would be elaborated on later after we compare the relative ratio of the amount of molecules deposited.

The ratio between the two molecular species is determined by comparing the peak area of the unique N 1s peak signals belonging to F_4-TCNQ molecules to that of the S 2p signals which originate from the 6T molecules. By taking into account the atomic sensitivity factors for both elements at a photon energy of 500eV (0.43 for N 1s and 0.54 for S 2p)[19,20] and also the number of atoms on each molecule (4 N atoms on F_4-TCNQ and 6 S atoms on 6T), we can monitor the ratio between the coverage of the two molecules during deposition. The ratio of the number of 6T : F_4-TCNQ molecules at each stage of 6T deposition is plotted in Figure 5.5d. The ratio between the two increases gradually from 0.34 with an initial 1 min deposition of 6T and eventually plateaus at 1.8 ± 0.4 after a total of 8.5 mins and 12 mins of 6T is deposited. This corresponds to the saturation of the S 2p signal in Figure 5.5b and hence number of 6T molecules after 8.5 mins of 6T deposition. The saturation in the number of 6T molecules could be due to the reduction in sticking coefficient of the incoming 6T molecules after a well-packed bimolecular network is formed. The plateau in the ratio with increasing deposition time indicates that the formation of the bimolecular network is a self-limiting one, where after a 1.8:1 6T : F_4-TCNQ coverage is obtained, further insertion of 6T molecules is prohibited.

Even though the desired 2:1 coverage is not obtained, based on the prior STM observations, we assume that the majority of the molecular layer consists of the 2:1 packing ratio. The discrepancy between the ratios observed under STM and PES measurements could be due to additional adsorption of residual F_4-TCNQ molecules in the same chamber where 6T deposition was carried out, as evidenced by the jump in N 1s signal in Figure 5.5d. This may have resulted in more than 1/3 coverage of the F_4-TCNQ

molecules deposited, preventing a 2:1 bimolecular network forming on the entire graphene surface. In addition, some parts of the surface could consist of the SiC buffer layer. As evidenced for $C_{60}F_{48}$ molecules in Chapter 3, molecules tend to be unable to form close packed molecular layers due to the high diffusion barrier on the buffer layer surface. This could prevent the formation of a well ordered bimolecular network and hence the achievement of a 2:1 ratio.

The core level C 1s peak is also measured and shown in Figure 5.5c. Before deposition, the sample exhibits the characteristic signals from the bulk SiC (283.8 ± 0.1eV), graphene (284.9 ± 0.1eV) and buffer layer (285.6 ± 0.1eV). After deposition of the F_4-TCNQ molecules, the C 1s peak of the epitaxial graphene shifted from its original binding energy of 284.9 to 284.7 ± 0.1eV and also experiences attenuation due to molecules deposited on the surface. The shift in the binding energy is due to charge transfer from graphene to the molecules, resulting in a band bending and lowering of the Fermi level of graphene closer to the C 1s core levels. This charge transfer is also evidenced by the presence of negatively charged nitrogen atoms observed in Figure 5.5a.

Both buffer layer and bulk associated peaks experience no shifts in binding energy, indicating that only the surface graphene layer is affected by the charge transfer. The C 1s peak due to the F_4-TCNQ at 286.1 and 287.3eV[10] is not detected as the amount deposited in this experiment is very small (0.1nm). After deposition of the 6T molecules, we note that there is a slight broadening of the C 1s peaks. In addition, there does not seem to be any significant attenuation of the graphene peaks. This is due to 6T molecules having C 1s peaks in the region of 285.1eV and 284.4eV,[13] which corresponds to the sulphur and non-sulphur bonded carbon atoms respectively. As these peaks are within the

binding energy range of the epitaxial graphene related peaks, it is difficult to accurately locate the C 1s graphene peak. In order to directly observe the doping effect of the molecules and their influence on the electronic band structure, ARPES measurements are carried out at 120K to probe the band structure perpendicular to the Γ-K direction of the graphene Brilluoin Zone.

Figure 5.6 describes the graphene electronic band structure about the K point a) before and after deposition of b) F_4-TCNQ and c) 6T molecules respectively. The binding energies and the intensities of all the spectrum has been calibrated and normalized against the Fermi edge of an Au sample present in the chamber. The linear bands of pristine monolayer graphene on SiC (0001) are presented in Figure 5.6a with the Dirac point located at 0.40 ± 0.05eV below the Fermi level, similar to other reports.[17,21] The intrinsic electron doping is due to the presence of the buffer layer as explained in Chapter 3. After deposition of 0.1nm F_4-TCNQ (Figure 5.6b), the linear bands experience a rigid shift, with the Dirac point now situated at 0.15 ± 0.05eV below the Fermi level. This is a shift of 0.25eV from pristine epitaxial graphene, consistent with similar report on F_4-TCNQ doping of graphene.[17] The shift of the Dirac point towards the Fermi level is due to charge transfer from the graphene to the F_4-TCNQ which reduces the intrinsic electron doping of pristine graphene introduced by the buffer layer. This is consistent with the shift in C 1s core level of graphene to a lower binding energy in Figure 5.5c. The linearity and sharpness of the bands are maintained, indicating that the integrity of the graphene layer is preserved after molecular deposition.

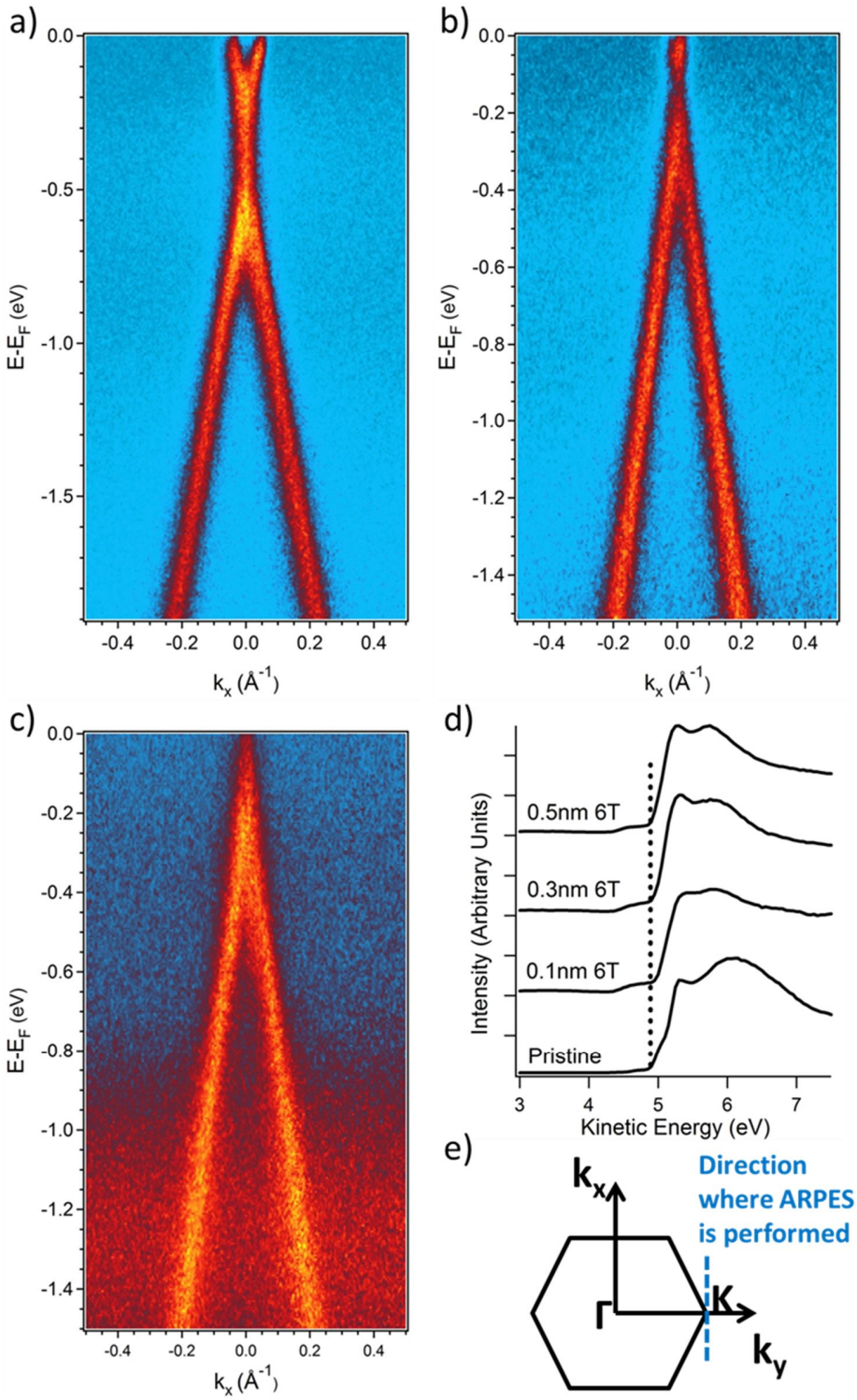

Figure 5.6 ARPES measurements of a) pristine epitaxial graphene, b) after deposition of 0.1nm F_4-TCNQ and c) Mixed molecular 6T to F_4-TCNQ ratio of 1.8:1.Photon energy of 60eV is used. d) UPS spectra at low photoelectron kinetic energy part with increasing amounts of 6T deposited on graphene. Dotted line marks the secondary electron cut-off. 21.2eV photon energy is used. e) Geometry of ARPES measurements.

In order to ascertain the effects of a bimolecular network, ARPES measurements are performed after a 1.8: 1 ratio of 6T to F_4-TCNQ molecular coverage is achieved and the spectrum is described in Figure 5.6c. We observe that there is a greater reduction in electron doping as the Dirac point is now at the Fermi level. As 6T is not a known dopant on HOPG[13], we hypothesize that the shift in Dirac point could be due to additional adsorption of residual F_4-TCNQ molecules in the same chamber where 6T deposition was carried out, thereby enhancing the doping effect. An increase in the amount of F_4-TCNQ molecules is evidenced in the increase of the N 1s signal intensity in Figure 5.5a after 1 min of 6T has been deposited. Likewise, the bands remain linear and sharp, implying that the physical structure of graphene remains intact. In addition, there is a decrease in the signal to noise ratio of the spectrum. The increase in the background intensity is attributed to the molecular over layer that attenuates the signal intensity from graphene. In addition, we note that there is an enhanced signal in the region located at binding energies greater than 0.9eV. This is due to photoelectrons from the 6T electronic orbitals present in the valence band region.[10,22] The possibility of the contribution attributed to F_4-TCNQ molecules is excluded as previous studies have shown no signs of it even after 0.4nm thickness was deposited.[17] Photoemission from these molecular orbitals hence obscures the analysis of the band dispersion in this energy region.

To confirm our earlier hypothesis, *in-situ* thickness dependent UPS was performed to monitor any changes in work function as 6T molecules are deposited on a separate piece of epitaxial graphene on SiC and is shown in Figure 5.6d. According to Equation 5.1, the work function is determined from the SECO at the low kinetic energy range of the photoelectrons. As indicated by the SECO (dotted line in Figure 5.6d), a

work function of 4.2eV is obtained for pristine graphene and it remains constant with increasing 6T deposition from nominal thicknesses of 0.1nm to 0.5nm. This indicates that the vacuum level between 6T and graphene is well aligned and there is no observable charge transfer between the two. Thus, only the F_4-TCNQ molecules of the bimolecular network contribute to the doping of graphene.

The slope of the linear band dispersion in Figures 5.6a – c is then measured to detect any signs of Fermi velocity renormalization induced by the presence of the molecules. The slope is obtained by first determining the peak locations, k_x, over a range of binding energies of the spectrum followed by performing a linear fit to the obtained peak locations. The peak locations are measured by doing a fit using two Lorentzian peaks, one for each linear band, to the momentum distribution curve (MDC) of the spectrum described in Figures 5.6a – c. Fitting was not done for the linear bands with binding energies greater than 0.85eV after deposition of 6T molecules as the background intensity is too high to make accurate fits. In addition, fitting was only performed for the MDC in the range of the binding energies where the two peaks are distinctly discernible to minimize errors and also sufficiently away from the kink present at the Dirac point. To ensure that the linear bands measured have the same baseline for comparison, i.e.: that comparable sections of the band dispersion is measured, the doping of the graphene layer is also taken into account.

The results of the analysis are shown in Figure 5.7. Figures 5.7a and b describe the fitted positions of the left and right linear bands respectively. The offset in their energy as well as their k vector values is due to the choice in range of binding energies over which fitting was performed. The binding energies selected are [-0.89eV, -1.21eV],

[-0.64eV, -0.96eV], [-0.49eV, -0.81eV] for pristine graphene, after 0.1nm of F_4-TCNQ and after a bimolecular mixture is deposited respectively. The lower limit is selected so that the fitting is done over bands which are well separated and defined while the upper limit is chosen to avoid the background intensity present in the ARPES data for the bimolecular mixture. After performing a linear fit for the band in Figure 5.7a, band velocities of 1.01 ± 0.04 x 10^6 ms^{-1} and 0.99 ± 0.04 x 10^6 ms^{-1} are obtained for pristine graphene and after deposition of 0.1nm of F_4-TCNQ respectively.

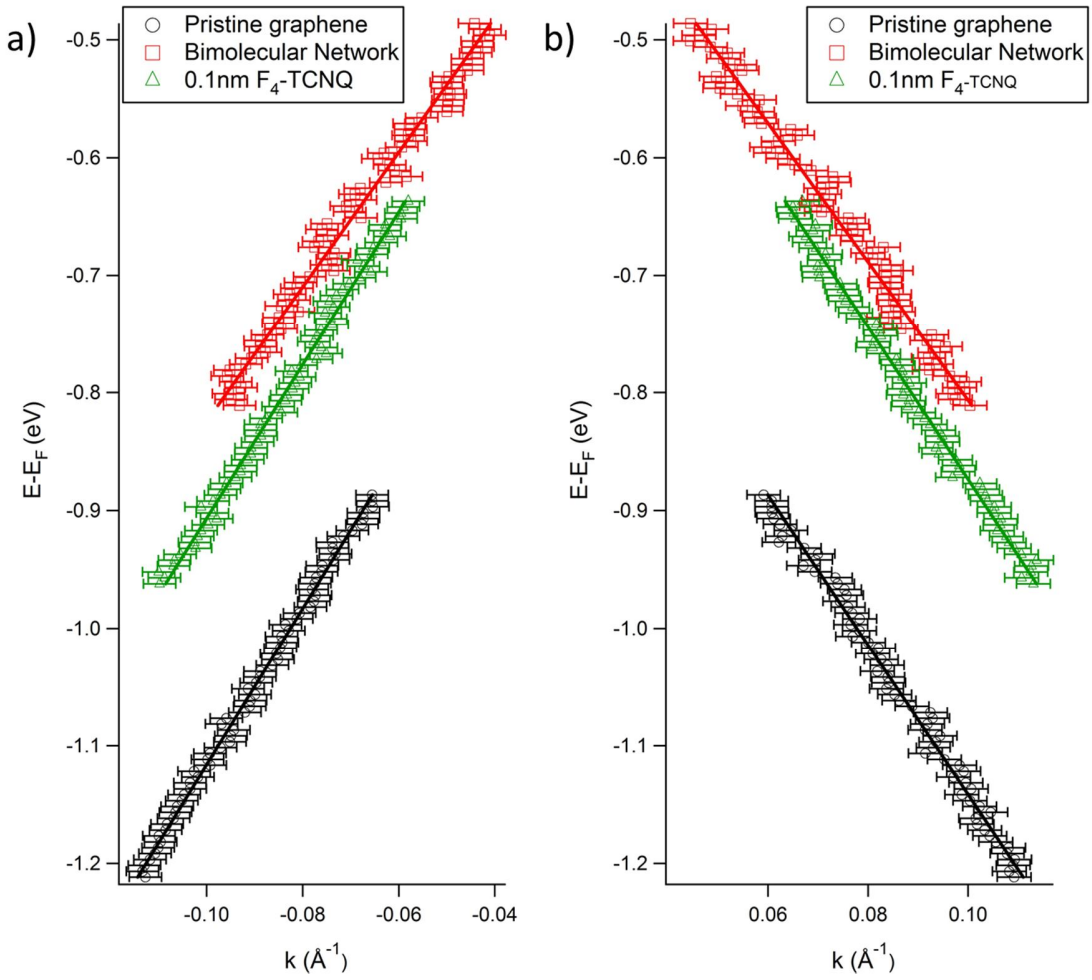

Figure 5.7 The fitted band positions of a) first and b) second linear band dispersion of graphene. Band dispersions of pristine graphene (black circles), after 0.1nm F_4-TCNQ deposition (green triangles) and after 1.8:1 6T to F_4-TCNQ coverage has been deposited are indicated.

We observe that there are no significant changes in the Fermi velocity after p-type doping of the F_4-TCNQ molecules. The Fermi velocity obtained is consistent with previous reports of around 1 x 10^6 ms^{-1} for epitaxial graphene on SiC.[23] After additional deposition of 6T to the 0.1nm F_4-TCNQ layer, the Fermi velocity decreases to a value of 0.87 ± 0.04 x 10^6 ms^{-1}. This constitutes to a 0.14 x 10^6 ms^{-1} or a 14 ± 8% reduction in the Fermi velocity after deposition of both F_4-TCNQ and 6T molecules. Likewise for Figure 5.6b, the Fermi velocity of the linear band after just 0.1nm deposition F_4-TCNQ remains similar to pristine epitaxial graphene but it experiences a reduction of 0.08 x 10^6 ms^{-1} or 8 ± 9% after deposition of both molecular species. The discrepancy between the two values obtained could be due to a finite misalignment of the detector slit along the desired direction of data acquisition. This would result in a slight asymmetry between the band dispersions which is reflected in our fit.

As there is no observable difference in the linear bands after deposition of 0.1nm F_4-TCNQ, the influence due to a purely F_4-TCNQ molecular layer can be excluded. This implies that the presence of a bimolecular network consisting of periodically placed dopant molecules (F_4-TCNQ) is capable of influencing the electronic band structure of graphene by renormalizing the Fermi velocity of graphene. We note that the change in Fermi velocity obtained here is much lower than that reported by Rusponi et. al. of 70% when Ir cluster superlattices are bonded to graphene.[24] This may be due to the lower potential difference generated between each region of the bimolecular network. This can be approximated to a maximum of 0.4eV by assuming that the doping observed in the ARPES results is well localized around the F_4-TCNQ molecules. In addition, a lack of well-defined symmetry of the bimolecular network with respect to the underlying

graphene layer may also contribute to the lower extent of renormalization of the band dispersion. However, due to technical constraints as well as limitations in system resolutions, a complete Fermi surface mapping after deposition of both molecular species cannot be performed. We are also unable to obtain the band dispersion along the Γ – K direction to compare the predicted anisotropy in the Dirac cone dispersion under a periodic potential.

5.5 Conclusion and Future Work

In summary, a bimolecular network with a possibility of generating a periodic potential has been generated on epitaxial graphene via molecular deposition using 6T and F4-TCNQ molecules. After an initial deposition of both molecules, a mixture of bimolecular networks is generated, with the 1:1 and 1:2 F4-TCNQ to 6T coverage ratio being the dominant ones due to an uneven deposition of molecules across the entire sample surface. The spread of the doping effect generated by these molecules is approximated from STS taken over exposed graphene regions to be less than 4nm. When 6T molecules are deposited in excess, instead of having a coexistence of different networks with varying molecular ratio, a bimolecular layer with the unit cell having a 1:2 ratio between the F4-TCNQ and 6T molecular coverage respectively can be formed over majority of the surface.

The bimolecular network was then deposited in a different chamber according to the growth procedures presented in the LT-STM observations and PES measurements were taken to monitor its development. The formation of the bimolecular layer is found to be a self-limiting one with a saturation of the 6T : F_4-TCNQ coverage ratio at 1.8 : 1. Perfect 2 : 1 ratio could not be obtained due to inclusion of additional F_4-TCNQ

molecules during deposition of 6T molecules in the same chamber as well as the possibility of the presence of a buffer layer that inhibits its development. ARPES measurements of the as-deposited bimolecular layer indicate that there is a renormalization in the Fermi velocity of up to 14 ± 8%, demonstrating the possibility of a bimolecular network altering the electronic band structure of graphene. This indicates a promising approach of applying a periodic potential to graphene on the length scale of molecular dimensions without resorting to covalent bonding or external application of electric fields.

However, to truly determine whether anisotropic renormalization has taken place, complete mapping of the Dirac cone dispersion is required. Also, to minimize the background signal from the molecular orbitals, perhaps a proper choice of molecules with molecular orbitals located at least 1.5 eV or more from the Fermi level to minimize the background intensity around the regions where the linear band dispersion of graphene exists. The lattice parameters of the bimolecular arrangement on graphene can also be altered with a different choice of molecules and the resultant graphene electronic band dispersion can be compared with our current results. ARPES measurements on graphene that has only 6T deposited on it should also be carried out to exclude their involvement in the renormalization of the Fermi velocity and to confirm that indeed, it is a periodic array of two molecules and not the 6T molecules that caused the observed changes. Lastly, additional theoretical computations can be carried out to determine the lattice parameters and strength of the periodic potential generated by the bimolecular network.

References

1. C.H. Park; L. Yang; Y.W. Son; M. Cohen and S. Louie, *Nature Phys.* **4**, 213-217 (2008).

2. L. Brey and H.A. Fertig, *Phys. Rev. Lett.* **103**, 046809 (2009).

3. C.H. Park; Y.W. Son; L. Yang; M.L. Cohen and S.G. Louie, *Phys. Rev. Lett.* **103**, 046808 (2009).

4. C.H. Park; L. Yang; Y.W. Son; M.L. Cohen and S.G. Louie, *Phys. Rev. Lett.* **101**, 126804 (2008).

5. S. Rusponi; M. Papagno; P. Moras; S. Vlaic; M. Etzkorn; P. Sheverdyaeva; D. Pacilé; H. Brune and C. Carbone, *Phys. Rev. Lett.* **105**, 246803 (2010).

6. Y.L. Huang; W. Chen; H. Li; J. Ma; J. Pflaum and A. Wee, *Small* **6**, 70-75 (2010).

7. Y.L. Huang; W. Chen and A.T.S. Wee, *J. Am. Chem. Soc.* **133**, 820-825 (2011).

8. Y.L. Huang and A.T.S. Wee, *Langmuir* **26**, 3329-3334 (2009).

9. Y.L. Huang; W. Chen; H. Li; J. Ma; J. Pflaum and A.T.S. Wee, *Small* **6**, 70-75 (2010).

10. W. Chen; S. Chen; D.C. Qi; X.Y. Gao and A.T.S. Wee, *J. Am. Chem. Soc.* **129**, 10418-10422 (2007).

11. F. Jäckel; U. Perera; V. Iancu; K.F. Braun; N. Koch; J. Rabe and S.W. Hla, *Phys. Rev. Lett.* **100**, 126102 (2008).

12. K.F. Braun and S.W. Hla, *J. Chem. Phys.* **129**, 064707 (2008).

13. R. Wang; H.Y. Mao; H. Huang; D.C. Qi and W. Chen, *J. Appl. Phys.* **109**, 084307 (2011).

14. P. Lauffer; K.V. Emtsev; R. Graupner; T. Seyller and L. Ley, *Phys. Rev. B* **77**, 155426 (2008).

15. T. Ohta; A. Bostwick; T. Seyller; K. Horn and E. Rotenberg, *Science* **313**, 951-954 (2006).

16. J.T. Sun; Y.H. Lu; W. Chen; Y.P. Feng and A.T.S. Wee, *Phys. Rev. B* **81**, 155403 (2010).

17. C. Coletti; C. Riedl; D.S. Lee; B. Krauss; L. Patthey; K. von Klitzing; J.H. Smet and U. Starke, *Phys. Rev. B* **81**, 235401 (2010).

18. J.M. Lindquist, *J. Phys. Chem.* **92**, 1394-1396 (1988).

19. J. Yeh and I. Lindau, *At. Data. Nuc. Data Tables* **32**, 1-155 (1985).

20. J.J. Yeh, *Atomic Calculation of Photoionization Cross-Sections and Asymmetry Parameters* (Gordon & Breach Science, 1993).

21. S.Y. Zhou; G.H. Gweon; A.V. Fedorov; P.N. First; W.A. de Heer; D.H. Lee; F. Guinea; A.H. Castro Neto and A. Lanzara, *Nature Mater.* **6**, 770 (2007).

22. S. Duhm; G. Heimel; I. Salzmann; H. Glowatzki; R.L. Johnson; A. Vollmer; J.P. Rabe and N. Koch, *Nature Mater.* **7**, 326-332 (2008).

23. S.Y. Zhou; D.A. Siegel; A.V. Fedorov and A. Lanzara, *Phys. Rev. Lett.* **101**, 086402 (2008).

24. S. Rusponi; M. Papagno; P. Moras; S. Vlaic; M. Etzkorn; P. Sheverdyaeva; D. Pacil; H. Brune and C. Carbone, *Phys. Rev. Lett.* **105**, 246803 (2010).

Chapter 6: Conclusion and Outlook

6.1 Thesis Summary

In this thesis, we aim to modify the physical and electronic structure of graphene through the application of organic molecules. We have presented the modification of epitaxial graphene on SiC (0001) in three different organic molecule – graphene systems and studied the modified properties using a combination of STM and PES measurements.

In Chapter 3, successful fluorine intercalation was demonstrated through stepwise thermal annealing of $C_{60}F_{48}$ molecules deposited on the graphene surface. Fluorine dissociates from the molecules during annealing and two temperature dependent phases of intercalation was observed, namely the semi-intercalated and quasi-freestanding graphene. At moderate temperatures of 150°C, fluorine is observed to intercalate selectively at regions where Si dangling bonds are present in the interface between the buffer layer and the SiC bulk substrate. The interfacial Si-F species in turn reduces the substrate interaction with the carbon layer. Thus, the as produced semi-intercalated graphene exhibits properties of a graphene array periodically bonded at the zigzag edges, with a band gap of 280meV due to quantum confinement of the electrons. The method described herein presents an alternative strategy for the production of graphene arrays using a bottom-up approach, circumventing the need for conventional lithography or covalent bonding with surface adatoms.

At higher temperatures of 900°C, the fluorine intercalation was complete and quasi-freestanding graphene is obtained. The bonds between the buffer layer and the bulk substrate were broken and the buffer layer is hence converted into quasi-freestanding

graphene with a passivated Si-F interface beneath it. Due to the absence of the buffer layer, the doping of the quasi-freestanding graphene is greatly reduced and is found to be charge neutral by STS. Localised perturbations by adsorbed fluorine is also measured and attributed to fluorine adatoms present between the newly formed quasi-freestanding graphene and the substrate. PES measurements confirm both the presence of the Si-F interfacial layer as well as the reduced doping in the quasi-freestanding graphene. These intercalation studies conducted would enable us to better understand such processes involved and thus improve our control over them.

Its less fluorinated $C_{60}F_{36}$ counterpart was also used as a fluorine source for selective fluorination of graphene in Chapter 4. $C_{60}F_{36}$ was first deposited and synchrotron beam irradiation was then used to write the desired regions to be fluorinated on graphene. PES studies reveal the much enhanced fluorination of the irradiated area compared to its surrounding regions, about twelve folds larger amount of C-F covalent bond formation, indicating the selectivity of the technique. Fluorine dissociates from the molecules during irradiation and C-F covalent bonds were formed during the process. In addition, NEXAFS measurements indicate the presence of in-plane dangling bonds were produced as a result of the C=C bond being disrupted during fluorination. The successful demonstration of selective fluorination using synchrotron beam provides a means for a more controlled and directed functionalization of graphene instead of the usual method of non-selective fluorination by gases and plasma.

In Chapter 5, we aim to generate a periodic potential on graphene using selective hydrogen bonding between 6T and F_4-TCNQ molecules to anisotropically renormalize the Fermi velocity of graphene. With appropriate growth parameters, a periodic

bimolecular network was shown to form between the two molecular species on graphene with a ratio of 2:1 between the 6T : F_4-TCNQ molecules. STS results on exposed graphene surfaces present in defects of the molecular layer reveal the possibility that the doping effect introduced by individual F_4-TCNQ molecules have a limited range of at most 4nm. This network was then repeated in a separate PES analysis chamber and monitored using PES. The formation of the bimolecular network was found to be self-limiting with a maximum attainable ratio of 1.8:1 between the 6T : F_4-TCNQ molecules. ARPES measurements indicate that doping by F_4-TCNQ molecules alone only results in a rigid shift of the linear bands towards the Fermi level while a combination of the two molecular species causes a reduction in the band velocity of up to 14%. Our results imply the possibility of a Fermi velocity renormalisation through the periodic potential generated by a bimolecular network. The work described herein is a first step towards creating a periodic potential array based on self-assembled molecular networks and further our understanding on their potential effects on the electronic band structure of graphene.

6.2 Future Work

In this dissertation, we have looked into the various modifications of graphene by organic molecules on the atomic scale as well as its effects on the electronic and chemical structure of graphene. However, complete controllability of these processes and full understanding of their effects has not been achieved yet. To fully elucidate the impact of our modifications on the electronic and magnetic properties of graphene, there are further works still to be carried out.

Presently, the dimensions of the semi-intercalated graphene as well as the quasi-freestanding graphene are limited by the terrace sizes of the buffer layer on which they are developed on. Larger coverage of the buffer layer would require refinement of the graphene growth process and adopting methods such as Ar environment based thermal annealing. Once surface uniformity can be achieved, we can then investigate transport measurements through a graphene array produced after semi-intercalation as well as the effects of an interfacial Si-F layer on the transport properties of quasi-freestanding graphene.

Instead of using fluorinated species, alternative forms of functionalization can be explored by using species with different functional groups such as Cl or Br. Furthermore, to improve the ease of implementation, ambient methods of molecular excitation such as lasers can also be carried out. Possibility of fluorine adatom induced magnetism should also be explored through complementary experiments. In addition, there is a need to ascertain the resultant electronic structure and transport properties of these fluorinated graphene layers through other techniques such as Hall measurements or ARPES.

As mentioned in Chapter 5, additional ARPES measurements to map the Fermi surface of graphene would enhance our understanding of the Fermi velocity renormalisation. A drawback to the presented method is the susceptibility of these bimolecular layers to external environments. Future work should look into strengthening the intermolecular interactions to maintain their structural integrity. Covalent organic frameworks which involve covalent bonding between molecules may provide a stronger alternative to intermolecular hydrogen bonding to stabilise these molecules or a protective capping layer can be employed to prevent external perturbation.